Spectroscopic Investigation of the Transient Interplay at Hybrid Molecule-Substrate Interfaces after Photoexcitation: Ultrafast Electronic and Atomic Rearrangements

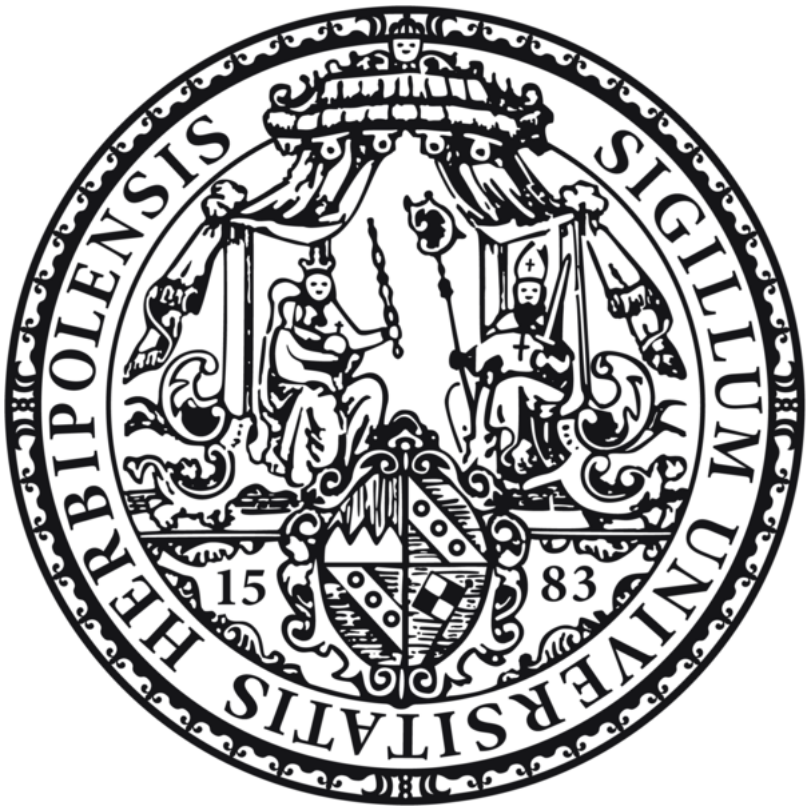

Dissertation zur Erlangung des
naturwissenschaftlichen Doktorgrades
der Julius-Maximilians-Universität Würzburg

vorgelegt von

Kiana Jasmin Baumgärtner
aus Stuttgart

Würzburg 2023

This document is licensed under the Creative Commons Attribution 4.0 International License (CC BY 4.0):
http://creativecommons.org/licenses/by/4.0 This CC license does not apply to third party material (attributed to another source) in this publication.

Eingereicht am: 6. April 2023
bei der Fakultät für Physik und Astronomie

1. Gutachter: Prof. Dr. Friedrich Reinert
2. Gutachter: Prof. Dr. Jens Pflaum
3. Gutachter: Prof. Dr. Giorgio Sangiovanni
der Dissertation

Vorsitzende(r): Prof. Dr. Karl Mannheim

1. Prüfer: Prof. Dr. Friedrich Reinert
2. Prüfer: Prof. Dr. Jens Pflaum
3. Prüfer: Prof. Dr. Giorgio Sangiovanni
im Promotionskolloquium

Tag des Promotionskolloquiums: 22. September 2023

Doktorurkunde ausgehändigt am: _____

Zusammenfassung

Das Ziel der vorliegenden Doktorarbeit ist es, die Bewegung von Atomen, Ladungsträgern und Energie an organisch/anorganischen Grenzschichten fernab des thermischen Gleichgewichts zu visualisieren und deren Wechselwirkung zu entschlüsseln. Dies wird experimentell mittels zeitaufgelöster Photoemissionsexperimente an einer Freien-Elektronen-Laser-Quelle und an einer Höher-Harmonischen-Quelle verwirklicht.

Ladungs- und Energietransfer zwischen organisch/anorganischen Grenzschichten sind zentrale Komponenten für die Funktion Molekül-basierter Anwendungen, wie z.B. katalytische Oberflächen, elektronische Schalt- und Speichergeräte oder molekulare Maschinen [1–3]. Sie stellen einen dynamischen Prozess dar, der sich in einem Wechselspiel aus der Bewegung von Elektronen zwischen beiden Schichten und atomaren Bewegungen innerhalb beider Schichten äußert. Planare Moleküle, wie Pentacen oder Kupfer(II)-Phthalocyanin (CuPc), eignen sich besonders um solche atomaren Bewegungen zu untersuchen, da diese aufgrund geringer Rückstellkräfte senkrecht zur Molekülebene besonders ausgeprägt sein können.

In dieser Arbeit werden Ladungs- und Energietransferprozesse an zwei ausgewählten Grenzschichten untersucht: Pentacen auf Silber (Ag(110)) und CuPc auf Titan Diselenid ($1T$-$TiSe_2$). Zeitaufgelöste Photoemissionsexperimente (tr-PES) wurden an einer Höher-Harmonischen-Quelle [4] und an dem Freien-Elektronen-Laser *FLASH* (Deutsches Elektronen-Synchrotron DESY, Hamburg, Deutschland) [5] durchgeführt. Beide Lichtquellen liefern Photonenpulse mit einer Halbwertsbreite von etwa 100 fs und sind daher geeignet, um Nicht-Gleichgewichtsprozesse zeitlich aufzulösen, die auf der Bewegung von sowohl Elektronen als auch Atomen basieren. Die gewählte Höher-Harmonische-Quelle liefert Photonenenergien im UV-Bereich. Bei *FLASH* hingegen können die Photonenenergien variabel vom UV-Bereich bis hin zum Weichröntgenbereich erzeugt werden [5]. Dieser erweiterte Energiebereich ermöglicht es, zusätzlich zur elektronischen Dynamik im Valenzbereich, auch Dynamiken kernnaher Zustände zu beobachten. Mithilfe dreier Modalitäten von zeitaufgelöster Photoemission – zeit- und winkelaufgelöste Photoelektronenspektroskopie (tr-ARPES), zeitaufgelöste Röntgenphotoelektronenspektroskopie (tr-XPS) und zeitaufgelöste Röntgenphotoelektronen-Diffraktion (tr-XPD) – werden sowohl die elektronischen als auch strukturellen Dynamiken der Grenzschicht rekonstruiert. Dabei dient tr-ARPES im UV-Bereich zur Charakterisierung der makroskopischen elektronischen Eigenschaften und tr-XPS und tr-XPD im Weichröntgenbereich dienen zur Analyse lokaler chemischer und struktureller Eigenschaften. Alle Messungen wurden unter denselben experimentellen Be-

dingungen durchgeführt und mithilfe eines Flugzeit-Impulsmikroskops [6] konnte die transiente Bandstruktur mit einer Ortauflösung im Sub-Ångström-Bereich und einer Zeitauflösung im Femtosekunden-Bereich aufgenommen werden.

In beiden untersuchten Systemen werden elektronische und strukturelle Prozesse an der Molekül–Substrat Grenzfläche beobachtet, die durch einen Ladungs- und Energietransfer in Folge optischer Anregung erklärt werden. Dieser Transfer äußert sich elektronisch durch ein Befüllen des Substrat-Leitungsbands und einem zeitgleichen Entleeren der Molekül-Valenzorbitale. Strukturelle Veränderungen, wie die Adsorptionshöhe oder intramolekulare Atompositionen, werden aus den sich zeitgleich verformenden Molekül-Valenzorbitalen rekonstruiert. Speziell für CuPc/$TiSe_2$ wird ein effektiver Ladungstransfer beobachtet, wodurch 375 fs nach optischer Anregung $\sim 45\,\%$ der Moleküle einfach positiv geladen vorliegen. Diese Ladungstrennung zwischen den sich wie ein Schachbrett anordnenden positivgeladenen und neutralen Molekülen sowie dem Substrat führt zu einer Modulation des Oberflächenpotentials, welche eine energetische Verschiebung aller Grenzflächenzustände bedingt und intramolekulare Strukturveränderungen sowie eine makroskopische Reorganisation des Molekülfilms zur Folge hat: $\sim 60\,\%$ der Moleküle drehen sich innerhalb von ~ 375 fs synchron auf dem Substrat und nehmen nach ~ 1800 fs wieder ihre Ausgangsposition ein. Diese überraschende Beobachtung sowie die Ursache werden detaillierter in der vorliegenden Arbeit diskutiert und in den Kontext aktueller Forschung an "molekularen Schaltern" gebracht.

Abstract

This thesis is aimed at establishing modalities of time-resolved photoelectron spectroscopy (tr-PES) conducted at a free-electron laser (FEL) source and at a high harmonic generation (HHG) source for imaging the motion of atoms, charge and energy at photoexcited hybrid organic/inorganic interfaces.

Transfer of charge and energy across interfaces lies at the heart of surface science and device physics and involves a complex interplay between the motion of electrons and atoms. At hybrid organic/inorganic interfaces involving planar molecules, such as pentacene and copper(II)-phthalocyanine (CuPc), atomic motions in out-of-plane direction are particularly apparent. Such hybrid interfaces are of importance to, e.g., next-generation functional devices, smart catalytic surfaces and molecular machines [1–3].

In this work, two hybrid interfaces – pentacene atop Ag(110) and copper(II)-phthalocyanine (CuPc) atop titanium disulfide ($1T$-$TiSe_2$) – are characterized by means of modalities of tr-PES. The experiments were conducted at a HHG source [4] and at the FEL source *FLASH* at Deutsches Elektronen-Synchrotron DESY (Hamburg, Germany). Both sources provide photon pulses with temporal widths of $\sim 100\,\mathrm{fs}$ and thus allow for resolving the non-equilibrium dynamics at hybrid interfaces involving both electronic and atomic motion on their intrinsic time scales. While the photon energy at this HHG source is limited to the UV-range, photon energies can be tuned from the UV-range to the soft x-ray-range at *FLASH* [5]. With this increased energy range, not only macroscopic electronic information can be accessed from the sample's valence and conduction states, but also site-specific structural and chemical information encoded in the core-level signatures becomes accessible. Here, the combined information from the valence band and core-level dynamics is obtained by performing time- and angle-resolved photoelectron spectroscopy (tr-ARPES) in the UV-range and subsequently performing time-resolved x-ray photoelectron spectroscopy (tr-XPS) and time-resolved photoelectron diffraction (tr-XPD) in the soft x-ray regime in the same experimental setup. The sample's bandstructure in energy-momentum space and time is captured by a time-of-flight momentum microscope [6] with femtosecond temporal and sub-Ångström spatial resolutions.

In the investigated systems, out-of-equilibrium dynamics are traced that are connected to the transfer of charge and energy across the hybrid interfaces. While energetic shifts and complementary population dynamics are observed for molecular and substrate states, the shapes of involved molecular orbitals change in energy-momentum space on a sub-picosecond time scale. In combination with theory support, these changes are attributed to

atomic reorganizations at the interface and transient molecular structures are reconstructed with sub-Ångström precision. Unique to the material combination of CuPc/$TiSe_2$, a structural rearrangement on the macroscopic scale is traced simultaneously: $\sim 60\,\%$ of the molecules undergo a concerted, unidirectional in-plane rotation. This surprising observation and its origin are detailed in this thesis and connected to a particularly efficient charge transfer across the CuPc/$TiSe_2$ interface, resulting in a charging of $\sim 45\,\%$ of CuPc molecules.

Table of contents

1 Introduction

In the year 2000, Herbert Kroemer famously stated in his Nobel Prize lecture that *the interface is the device* [7]. With interfaces being at the origin of effects such as transfer and separation of charge and energy, this statement framed his successful work in the field of semiconductor interfaces for implementation in electronic and optical devices. Driven by the goal to miniaturize and further customize their design, research has since then expanded towards implementing organic materials in such devices. These carbon-based molecular materials are not only available in abundance and vastly functionizable but also promise to have a reduced impact on our environment during their recycling [8]. In the past three decades, an understanding of electronic and structural properties at hybrid organic/inorganic interfaces has been developed [8–13]. Based on this, significant progress has been made towards exploring molecular designs for creating hybrid devices with tailor made functionality: organic light emitting diodes (OLED) [14] and organic field effect transistors (OFET) [15] have been developed as counterparts to their inorganic equivalents. Adsorbed molecules have been incorporated to the design of information storage devices in the form of molecular switches – molecules undergoing switching motions in response to an external stimulus [16]. And molecular machines have been built capable of transferring energy and mechanical work across interfaces [1, 17].

Today, we are challenged by understanding the dynamic aspect of device function. Being at the origin of device function, this challenge starts with unraveling the dynamic properties of hybrid organic/inorganic interfaces. Device function is driven by the flow of charge and energy across the interface, intertwining both electronic and atomic motion. The effects are particularly strong for 'soft' molecules in contact with interactive surfaces as, e.g. in catalysis and molecular electronics. Upon receiving a charge from the substrate, the geometric and electronic structure of an adsorbed molecule can change considerably, while its localized charge will in turn initiate the movement of mobile charge carriers in the substrate. This process will modify the substrate's local atomic and global electronic structure by shifting, distorting, or splitting of bands [9, 18, 19].

It is a long-standing goal of interface science to visualize and disentangle such intertwined dynamics by shooting 'molecular movies' [20–22], i.e., to image atomic positions and molecular orbitals in real or reciprocal space simultaneously with the population and modification of electronic states in energy-momentum space, as bonds and bands are rearranging in time. The typical approach to such movies is to initiate a dynamic process

with a femtosecond laser pump pulse and to film the subsequent temporal evolution by taking 'snapshots' of the system's bandstructure with femtosecond probe pulses at specified pump-probe time delays.

With the advent of light sources providing radiation with femtosecond pulse widths such as FELs and laboratory-based HHG sources, several electron-based measurement techniques have become available: ultrafast low-energy electron diffraction (ULEED) [23] and ultrafast reflection high-energy diffraction (URHEED) [24, 25] for measuring the global atomic structure of the interface, tr-XPD [26] for accessing site-specific structural information, tr-ARPES for imaging the electronic band structure [21, 27–29] and molecular orbital dynamics [22, 30], and tr-XPS for probing local, atomic site-specific chemical dynamics [31, 32].

In recent years, advances have been made towards shooting molecular movies and studies have been presented on the individual imaging of structural dynamics [20], valence band dynamics [21] and the transient occupation of a molecular orbital [22]. For a combined electronic and structural understanding of macroscopic as well as molecular-scale processes at the excited interface although, multimodal measurements are required that access both the valence band as well as core level dynamics of the same system. While transient valence band studies can be performed at laboratory-based HHG sources [4], the photon energies necessary for transient core level studies are currently only provided by FEL sources such as *FLASH*. In contrast to HHG sources, *FLASH* offers photon pulses with high brillance and with tunable energies from the UV-range to the soft x-ray-range [33]. This allows for conducting tr-ARPES, tr-XPS and tr-XPD experiments in a single setup with a femtosecond temporal resolution. However, tr-PES at FELs is still in its infancy unlike HHG-based science. Thus, conducting experiments as well as handling data in the post-processing stage remains challenging. At the beginning of the work on this thesis, it was even unknown whether organic samples would withstand the conditions of FEL irradiation or if they would degrade too quickly.

The goal of this thesis is to visualize and understand the dynamic response of a hybrid organic/inorganic interface to optical excitation. For obtaining a combined understanding of the induced electronic and structural dynamics, the modalities tr-ARPES, tr-XPS and tr-XPD were applied in a single setup at *FLASH*. With a time-of-flight momentum microscope [6] four-dimensional data sets of energy-momentum space and time were captured allowing for disentangling and separately tracing the temporal evolution of excited substrate and adsorbate states. Two separate studies are presented in this thesis. In an initial study, the experimental conditions for pump-probe measurements on hybrid organic/inorganic samples at *FLASH* are established on the example of the pentacene/Ag(110) interface. Thereby, first dynamic observations of molecular orbitals far from equilibrium are presented on a

sub-picosecond time-scale. Excitation and relaxation pathways across the interface are retraced and interfacial electronic and structural properties are reconstructed. Based on the experiences and conclusions made in the initial experiment, a second study has been conducted on the hybrid CuPc/$TiSe_2$ interface. For this second interface, an 'interfacial movie' is presented combining information on the sample's valence band and core level dynamics. Thereby, the motion of atomic positions is visualized together with the population and modification of electronic states. This work will contribute to the fundamental understanding of light-induced processes at hybrid interfaces towards tailoring the design of future molecule-based devices.

Hybrid Organic/Inorganic Interfaces – Fundamentals

2

This chapter is intended as an overview on established concepts describing hybrid organic/inorganic interfaces. The electronic and structural parameters of hybrid interfaces in a static picture are introduced in sections 2.1 and 2.2, respectively. Dynamic aspects to these electronic and structural parameters are discussed in section 2.3.

Hybrid interfaces play a crucial role in defining device function as they are the basis for both transfer and separation of charge and energy. It is fundamental to understand the electronic and structural properties at the interface in both their static and dynamic state upon external stimulation. The electronic properties are defined not only by the chemical nature of the hybrid components, but they are also largely influenced by the relative geometric arrangement between adsorbate and substrate [11, 34] and the electronic-atomic coupling [10, 35].

A hybrid interface is formed when organic molecules are deposited on an inorganic substrate. Upon adsorption both components are subject to interactive forces and their bond can be categorized as either physisorptive or chemisorptive, based on their interactive strength.

Physisorptive systems are based on non-covalent, weak interactions between adsorbate and substrate. Such interactions include electrostatic Coulomb forces as well as van-der-Waals forces that describe various combinations of permanent and induced dipole interactions. Due to the weak nature of these forces, the atomic structures at the interface and relative energy distances between molecular orbitals and their shapes are mainly retained by physisorption. Chemisorptive systems involve the formation of a covalent bond between adsorbate and substrate. Thus, both atomic structure and charge distribution at the interface are distinctly altered. A clear separation between these categories is not always applicable due to the continuous range of interactive strength [13]. Therefore, a third category of intermediate interactive strength is introduced here to describe interfaces with charge transfer between molecule and substrate. The following sections will discuss some of the energetic and structural aspects at such hybrid interfaces.

2.1 Energy Level Alignment

Before brought into contact, the electronic properties of a molecule and of an inorganic substrate are described by their intrinsic energy levels, the relative energetic positions of filled and empty states with respect to the Fermi level (E_F), and their workfunction ϕ, defined as the energetic difference between the vacuum level at the surface (E_{vac}) and E_F.

In crystalline substrates, energy levels at and around E_F form dispersive bands with filled (valence band) and empty (conduction band) states. Whereas in a single molecule, the electronic structure is characterized by discrete, non-dispersive molecular orbitals [36, 37]. Similar to crystalline substrates, the energetically stronger bound core level electrons are localized in orbitals at atomic sites, while the weaker bound electrons in the molecular frontier orbitals are delocalized over the entire molecule. In a molecular crystal, the molecular frontier orbitals of neighboring molecules, such as the highest occupied molecular orbital (HOMO) and the lowest unoccupied molecular orbital (LUMO), can form weakly dispersing bands (< 0.1 eV) [9]. Throughout this work although, only samples are studied in which molecules can be viewed as isolated from each other not forming bands.

Weak Molecule-Substrate Interactions

When molecule and inorganic substrate are brought into contact, their electrons experience the presence of the mutual charges. In physisorptive systems, the interplay between both electron clouds is weak and scales with the surface polarity of the materials [13, 38]. Two types of interactions arise: attractive van-der-Waals forces and repulsive electrostatic forces.

The repulsive electrostatic interaction between adsorbate and substrate electron clouds at the interface is termed push-back effect and is associated with a reduction of the system's work function by formation of an interface dipole [39, 40]. Reports on coverage dependent studies on metal substrates have revealed a linear change of the work function at the hybrid interface ϕ_{hybrid} upon physisorption of molecules until forming a closed monolayer [13, 41, 42]. For the growth of subsequent adsorbate layers, ϕ_{hybrid} continues to change linearly, but the linear slope is reduced step-wise with completion of each closed layer. ϕ_{hybrid} saturates when a critical adsorbate thickness is reached and the metal surface is no longer sensitive to the charge clouds of deposited adsorbate layers [10]. In contrast, for some systems involving substrates with large band gaps, such as SiO_2 and Al_xO_y, ϕ_{hybrid} has shown minimal dependence on adsorbate coverage [43]. There, the interaction between substrate and adsorbate is mainly limited to a weak attraction by induced or spontaneously created dipoles. Thus, molecule and substrate may be viewed as independent and the concept of vacuum level alignment can be applied to construct the interfacial band structure [9, 12].

Electronic Coupling between Molecule and Substrate

At interfaces with intermediate interactive strength and with chemisorption, processes based on electronic coupling between molecule and inorganic substrate may occur additionally and contribute to the interfacial electronic properties. Such processes include interfacial transfer of charge and energy, hybridization and the formation of chemical bonds.

When molecular frontier orbitals overlap in energy-momentum space with the valence states of the substrate, they can form hybridized states with shared charge carriers. The hybridized orbitals appear both shifted and broadened in energy-space [44–47]. As a result of the charge redistribution, also nuclear positions adjust to the shared charge density distribution and determine the shape of the hybridized state [40, 48]. The formation of a chemical bond can also be observed by characteristic energy shifts in the core levels of the involved surface atoms [49].

The concept of charge transfer has been interdisciplinarily studied for several decades due to its important role in fundamental and application oriented research [50]. Interfacial charge transfer considers the relative positioning between occupied and unoccupied states in both materials with respect to their E_{F} and E_{vac}. Thereby, different scenarios can be distinguished [12, 38, 40]: no charge transfer occurs, if ϕ of both materials is equal. Then, the concept of vacuum level alignment applies. Otherwise, charge transfer takes place and the alignment of both materials' E_{F} is the driving force and determines the direction and amount of charge transfer. Several models of charge transfer have been developed according to the type and strength of the interface and are listed below.

Charge Transfer at Hybrid Interfaces with Intermediate Interaction

At hybrid interfaces with intermediate interactions, where the hybridization between molecular frontier orbitals and substrate valence states is negligibly small, the transfer of integer charges by electron–vibration coupling or tunneling has been considered [46]. The transfer of electrons within or into molecules involves both electron–electron and electron–vibration interactions [52]. Transition rates are discussed within the Franck-Condon model, which will be introduced in a later section. The *Integer Charge Transfer Model* has been developed for predicting the energy level alignment at hybrid interfaces where electron transfer takes place via tunneling. This model is thoroughly reviewed in [12, 34] and [38].

Charge Transfer at Chemisorptive Hybrid Interfaces

At hybrid interfaces with non-negligible hybridization, the *Induced Density of Interfacial States Model* [13, 53] and the *Electrostatic Model* [54] were introduced to explain fractionally transferred charges. As a result of both charge and energy transfer, the band structure

at the interface is largely modified. Bands may shift, broaden and split [13, 45, 46, 55–57]. By redistribution of charges across the interface, surface dipoles are formed that alter the system's surface potential and work function [40–42]. As a rule of thumb, a strong chemical interaction at the interface can be identified by a broadening of the molecular frontier orbitals, a (partial) filling of the LUMO and an increase of its binding energy among other signatures.

Nevertheless, it should be noted, that the last two mentioned models describe the transfer of both charge and energy as macroscopic, spatially homogeneous quantities, which are typically represented in energy diagrams. This assumption appears obvious, as many experimental techniques, such as electronic transport measurements or photoemission experiments, measure laterally averaged quantities, e.g. ϕ_{hybrid}. However, a microscopic view on the localized nature of the interfacial potential is appropriate in systems with non-delocalized charges in the substrate and molecular layer each. Examples for such systems are hybrid interfaces with low adsorbate coverages or large molecular distances [58], with defect states [10, 59] or in systems where only a fraction of the adsorbates is involved in charge carrier transfer [46].

Thomas-Fermi Screening

The response of a substrate to a local charge is based on Coulomb interactions and the screening thereof. Within the semi-classical concept of *Thomas-Fermi screening*, this scenario is treated as the introduction of a local disorder potential to the substrate, which is pictured as a Fermi liquid. The mobile electrons within the substrate rearrange around the local charge Q, which leads to a reduction of the charge's bare Coulomb potential [60]

$$V_0(\mathbf{r}) = \frac{Q}{4\pi\varepsilon_0}\frac{1}{\mathbf{r}} \tag{2.1}$$

to a screened potential

$$V_{\text{screened}}(\mathbf{r}) = \frac{Q}{4\pi\varepsilon_0}\cdot\frac{e^{-\mathbf{r}/r_{\text{TF}}}}{\mathbf{r}} = \frac{V_0}{\varepsilon_{\text{r}}}. \tag{2.2}$$

Thereby, the dielectric functions in vacuum (ε_0) and in the material (ε_{r}) are considered and the real-space coordinate and the Thomas-Fermi screening length are denoted by $\mathbf{r}$ and r_{TF}, respectively. To estimate the length scale at which efficient screening in a material takes place and whether the approximation by a Fermi liquid is reasonable, equation 2.2 may be regarded with respect to the value of r_{TF}. Small screening lengths are provided by materials

with small values of r_{TF}. In quasi-two-dimensional materials, r_{TF} is given by

$$r_{\mathrm{TF}} = 2\pi e^2 \frac{N(E_{\mathrm{F}})}{A \cdot \varepsilon_{\mathrm{r}}} \tag{2.3}$$

with the unit cell area per atom A and the amount of electrons at the Fermi level $N(E_{\mathrm{F}})$ [60].

A hybrid interface, where local charges are introduced by the adsorbates, can be described in the framework of the *dielectric continuum model* [61], which is based on *Thomas-Fermi screening*. Thereby, the adsorbate layer is modeled as a quasi-two-dimensional layer with constant $\varepsilon_{\mathrm{r}} = \varepsilon_{\mathrm{ads}}$ and height h, that is sandwiched in between the semi-infinite substrate with constant $\varepsilon_{\mathrm{sub}}$ from below and vacuum with $\varepsilon_{\mathrm{vac}} = 1$ from above. The screened interaction between electrons in the sandwiched, quasi-two-dimensional adsorbate layer differs from the above-described three-dimensional case. In the sandwiched model, an effective two-dimensional dielectric function [61]

$$\varepsilon_{\mathrm{eff,ads}}(\hbar\mathbf{k}) = \frac{\varepsilon_{\mathrm{ads}}[1 - \tilde{\varepsilon}_{\mathrm{sub}}\tilde{\varepsilon}_{\mathrm{vac}}e^{-2h\hbar\mathbf{k}}]}{1 + [\tilde{\varepsilon}_{\mathrm{sub}} + \tilde{\varepsilon}_{\mathrm{vac}}]e^{-h\hbar\mathbf{k}} + \tilde{\varepsilon}_{\mathrm{sub}}\tilde{\varepsilon}_{\mathrm{vac}}e^{-2h\hbar\mathbf{k}}} \tag{2.4}$$

needs to be evaluated for the adsorbate layer, which depends on the momentum vector $\mathbf{k}$ and on the modified dielectric constants at the neighboring interfaces defined as $\tilde{\varepsilon}_{\mathrm{sub}} = \frac{\varepsilon_{\mathrm{ads}} - \varepsilon_{\mathrm{sub}}}{\varepsilon_{\mathrm{ads}} + \varepsilon_{\mathrm{sub}}}$ and $\tilde{\varepsilon}_{\mathrm{vac}} = \frac{\varepsilon_{\mathrm{ads}} - \varepsilon_{\mathrm{vac}}}{\varepsilon_{\mathrm{ads}} + \varepsilon_{\mathrm{vac}}}$ [63]. $\varepsilon_{\mathrm{eff,ads}}$ replaces ε_{r} of the adsorbate in equation 2.2 and accounts for a modified, lateral V_{screened} in the adsorbate layer caused by the presence of mobile charge carriers in the neighboring layers. Thereby, a local charge Q in the adsorbate layer interacts with the charges in the substrate and induces a charge rearrangement. This charge rearrangement can be pictured as the formation of an image charge with magnitude $Q \cdot \tilde{\varepsilon}_{\mathrm{sub}}$, that is located inside the substrate at an equal distance to the interface as the charge of the adsorbate [63]. An infinite series of image charges results from mirroring at the substrate/adsorbate and adsorbate/vacuum interfaces. The combination of the image charges with Q in the adsorbate layer forms a dipole potential in the direction of the surface normal, which adds to the image charge potential and locally modifies V_{screened} in the adsorbate layer at the dielectric interface [10, 64]. Note, that in laterally integrating measurements such as photoemission experiments an average vertical potential difference between adsorbate layer and substrate is obtained

$$\Delta V = \frac{4\pi\sigma}{\varepsilon_{\mathrm{ads}}} \cdot h \tag{2.5}$$

with the laterally averaged charge density σ, which is sensitive towards the height of the adsorbate layer.

2.2 Structural Alignment

The structural arrangement at the hybrid organic/inorganic interface is driven by a minimization of the interfacial potential energy. Various studies have concentrated on connecting different structural parameters to the electronic structure of the interface [56, 65]. Such parameters include the geometry of the substrate surface, the shape and size of the molecules as well as their adsorption height and coverage.

Adsorption Height

Regarding the parameter of adsorption height, a general tendency is observed that shorter molecule–substrate distances translate to stronger electronic couplings due to an increased overlap of the electronic valence states [18, 55, 66–71]. The increased overlap leads to larger push-back effects and encourages hybridization as well as charge transfer [41, 42]. Also bond formation was observed at strongly interacting interfaces, where charge transfer from the substrate resulted in a stabilization of the *pi*-electron system of planar, polycyclic, aromatic hydrocarbons [66, 68]. Exceptions to the rule can be found, when the molecule–substrate interaction is dominated by the push-back effect, which hinders a lowering of the adsorbate height contrary to charge transfer, hybridization or bond formation [72, 73].

Atomic Displacements

The interfacial potential landscape does not only impact the adsorption height, but results also in relative atomic displacements within the substrate and molecule in comparison to their isolated forms. Atomic relaxations are often more prominent in planar molecules than in 3D crystals, since resetting forces are much smaller in out-of-plane direction. Nevertheless, atomic relaxations may similarily affect the substrate as for example observed by adsorbate induced surface reconstructions [74]. The directions of the atomic displacements are informative about site-specific charge density variations within the molecule and the substrate, leading to either repulsive or attractive interactions. Such local charge differences can either reflect an intrinsic dipolar character of the molecule or they can be the result of selective charge transfer to specific molecular sites [75].

These effects can be illustrated on the example of the planar, polycyclic molecule CuPc: normal incidence x-ray standing wave experiments on CuPc have shown relative atomic displacements by $\sim 2\,\%$ and by $\sim 4\,\%$ for physisorptive and slightly chemisorptive interactions with the substrate, respectively [73]. Thereby, the chemisorptive interaction was mediated by the CuPc HOMO, which mainly resides at the nitrogen-based azaporphyrin ring surrounding the central copper atom. Thus, the largest atomic displacement and a movement

towards the substrate was observed for atoms within the azaporphyrin ring. In an atomic force microscopy experiment on the same molecule, individual molecules were negatively charged by an external source [76]. It was found that the additional charge resided at the central copper atom, which was displaced by $\sim 30\,\%$ away from the substrate due to a repulsive Coulomb interaction with the metal substrate. Note, that for charged adsorbates the interfacial potential is additionally altered by the image charges (see 2.1), which tends to lower ϕ and decrease the adsorption height [56].

Vibrational Motion

Another process, which leads to temporal rather than permanent atomic displacements, originates from vibrational movements in the molecules and from phonons in the substrate. The coupling between such vibrational movements to electronic transitions can be observed in spectroscopic experiments as a vibronic progression – a series of transitional states whose intensities and energetic separations are tied to vibration mode-, element-specific atomic displacements [77, 78]. The phenomenon of vibronic transitions and their properties are described by the Franck-Condon principle [79]. Thereby, electronic transitions are treated as decoupled from atomic movement (Born-Oppenheimer approximation), which is reasoned by the much larger atomic masses in comparison to the electronic mass. This renders atomic motion negligible on the time-scale of an electronic transition. Only after the excited charge equilibrates towards its new energetic minimum, a change in Coulomb interactions between electrons and nuclei gives rise to changes in the vibrational state of the molecule. At hybrid interfaces, the vibrational motion within adsorbates (and the substrate) can result in stronger electronic coupling to the substrate and lead to increased interfacial charge transfer [80].

Adsorbate Coverage

Aside from the adsorbate height, the adsorbate coverage is an essential aspect that imparts interfacial properties. In combination with the molecular shape, it controls the extent of electronic overlap between neighboring molecules and thus defines not only structural parameters as the relative molecule-to-substrate orientation [57, 81] but also surface-sensitive electronic parameters as the surface potential landscape or work function [56, 82, 83]. While some structural properties of the hybrid interface are predefined by the intrinsic shape and electronic structure of the chosen substrate and adsorbate, many parameters can be externally tuned during or after sample growth that influence the interfacial structure. One of such parameters is the molecular ordering atop the substrate, which may be controlled, e.g., by the sample temperature [84, 85].

Important to this thesis is the growth of homogeneously oriented molecules, which adsorb in a layer-by-layer manner with negligible intermolecular electronic overlap. This facilitates the interpretation of experimental results obtained for methods integrating over multiple adsorbate sites and allows for comparison with theoretical results on computationally less-demanding models such as an isolated molecule or a single adsorbed molecule. A suitable growth method of choice for obtaining such hybrid interfaces is organic molecular beam deposition (OMBD) [81, 85, 86] employed in ultra-high vacuum (UHV) conditions. Thereby, a well-ordered layer-by-layer growth can be achieved when growth parameters and materials are chosen such that the strength of molecule–substrate interactions exceeds intermolecular forces.

2.3 Dynamic Processes and Excitation Pathways

This section addresses the dynamical aspects of electronic and structural arrangement at hybrid interfaces. The processes behind forming chemisorptive or physisorptive interfaces can typically be distinguished by their time scales.

Forming a chemisorptive interface is based on a chemical reaction where bonds break, form and rearrange. This requires spatial overlap between the electronic wavefunctions of the involved states, so charge can migrate between both wavefunctions and form a bound state. Thereby charge initially oscillates between both states until an equilibrium is reached after several hundreds of attoseconds up to a femtosecond [50, 87]. After the bond has been formed, its charge density can be viewed as static. Thus, chemisorptive interfaces are often associated with adiabatic processes where nuclei remain static.

Physisorptive interfaces, on the contrary, rely on van-der-Waals interactions and due to the push-back effect the molecules appear to 'float' atop the substrate. Charge transfer processes at such non-covalently bound interfaces require vibronic coupling between both components with typical vibronic oscillation times of a few tens to hundreds of femtoseconds [88, 89].

Time Scales of Selected Dynamic Processes

A selection of dynamic processes and their time scales are presented in Figure 2.1. The assorted values are adapted from several publications reviewing ultrafast dynamics in solid inorganic and organic materials as well as at hybrid organic/inorganic interfaces [87, 90–98]. Processes that are based on the movement of electrons, such as screening or inner shell recombinations, are traceable on the attosecond time scale. A similar time scale is associated with the photoemission process, which can promote bound electrons into unoccupied states below or above the vacuum level. The latter case is labeled as 'ionization', while the filling

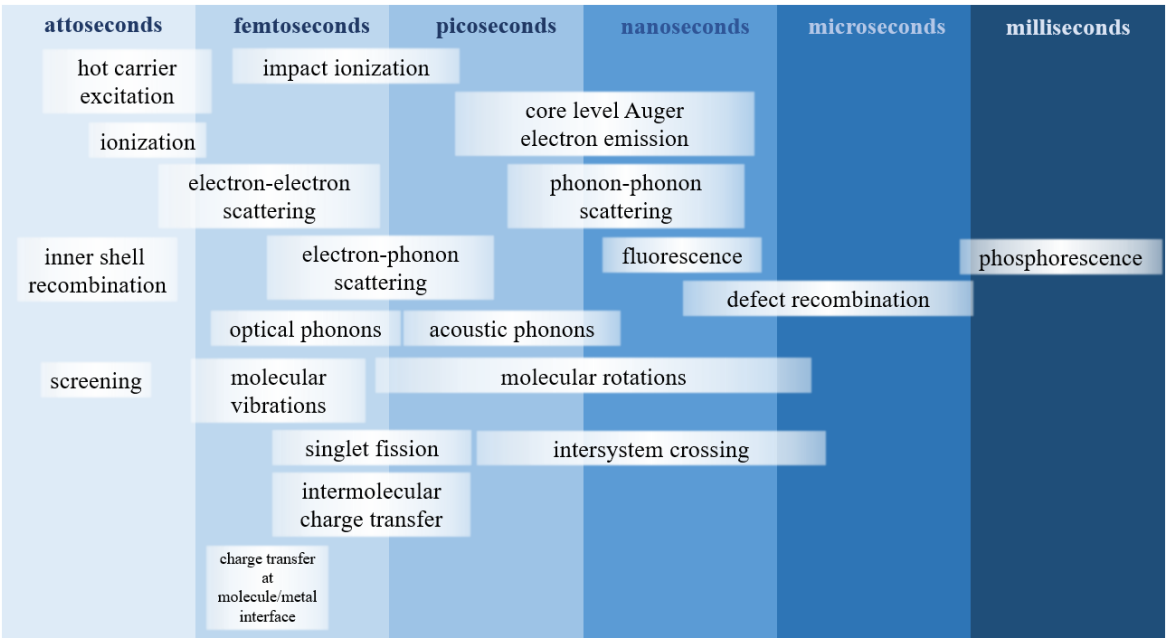

Figure 2.1: Time scales of selected dynamic processes in inorganic and organic materials as well as at hybrid organic/inorganic interfaces. Based on [87, 90–98].

of states below the vacuum level refers to excitation of 'hot carriers'. The wording 'hot carrier' originates from the consideration of a system's electronic temperature, which may reach a few thousands of Kelvin during photoexcitation [99].

The fastest processes involving atomic movement occur on a time scale that is an order of magnitude slower. With oscillation periods of a few tens of femtoseconds, molecular vibrations and optical phonon modes in the inorganic substrates can mediate coupled processes such as interfacial and intermolecular charge transfer, the consecutive structural relaxation of excited state molecules as well as the thermalization of hot carriers. The thermalization of hot carriers describes their step-wise cooling process initiated by electron–electron scattering within few femtoseconds, followed by electron–phonon scattering on the picosecond time scale and finally heat dissipation by phonon–phonon scattering. This last step may take up to several hundreds of nanoseconds until thermal equilibrium is reached in an externally excited sample. Note, that while electronic temperatures may reach several thousands of Kelvin during photoexcitation, the local temperature of the lattice typically only increases on the order of $\sim$ 20 K for excitation powers of $\sim 1 \frac{\mathrm{GW}}{\mathrm{cm}^2}$ [100].

Photoexcitation of samples often initiates a series of processes following the hot carrier relaxation pathway, which may lead to the emission of electrons, for example by Auger scattering, or to the emission of photons by, e.g., inner shell recombination, fluorescence, defect recombination or phosphorescence. To maximize the photon harvest, the design of organics-based devices often exploits mechanisms based on charge and energy transfer by

spin flips as in singlet fission or intersystem crossing. Another large field of application oriented research is surface catalysis. Thereby, adsorbed molecules undergo a chemical reaction, which may be mediated by vibronic coupling to the photoexcited substrate, and then they desorb within several hundreds of femtoseconds to picoseconds when excess electronic energy is converted into vibrational energy [101].

Hot Carrier Excitation

In this thesis, the photoexcitation induced dynamics of hybrid interfaces are studied within a time frame ranging from about 100 fs to a few picoseconds. On this time scale, the dynamics are mainly governed by the excitation of hot carriers, followed by their thermalization. Both, excitation and thermalization may involve hot carrier scattering at electrons, phonons and molecular vibrations and can thus take various pathways involving several substrate, adsorbate or hybrid interface derived states. A goal of dynamic interface studies is to trace and identify these pathways, e.g., by their characteristic time scales, temperature and energy dependencies as well as momentum distributions.

Primary Hot Carriers

Four mechanisms resulting in the creation of hot carriers are presented and sketched in Figure 2.2. The most direct scenario is the absorption of a photon $h\nu$ resulting in an interband transition (Fig. 2.2 A). The created hot electron (black circle) and hot hole (white circle) are vertically separated by the photon energy (green arrow) and reside on the occupied part (grey shaded area) and unoccupied part (white shaded area) of separate bands, respectively. The time scale for such a direct transition is in the attosecond to few femtoseconds range (see Fig. 2.1) and the occurrence of directly excited carriers is obviously tied to the vertical accessability between initial and final states at the given (small) photon energy. If these conditions are not satisfied, hot carrier excitation via an intraband excitation is possible (Fig. 2.2 B). A requirement for this process is the existence of a partially filled band crossing E_F, so electrons can be excited from the occupied part into the unoccupied part of the same band. Such an indirect transition typically involves two components: adsorption of a photon for a change in energy and a scattering process which provides the necessary change in momentum (dashed, horizontal black arrow) of the hot electron. At elevated temperatures, scattering with phonons dominates over scattering at defect states or the surface potential, thus the time scale and also the probability of an intraband transition is mainly dictated by the electron-phonon coupling time τ at room temperature and the material's dielectric function [100].

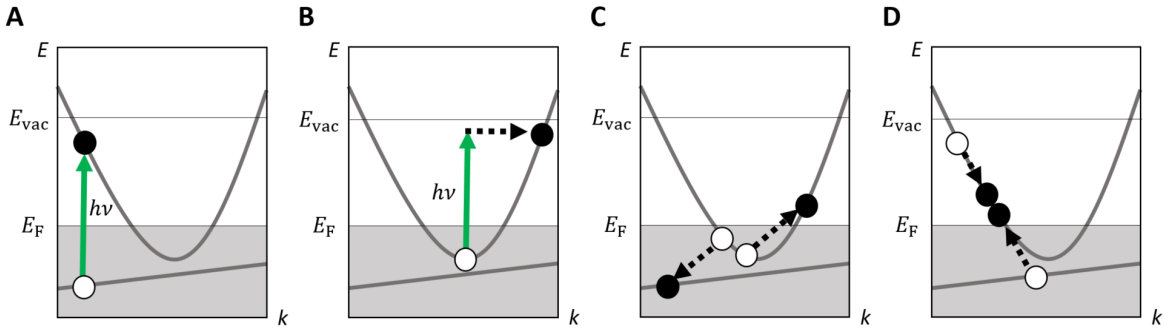

Figure 2.2: Excitation mechanisms of hot carriers. **A** Direct interband excitation of hot electrons (black circle) and hot holes (white circle) by photon absorption (green arrow), **B** indirect intraband excitation involving photon absorption and a scattering process (dashed, black arrow), which leads to a change of the hot electron momentum. **A** and **B** result in the creation of primary hot carriers. Secondary hot carriers are created by **C** Auger scattering and **D** impact ionization. Adapted from [100, 102].

Within the Drude model, the frequency (ω)-dependent dielectric function is given by $\varepsilon(\omega) = 1 - \frac{\omega_p^2}{\omega(\omega+i/\tau)}$ with the plasma frequency $\omega_p = 4\pi Ne^2/m_0$ in a free-electron gas and the electron mass m_0. Hence, its value holds information on the amount of electron-phonon scattering processes (by τ) as well as on electron-electron or hole-hole scattering processes by the amount of available charge carriers N.

Secondary Hot Carriers

The hot carriers excited by photons as shown in Fig. 2.2 A and B are labeled as primary hot carriers. As soon as they are excited, they start to thermalize and relax by scattering towards E_F [103]. As a result of these scattering processes, a cascade of secondary hot carriers may be created by two mechanisms sketched in Fig. 2.2 C and D.

In C, charge carriers near E_F interact by an Auger process. Thereby, an electron recombines with an energetically lower hot hole. To conserve both energy and momentum, a second electron is lifted to an energetically higher state. This process leads to a decay of photogenerated hot holes and may increase the number of secondary hot electrons above E_F. Note, that the initial state of the involved electrons must not necessarily be located below E_F as depicted here. Instead, Auger scattering may similarly involve hot electrons above E_F.

The process in D describes an inverse mechanism and is labeled in literature as *inverse Auger scattering* or *impact ionization* [100, 102, 104]. Thereby, a high-energy hot electron interacts with a low-energy electron in the valence band. By transfer of energy and momentum, two low-energy secondary hot electrons are created above E_F.

Note, that the creation of secondary hot carriers is connected to the relaxation and thermalization of primary hot carriers. Initially, the thermalization is governed by inelastic

electron-electron and hole-hole scattering processes. Based on the Drude model, the lifetime of a hot carrier is proportional to $\omega_p^{-1}(E - E_F)^{-2}$. Thus, the relative energy of hot carriers to E_F is essential as well as the amount of charge carriers available as scattering candidates (given in ω_p). The latter is largely defined by the material's band structure. In various noble metals, the excitation energy dependence of hot carrier generation and their lifetimes has been extensively studied, all yielding lifetimes below 100 fs at room temperature [100, 105, 106]. At similar conditions, the hot carrier dynamics measured in materials with lower N close to E_F, as for example in van-der-Waals layered 2D materials, are about one to two orders of magnitude slower [104, 107, 108]. This is reasoned not only by their lower density of states at E_F, but also by the dominance of phonon scattering during hot carrier thermalization [109].

From an application-based point of view, relaxation mechanisms at hybrid interfaces are favorable which result in radiative decay (fluorescence, phosphorescence) or in the creation of excitons, which are electron–hole pairs with binding energies within the system's bandgap. The magnitude of exciton binding energies as well as excitonic lifetimes are important parameters for optimizing the device's function. While electronic applications as OPV favor small binding energies for efficient charge carrier separation, large exciton binding energies are desired for high recombination rates in optical applications as OLED. Thus, extensive static [110] and dynamic [111] studies have characterized the influence of molecular shape, interfacial structural and electronic alignment on the localization and lifetime of excitonic wavefunctions. Time scales between few femtoseconds to picoseconds have been measured for exciton creation, tied to intra- and intermolecular as well as interfacial charge transfer. Nevertheless, no evidence for the creation of excitonic states was found within this thesis, considering the chosen materials and experimental parameters. Therefore, no further discussion of excitonic states will be provided here and the interested reader is referred to [111].

3 Experimental Conditions and Methods

In this chapter, experimental conditions, measurement techniques and setups are described that are used for the characterization of hybrid organic/inorganic interfaces in this thesis.

3.1 Experimental Conditions

For systematic studies on hybrid interfaces, it is essential to control and maintain their electronic and structural properties. Keeping the samples under UHV conditions (pressures below 10^{-8} mbar) helps not only to control sample growth but also to minimize sample contamination by undesired adsorption of gaseous atmospheric particles. Such particles may raise two issues: firstly, they might intercalate in the sample and act as defect states, altering the interfacial structure and electronic properties. Secondly, they might cover the sample and thereby limit the accessability of the hybrid interface by surface sensitive measurement techniques. Based on Langmuir's adsorption model [112], the temporal variation of adsorbate coverage C_{ads} on a substrate can be approximated by

$$\frac{d}{dt}C_{\mathrm{ads}} = \frac{p_{\mathrm{ads}} \cdot S}{\sqrt{2\pi m_{\mathrm{ads}} k_{\mathrm{B}} T}} - v_{\mathrm{des}} \cdot e^{-\frac{\Delta H}{k_{\mathrm{B}} T}} \cdot C_{\mathrm{ads}} \tag{3.1}$$

with the adsorbate partial pressure p_{ads}, the adsorbate mass m_{ads}, Boltzmann constant k_{B}, sample temperature T, sticking coefficient S, activation energy of desorption ΔH and desorption coefficient v_{des}, which describes the amount of times that an adsorbed particle attempts to overcome its adsorption potential [113]. The right hand side of this equation consists of two terms, the first describing the adsorption rate and the second describing the desorption rate of a particle. When both processes equilibrate a saturated adsorbate coverage is reached. The simplest way to prolong this time scale and to reduce sample contamination is by ensuring UHV conditions.

In this thesis, all studied hybrid interfaces were kept in vacuum chambers with UHV conditions. During *in-situ* sample growth, a base pressure of 10^{-9} mbar was maintained in the preparation chamber and the samples were kept at a base pressure of 10^{-10} mbar during characterization. At 10^{-9} mbar, the contamination coverage typically saturates only after 14 days as compared to after few seconds at ambient pressure [114]. Within this work, measurements were conducted for up to 16 h on one sample. Static XPS measurements reveal that a negligible contamination with coverages of less than 0.1 monolayers occurred

on this time scale.

Although equation 3.1 is based on a simplified model, which assumes a homogeneous substrate and no interactions between adsorbates, it sets the basis for the technique 'organic molecular beam deposition' (OMBD) by which the hybrid interfaces in this work were fabricated. OMBD is based on the adsorption and desorption of gaseous molecules on a substrate, which are provided by a Knudsen cell. By varying parameters such as the Knudsen cell temperature and the cell-to-substrate-distance, p_{ads} in equation 3.1 can be tuned. Separate control over the temperatures at the substrate and the Knudsen cell allows for regulating the adsorbate mobility on the substrate surface, an important factor which comes into play, e.g., on substrates with surface corrugations and energetically inequivalent adsorption sites. The impact of substrate and Knudsen cell temperature as well as deposition rate on controlled multilayer growth should be mentioned: as these parameters can influence the relative substrate-adsorbate versus adsorbate-adsorbate interactions, various structural adsorbate arrangements may be obtained. The reader is referred to literature for in-depth reviews on the principles of OMBD and different growth modes [81, 85, 86] as well as for material specific growth studies on the adsorbates pentacene and CuPc [67, 115, 116].

The second impact of substrate contamination is a reduced accessibility of the hybrid interface by surface sensitive measurement techniques. In this thesis, measurement techniques are employed which are based on the emission of electrons from matter. Thereby, only those electrons with energies above a certain threshold can overcome the surface potential and can be detected. Thus, energy-loss channels via, e.g., inelastic electron-electron scattering greatly impact the detected electron intensity by reducing the electrons' inelastic mean free path. Although the cross section for electron-electron scattering events depends on the material specific dielectric function ε_{r} (see chapter 2), a universality in the relationship between electron energy and electron mean free path in different materials has been proposed [117]. Thereby, the shortest inelastic mean free paths of about 1 nm are found for electron energies in the UV-range. For electron energies in the soft x-ray-range, the inelastic mean free path increases by about half an order of magnitude. Even though the universality, which was initially proposed by Seah and Dench [117], has been questioned by later works [118, 119], it may be used as a guideline for estimating the probeable volume below the sample surface by electron-based measurements.

3.2 Experimental Methods

3.2.1 Photoelectron Spectroscopy

Photoelectron spectroscopy is an established measurement technique for accessing a sample's electronic bandstructure [49, 120]. It is based on the photoelectric effect [121, 122] and is realized by an energy-selective detection of electrons, which are emitted from a sample as the result of photon absorption. When illuminating a sample with light, an electron can be emitted if the photon energy $h\nu$ is larger than the sample's workfunction ϕ. The kinetic energy E_{kin} of the electron above the vacuum level is related to its binding energy E_{bin} inside the solid via

$$E_{\mathrm{kin}} = h\nu - \phi - E_{\mathrm{bin}}. \tag{3.2}$$

The electron may be accellerated to E'_{kin} when entering the potential of the spectrometer. However, in an experimental setup, sample and spectrometer share a common ground potential so that their chemical potential is equal. Thus, E_{bin} can still be determined from the detected E'_{kin} via

$$E_{\mathrm{bin}} = h\nu - \phi_{\mathrm{spec}} - E'_{\mathrm{kin}}, \tag{3.3}$$

if the work function of the spectrometer ϕ_{spec} is known. Note, that in some conventions the initial energy of a bound electron inside the solid is expressed as $E - E_{\mathrm{F}} = -E_{\mathrm{bin}}$ where the energies of occupied states take negative values.

The obtained intensity distribution of detected electrons is representative for the photoemission process: it includes the signature of the sample's bandstructure in its photoexcited state and it depicts the interaction of the photoemitted electron with its surroundings.

Such interactions can the manifest themselves in the spectrum among other effects as a broadening of peaks in energy with a Lorentzian lineshape, a renormalization in $\mathbf{k}$ and as additional peaks next to the main line, which are collectively termed *satellites*. Satellites can have their origin in electron–electron interactions, as well as in interactions of the photoelectron with other (quasi-)particles. As a result, the photoelectron's kinetic energy is altered and an increased background intensity of *secondary electrons* is observed towards lower E_{kin} of the main peak. Processes creating satellites include inelastic scattering at other electrons or phonons, excitation of plasmons, formation of excitons and so-called shake-up processes. A shake-up process involves the excitation of two electrons by one photon [123, 124]. While one electron is energetically lifted into a bound, unoccupied state, a second electron is photoemitted. The kinetic energy of the photoemitted electron is reduced by the amount of energy necessary for exciting the first electron. In other words this process

is also denoted as *internal scattering* between a photoemitted core-electron and an excited valence-electron.

Detailed photoemission models are discussed in literature, e.g., by Damascelli [120] and Hüfner [49]. Since the intensity profile of photoelectron energies is material-specific, this approach was initially applied by Siegbahn in experiments for chemical analysis, which set the basis for photoelectron spectroscopy (PES) [125].

3.2.1.1 Angle-resolved Photoelectron Spectroscopy

As an extension of PES, angle-resolved photoemission spectroscopy (ARPES) detects the azimuthal and polar angle of the emitted photoelectron in addition to its E'_{kin}. This allows for mapping the sample's bandstructure in energy-momentum space.

When the photoelectron is emitted, its momentum component perpendicular to the sample surface $\mathbf{k}_{\perp}$ changes at the potential step between sample and vacuum. Its momentum component parallel to the sample surface $\mathbf{k}_{||}$, however, can be viewed as conserved when the photon momentum remains negligibly small. This assumption is typically made in experiments with photon energies below 100 eV [49]. Then, $\mathbf{k}_{||}$ can be related to the polar emission angle θ via

$$\mathbf{k}_{||} = \frac{1}{\hbar}\sqrt{2m_0 E'_{\mathrm{kin}}}\sin(\theta). \tag{3.4}$$

The individual momentum components in x- and y-direction ($\mathbf{k}_{||} = \sqrt{{k_x}^2 + {k_y}^2}$) are determined as

$$k_x = \frac{1}{\hbar}\sqrt{2m_0 E'_{\mathrm{kin}}}\sin(\theta)\cos(\varphi) \tag{3.5}$$

and

$$k_y = \frac{1}{\hbar}\sqrt{2m_0 E'_{\mathrm{kin}}}\sin(\theta)\sin(\varphi) \tag{3.6}$$

with the azimuthal emission angle φ.

The obtained bandstructure $I(E'_{\mathrm{kin}}, k_x, k_y)$ is connected to the sample's electronic, optical and structural properties. From the relative energetic positioning between electronic states and E_{F}, electronic and optical properties can be derived. The dispersion of a state $E'_{\mathrm{kin}}(\mathbf{k}_{||})$ relates to the character of involved orbitals as well as their distance and orientation in space. Since orbital shape and orientation are closely linked to atomic positions in the sample, also structural properties can be (indirectly) drawn from the electronic bandstructure. A combined experimental and theoretical approach – *orbital tomography* – relies on this connection between orbital shape and molecular structure and allows for reconstructing real-space molecular orbitals from the measured momentum distribution of non-dispersing molecular states [126]. This allows to gain insight into structural properties of a single molecule such

as its adsorption angle [127] or vibronic progression [77]. Note, that in some ARPES experiments the probed surface area integrates over few hundreds of μm^2 [6] and signals from a multitude of molecules are detected at once. Thus, it is essential to investigate samples with well-defined long-range order for a reconstruction of molecular orbitals. The measured signal can then be interpreted as a sum over intensities stemming from individual molecules and conclusions on single molecules can be drawn.

3.2.1.2 X-ray Photoelectron Spectroscopy

A PES experiment performed with excitation energies in the soft x-ray range or x-ray range is labelled as a x-ray photoelectron spectroscopy (XPS) experiment. Compared to ARPES in the UV-range, E_{kin} is increased in XPS, which allows for probing a larger sample volume in real space and for accessing higher $\mathbf{k}_{||}$ in reciprocal space. XPS is widely used for a qualitative as well as quantitative analysis of elements within a sample's surface [128]. By means of reference values from literature [124], the measured peaks, which appear at different binding energies in the spectrum, can be attributed to specific elements in the sample. Even individual species of an element, which appear shifted in binding energy due to their different chemical environments, may be distinguished. When comparing the relative peak areas of different elements, the stoichiometry of a compound sample can be evaluated. For this quantitative analysis, parameters inherent to the experimental setup and studied E_{kin} as well as sample and orbital specific parameters need to be considered, which can be taken from references values in literature [129].

In this work, XPS was applied to determine the adsorbate coverage of layer-by-layer grown molecules atop a substrate. Therefore, several XPS spectra were taken and compared for varying adsorbate coverages. Since increasing adsorbate coverage simultaneously results in damping of the substrate peaks I_{sub} and in increasing adsorbate peaks I_{ads}, it is sufficient to only evaluate the relative peak intensity changes of one of them. Following the Lambert-Beer law, the substrate peak intensity $I_{\text{sub}}(n)$ covered by n ($n \in \mathrm{N}$) closed adsorbate layers with thickness d decreases exponentially:

$$I_{\text{sub}}(n) = I_0 \cdot \mathrm{e}\left(\frac{-nd}{\lambda_{\text{ads}}\cos(\theta)}\right). \tag{3.7}$$

I_0 refers to the substrate peak intensity without any adsorbate coverage and λ_{ads} describes the inelastic mean free path within the adsorbate layer. For coverages in between closed adsorbate layers, I_{sub} decreases linearly with the covered surface proportion c_{cov}. Thus, a general formula for describing I_{sub} with incomplete adsorbate layer coverages is given by:

$$I_{\text{sub}}(n, c_{\text{cov}}) = c_{\text{cov}} \cdot I_{\text{sub}}(n) + (1 - c_{\text{cov}}) I_{\text{sub}}(n-1). \tag{3.8}$$

3.2.2 X-ray Photoelectron Diffraction

From an experimental view, x-ray photoelectron diffraction (XPD) and XPS experiments can be conducted in the same manner and photon energy range and thus equally access surface sensitive, chemically and locally resolved information. The interpretation of the data, however, focusses on the spectral shape of core levels in XPS, whereas in XPD it focusses on their momentum distribution. In this sense, XPD acts as an equivalent to ARPES or orbital tomography in the (soft) x-ray-range: the measured momentum-dependent intensity distributions hold information on the emitting orbital, its orientation in space and on the exciting light polarization.

Additional to the electronic information held by the directly emitted electron wave, structural information is encoded in additional momentum-dependent intensity modulations, which result from elastic scattering events of the photoelectron. In the framework of the three-step photoemission model [49, 120], such elastic scattering events can be pictured in an electron wave picture (see Fig. 3.1 A): as an electron is emitted from its initial state, e.g., an atomic site (black), its wave function (blue circles) travels through the sample. When it is elastically scattered at the Coulomb potential of a neighboring atom, a phase-shifted secondary wave (yellow and red circles) is created, which is centered around the scattering atom (grey). The interference between the directly emitted and secondary waves results in a momentum-dependent intensity modulation, which is unique to the emitting site. For a selected spectral peak, the measured momentum distribution is an incoherent sum of all intensities stemming from individual emitting sites. The observed scattering induced intensity modulations are characteristic to extrinsic as well as intrinsic factors. Intrinsic factors are, for example, the electrons' mean free path, the Z-dependent scattering cross-sections of the surrounding atoms and their local arrangement relative to the emitting atom. Extrinsic factors include E_{kin} of the emitted electrons, the experimental geometry, which defines the angles between sample, incident light and the detector, and the sample temperature. Since the local sample structure distinctly influences the measured momentum distribution, XPD has become an established method for determining site-specific atomic arrangements with chemical sensitivity and atomic resolution [130–135].

While the structure-sensitive information is in principle also retrievable from ARPES or orbital tomography measurements in the UV-range [136–139], the characteristic features become more discernible at higher excitation energies that allow for probing of core levels. The reasons for this are tied to the excitation energy and the probed initial states: in XPD typically core levels serve as initial states, which are spatially confined to an emitting atom. In contrast, ARPES/orbital tomography measurements in the UV-range probe valence states, such as molecular orbitals, which are delocalized over several atoms. The confinement of

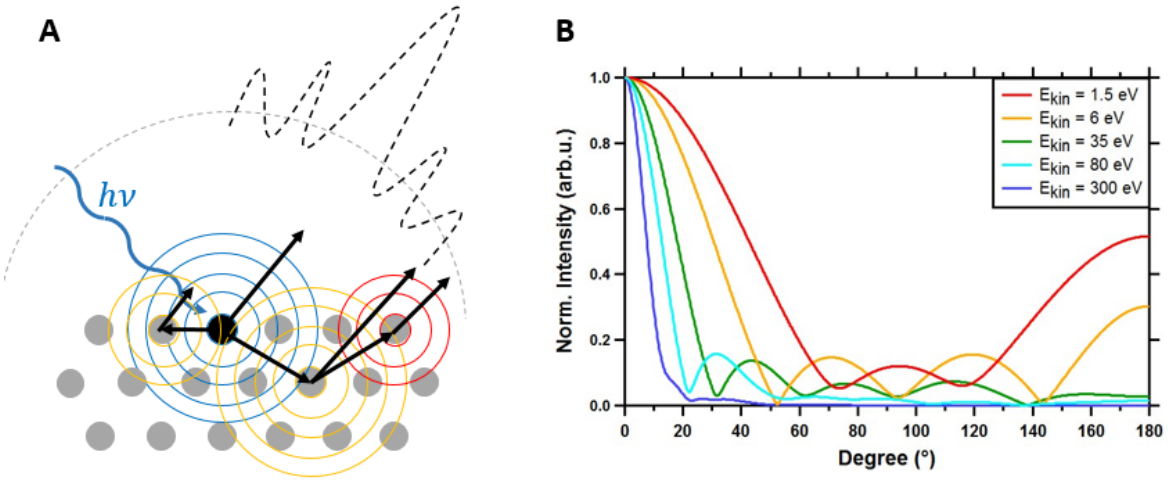

Figure 3.1: A Schematic of photoelectron diffraction. The emitter atom is colored in black, neighboring atoms in grey. The unscattered electron wave is pictured by blue concentric circles, scattered waves by yellow and red circles. The direction of electron scattering is marked by black arrows and the resulting momentum dependent intensity modulation is sketched by the black, dashed line. **B** Calculated angular dependency for photoelectrons scattered at an Ag atom. For higher E_{kin} forward scattering is dominant while backscattering becomes more significant for lower E_{kin}. (The calculation is printed with permission of Christian Metzger.)

the emitting state to a single atom in XPD reduces the amount of inequivalent scattering events that superimpose the measured intensity distribution. This facilitates the distinction and interpretation of scattering features in comparison to emission and scattering from a molecular orbital, where the amount of inequivalent neighboring scatterers is significantly larger [139].

A further consequence of increased E_{kin} in XPD is an altered directionality of scattering events. This is exemplarily shown in Fig. 3.1 B for scattering of photoelectrons of different E_{kin} at a silver atom. While electron scattering with E_{kin} in the UV-range is ocurring rather isotropically with low momentum dependence, forward scattering becomes mostly prominent for higher E_{kin}, thus resulting in more pronounced distinct features. The presence of pronounced features greatly facilitates the interpretation of experimental data and thus XPD experiments are preferably performed at higher E_{kin}. The calculation in B was performed by Christian Metzger based on a model of independent atomic centers [127, 140].

Lastly, and especially important for studying adsorbate interfaces is the increased electron mean free path in XPD. This allows to detect scattering occuring at sample depths of a few nanometers, which enables the determination of adsorbate heights, relative substrate-to-molecule orientations, intramolecular distortions and even adsorption sites [133, 137, 141]. To extract this structural information from the experiment, a comparison to model simulations is vital. Therefor, the momentum distribution resulting from an initially assumed sam-

ple geometry is compared to the experiment and altered iteratively until the highest possible agreement between experiment and simulation is reached. After qualitatively bringing the position of simulated and experimental features into agreement, the quantitative agreement is typically determined by the so-called R-factor [26]

$$\mathrm{R} = \frac{\sum_{k_x,k_y}[\xi(k_x,k_y) - \xi_0(k_x,k_y)]^2}{\sum_{k_x,k_y}[\xi^2(k_x,k_y) + \xi_0^2(k_x,k_y)]^2}. \tag{3.9}$$

The R-factor compares the so-called modulation functions ξ and ξ_0 of the two momentum maps, which are obtained by a pixel-wise (k_x,k_y) data normalization via

$$\xi(k_x,k_y) = \frac{I(k_x,k_y) - I_0(k_x,k_y)}{I_0(k_x,k_y)}. \tag{3.10}$$

These modulation functions represent the intensity modulations in each momentum map which are introduced due to the presence of scatterers. For their evaluation, knowing the intensity distribution in the presence of zero scatterers $I_0(k_x,k_y)$ at the corresponding energy is required. From the experimental data, $I_0(k_x,k_y)$ can be estimated as a mean of momentum maps extracted closely below and above the energy of the examined spectral feature. In the R-factor analysis, values closer to zero indicate a better agreement between the compared momentum maps.

3.2.3 Time-resolved Photoemission Experiments

By means of pulsed light sources and a timing mechanism, dynamic processes can be observed in time-resolved photoemission experiments. Such a timing mechanism is implemented in tr-PES by varying the arrival time of two different light pulses at the sample surface. The so-called 'pump pulse' is chosen to have an energy smaller than the sample's work function. It drives the system out of equilibrium and excites hot electrons into unoccupied states below E_{vac} (see Fig. 3.2 A, red arrow). The energy of the so-called 'probe pulse' is larger than the sample's workfunction and can emit electrons from the sample for detection (blue arrow). By means of a delay stage within the pump pulse's beam path, the pulse's path length can be mechanically altered, which results in a relative shift in time at which the pump and probe pulse arrive at the sample. Introducing this temporal shift, or pump-probe delay time τ_{delay}, allows for imaging the evolution of the sample's bandstructure by taking 'snapshots' in time.

How well a dynamic process can be experimentally resolved, depends on the number of snapshots taken, their temporal spacing (τ_{delay}) and on the temporal resolution during one snapshot. This temporal resolution (see Fig. 3.2 B, blue line) is defined by the convolution

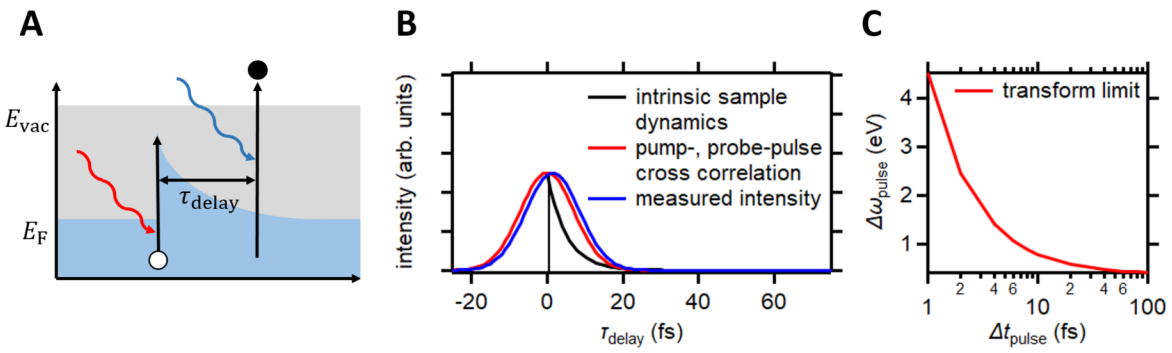

Figure 3.2: A Schematic depiction of a pump - probe pulse based photoemission experiment. The pump pulse (red arrow) excites electrons above E_F at $\tau_{delay} = 0$ and the probe pulse (blue arrow) samples the systems evolution after τ_{delay}. **B** Schematic illustration of the measured temporal resolution in an experiment (blue line), which is given by the convolution of the intrinsic sample dynamics (black line) and the pump- and probe pulse cross correlation (red line).**C** Transform limit for gaussian shaped pulses based on the energy-time uncertainty relation.

of the pulse shapes in time of both pump and probe pulse (red line) with the intrinsic sample dynamics (black line). Naturally, temporal pulse widths Δt_{pulse} shorter than the sample's intrinsic dynamics are desired for good sampling. The temporal width of a pulse, though, co-depends on the energetic pulse width $\Delta\omega_{pulse}$ as described by the energy-time uncertainty relation

$$\Delta\omega_{pulse} \cdot \Delta t_{pulse} \geq \frac{\hbar}{2}. \tag{3.11}$$

Therefore, a trade-off between temporal and energetic resolution needs to be made when designing an experiment (see Fig. 3.2 C).

3.2.3.1 Time-of-Flight Momentum Microscope

A critical step when performing a time-resolved photoemission experiment is the coordination of the pump and probe pulses' arrival time and space at the sample surface. Both, spatial and temporal overlap may be created by means of a time-of-flight momentum microscope setup [4, 6, 142] shown in Fig. 3.3. Such a momentum microscope can be operated in two different modes that either directly image the real space sample surface or the corresponding momentum space. The *real space mode* allows for a straight-forward analysis of the space at which the pump and probe pulses impinge on the sample as well as of their lateral extent on the surface ('spot size'). Absolute numbers for the spot sizes can be evaluated by comparing their extent to well-defined in-plane structures on a calibration-sample ('chessy sample' [6]). Both, pump and probe beam (red/blue and black lines, respectively) are coupled in from the same port into the analyzer chamber at a polar angle of $\theta = 68°$. Deviations from both beams' spatial overlap at the sample surface can be mechanically compensated, e.g., by

adjusting lense settings of the optical laser or by changing the relative orientation between the incoupling port and the sample surface. After spatial overlap is assured, their temporal overlap when arriving at the sample surface needs to be calibrated. This calibration is less straight-forward and typically took several hours to days at the beginning of the experiments in this work. Spatial overlap, on the other hand, was typically created within less than one hour.

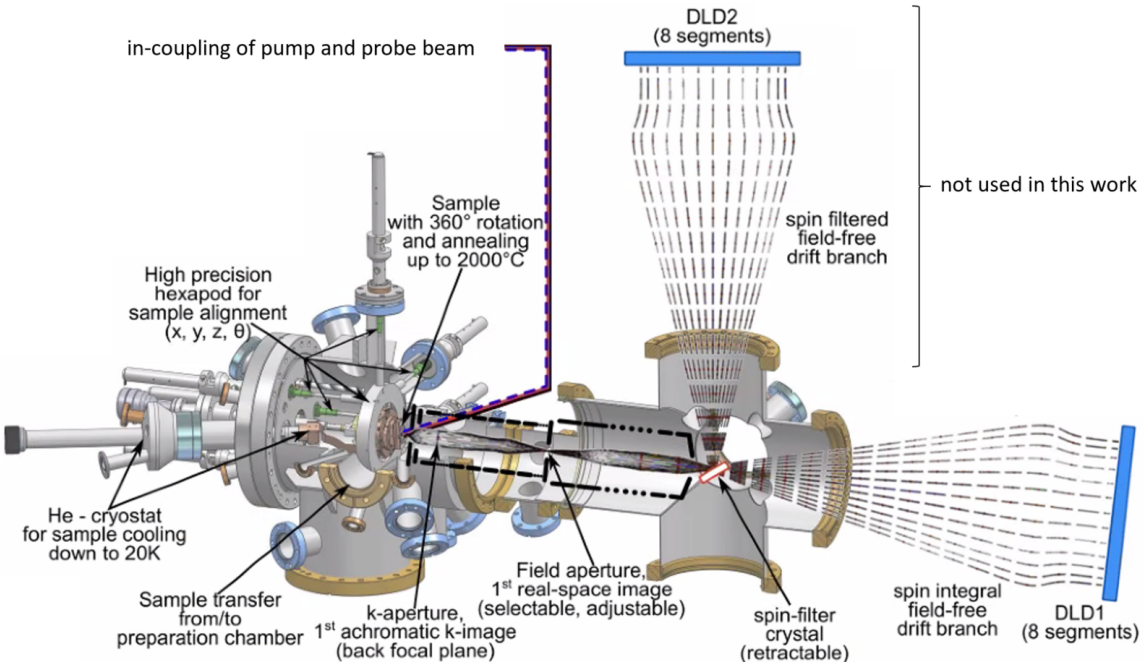

Figure 3.3: Schematic depiction of the analyzer chamber with integrated time-of-flight momentum microscope and excitation pulse structure at the beamline PG2 *FLASH* at DESY. No spin-selective measurements were performed for the projects in this thesis and only the right time-of-flight detector tube (DLD1) was used as a detector. Image adapted from [6].

To verify temporal overlap, or *time zero* (t_0), a specific trigger event needs to be found, which indicates the simultaneous arrival of both pulses. Such trigger events are described in ref. [6] and include scanning over a wide range of τ_{delay} while looking for excitation induced changes in the sample's bandstructure, for example the broadening or shifting of bands, the population of states above E_{F} or signs of the laser-assisted photoemission effect (LAPE). LAPE is based on the interaction between the emitted photoelectron with the electric field of the pump pulse, which results in the detection of sidebands [143]. These sidebands are replica of the main peak and are located energetically on both sides of the main line at a distance corresponding to the pump photon energy. They are present only for the duration of the pump pulse and are thus a good indicator in the search for t_0.

Once t_0 is found, photoelectrons can be detected with a delay line detector based on their momentum and flight time t_{tof} through the microscope's drift tube (bottom right drift tube

with delay line detector DLD1 in Figure 3.3). With knowledge of the drift tube's length l_{drift} (= 800 mm [6]), the kinetic energy of the photoelectrons can be determined via

$$E_{\text{kin}} = \frac{m_0 \cdot l_{\text{drift}}^2}{2t_{\text{tof}}^2}. \tag{3.12}$$

The delay line detector is segmented into two times four quadrants with independent multi channel plates. The second set of four quadrants is placed behind the first stack and rotated by 45° respectively. This allows for a simultaneous detection of up to four electrons, which is then followed by a 150 ps recovery time [6]. In momentum-sensitive measurements, as in XPD, a careful pixel-wise background correction needs to be performed during data evaluation in order to avoid an artificially uneven background intensities related to the detector segments. Ultimately, by means of this time-of-flight momentum microscope a four-dimensional dataset of $I(E'_{\text{kin}}, k_x, k_y, \tau_{\text{delay}})$ can be obtained with a field of view of ~ 4.8 Å^{-1} in $\mathbf{k}_{||}$. Thereby, structures in momentum space are resolved with an accuracy below 0.1 Å^{-1} while the energy resolution stays below 100 meV for excitation energies in the UV-range [4, 6]. Note, that while photoelectrons of all E'_{kin} are detected in an experiment, only those within a choseable energy window of ~ 7 eV are detected with high energy-resolution.

Space charge

A significant problem to time-resolved photoemission experiments in general and specifically to this type of time-of-flight momentum microscope is the so-called *space charge effect* [6]. It results in the loss of momentum information and in an (asymmetric) broadening of spectral features in energy. While the energetic broadening can be corrected - to some extent - during postprocessing of the data [144], the information loss on the electrons' momenta remains irretraceable as it has a stochastic origin. Thus, minimizing the occurrence of space charge is an essential step at the beginning of an experiment.

The space charge effect is based on the interaction between photoemitted electrons and arises within the spectrometer's drift tube, which the electrons pass with different velocities. While the 'electrons of interest' are typically directly emitted by the probe pulse and have thus a 'large' E_{kin}, the majority of emitted electrons are subject to inelastic scattering events and thus create a cloud of charge carriers above the sample which moves slowly towards the detector. Depending on their relative position in the drift tube, the fast moving electrons experience an acceleration or deceleration due to Coulomb interactions with the slow moving electron cloud.

Next to this deterministic interaction, which leads to a τ_{delay}- and $\mathbf{k}_{||}$-dependent energy broadening, stochastic electron-electron scattering additionally impacts the fast moving

electrons' momenta. Both, scattering and Coulomb interactions scale with the density of charge carriers in the 'slow' electron cloud. Thus, reducing the amount of emitted slow electrons is a reasonable method for minimizing the space charge effect. Ways to do so are, for example, by choosing a large band gap substrate to reduce the amount of secondary electrons created by the probe pulse, or by attenuating the pump pulse's fluence to reduce the amount of slow electrons excited via multi-photon absorption. The latter method was chosen during the measurements in this work, although, this required making a trade-off between the suppression of space charge and the efficiency of excited states per probed sample volume. The space charge effect is considered to be negligibly small, when no momentum- and time-dependent energy broadening characteristic to space-charge in the used momentum microscope is observed [6, 144].

3.2.3.2 Light Sources

In this work, time-resolved photoemission experiments were performed in cooperation with members working at *European EuXFEL* (Schenefeld, Germany), DESY (Hamburg, Germany), University of Hamburg and Kiel University (Germany). The time-of-flight momentum microscope described in section 3.2.3 served as a mobile endstation and experiments were conducted at both a HHG table-top laser light source at the University of Hamburg and at the FEL source *FLASH* at DESY.

High-Harmonic Generation

By means of high-harmonic generation, femtosecond light pulses in the UV-range are made available to laboratory-based table-top laser sources [145–148]. The working principle is shown in Fig. 3.4 A and is based on the interaction between an intense laser beam with gas atoms. The oscillating electromagnetic field of the so-called *driving laser* (red curve) periodically distorts the Coulomb potentials of the gas atoms (black curves). Thereby, an electron (black circles) may tunnel through the lowered side of the Coulomb barrier and ionize the atom. When the laser's electromagnetic field is of opposite sign, the emitted electron is accelerated back towards the ionized atom and when electron and ion recombine, a high energy photon (blue arrow) is emitted collinearly with the driving laser.

The energy of the emitted photon can be tuned by the choice of gas atoms, their density as well as by the energy and intensity of the driving laser [148]. Here, a Ti:Sapphire laser (Wyvern 1000, KM-Labs) with a wavelength of $\sim 790\,\mathrm{nm}$ ($= 1.58\,\mathrm{eV}$) serves as driving laser (see black box in Fig. 3.4 B). By means of a beam splitter, its output is separated into two branches. One of these branches serves as the pump pulse source (bottom red line), the other branch passes through an Argon filled capillary, where the higher harmonics are

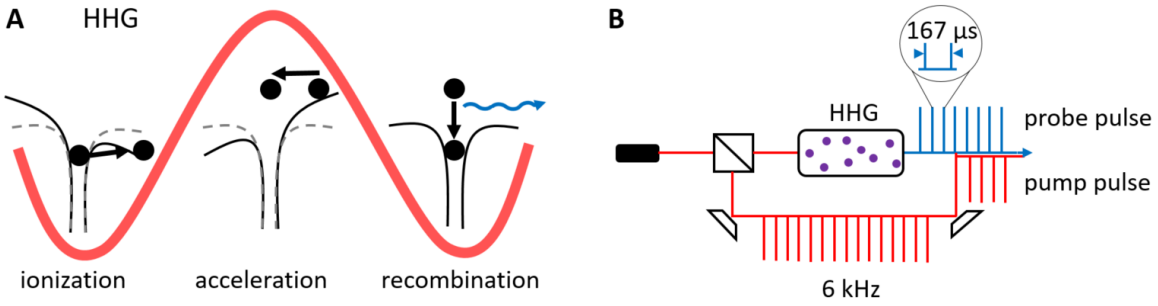

Figure 3.4: A Working principle of high harmonic generation. **B** Schematic depiction of beam paths and pulse structures for the laboratory based HHG light source.

generated. With aluminum filter foils and a monochromator, the fundamental wavelength and other higher harmonics are blocked and only the selected higher harmonic is guided towards the sample as the probe pulse source. A detailed description of this setup and its characterization can be found in literature [4].

The temporal structure of the pump and probe pulses are both defined by the same source – the driving laser, which is operated at a repetition rate of 6 kHz with a pulse length of ~ 50 fs (FWHM) and pulse energy of ~ 0.5 mJ. Thus, time zero may be found relatively quickly by comparing the path lengths of both branches. The repetition rate of 6 kHz corresponds to a temporal spacing of 167 μs between two consecutive pulses, which is well above the detector cool down time and the timescales of any thermalization processes within the studied samples. At the sample surface, a pump–probe pulse cross correlation of (95 ± 5) fs is determined with spot sizes of about $(100 \times 400)\ \mu m^2$. With additional filter foils the initial pulse energy of ~ 0.5 mJ is reduced down to several tens of nJ in order to avoid significant space charge effects. In this work, pump - probe based experiments were conducted with pump pulse energies of 1.58 eV and probe pulse energies of 36.3 eV, which allowed for a time-resolved characterization of valence band dynamics.

Free-Electron Laser

The free-electron laser source *FLASH* is able to provide pulsed radiation with fundamental wavelength energies in the UV- to the soft x-ray-range (14 eV - 310 eV) [5, 6, 149]. Due to the existence of higher harmonics, also core level states with energies up to ~ 800 eV can be efficiently probed with the third harmonic and time-resolved studies by tr-XPS and tr-XPD can be conducted. The lasing principle of *FLASH* is based on self-amplified spontaneous emission (SASE), which is detailed in ref. [150] and sketched in Fig. 3.5 A: a bunch of electrons ('macrobunch') is passing through an undulator (green and orange blocks), which forces their trajectory onto a sinusoidal curve (black arrow). The accellerated motion of

the electrons results in spontaneous emission of photons with a characteristic fundamental wavelength, which is defined by the magnet spacing in the undulator. Interactions between the emitted light and the electrons leads to so-called microbunching, a density modulation within the macrobunch, which results from either an accelleration or a deceleration of electrons depending on their relative phase to the light inside the undulator. The light emitted by each microbunch will coherently add up and create a pulsed probe beam structure as depicted in Fig. 3.5 B (blue line).

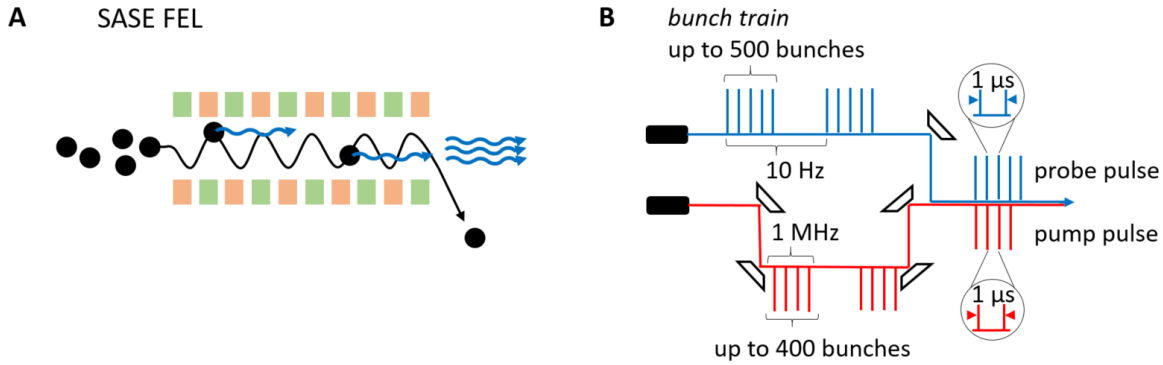

Figure 3.5: A Working principle of an self-amplified spontaneous emission based free electron laser. **B** Schematic depiction of beam paths and pulse structures for the free electron laser *FLASH* (DESY) light source.

The pulse structure consists of macrobunches, or 'bunch trains', at a repetition rate of 10 Hz. Each bunch train provides up to 500 pulses (microbunches), which are separated by 1 μs (1 MHz). Thus, an effective repetition rate of up to 5 kHz is obtained. Contrary to a HHG setup, here, a separate laser serves as a pump pulse source (red line). Thus, establishing temporal overlap between both sources is typically more complicated. This pump laser has a fundamental wavelength energy of 1.58 eV, which may be increased to 3.16 eV via a frequency doubling crystal (BBO). The pulse structure of the pump laser is similar to the probe pulse structure but with maximal 400 microbunches per bunch train. Therefore, a measurement includes both pumped and unpumped spectra which need to be individually selected and analyzed.

The lasing at *FLASH* is subject to statistic fluctuations as a result from the spontaneous emission process and parameters such as beam arrival time (jitter), pulse energy and intensity can vary for each pulse. In order to disentangle these parameters, a data aquisition (DAQ) program is provided by the *FLASH* facility, which allows for accessing the experimental conditions for each individually detected electron. With the detection of each electron, approximately 30 additional parameters are collected that include, e.g., the electron's coordinates on the detector, its specific time-stamp, information on the macro- and microbunches such as jitter, fluence, energy, the position of the delay stage and further

parameters specific to the beamline. Due to the vast amount of data collected during a measurement it is useful to preselect, sort and integrate over a few parameters of interest on the local *FLASH* server before transferring smaller datasets to a personal computer for further data evaluation.

A few noteable parameters characterizing the light source are a pump–probe pulse cross correlation of (180 ± 10) fs, a spot size of about $(260 \text{ x } 150)\,\mu\text{m}^2$ for the pump laser and of $(200 \text{ x } 100)\,\mu\text{m}^2$ for the probe laser. The probe pulse energy of $\sim 30\,\mu$J was further attenuated by thin film filter foils and nitrogen gas for space charge suppression. Similarily, the pump pulse laser with a maximum energy of 1 mJ per pulse was attenuated to provide fluences of few tens to hundreds of $\frac{\mu\text{J}}{\text{cm}^2}$.

4 Results

In this chapter, two hybrid organic/inorganic interfaces are discussed: a bilayer of pentacene molecules atop an Ag(110) crystal and a monolayer of CuPc molecules atop the transition metal dichalcogenide (TMDC) $TiSe_2$. The tr-PES experiments on these interfaces were first conducted at a HHG source in June 2018 for pentacene/Ag(110) and in July 2020 for CuPc/$TiSe_2$, followed by similar experiments at the *FLASH* FEL source in August 2018 and in August 2020, respectively. The time resolved momentum mapping experiments of the pentacene/Ag(110) valence region were the first of their kind conducted at a FEL source. Thus they were initially intended as a proof-of-principle showcase addressing whether molecular thin film samples would withstand the high intensity radiation of the FEL. With our study, we show not only the feasability of such an experiment by mapping molecular frontier orbitals on a femtosecond time scale, but also reveal a dynamic interplay between electronic and structural motion at the hybrid interface upon photoexcitation. In order to further elaborate on visualizing and understanding combined electronic and structural dynamics at hybrid organic/inorganic interfaces, we combined three modalities of tr-PES – tr-ARPES in the UV range, tr-XPS and tr-XPD in the soft x-ray range – during the consecutive beamtime on CuPc/$TiSe_2$. Thereby, we accessed the transient electronic and structural properties of the interface from both valence band as well as core level energies. This combined approach allows us to identify and trace a uniquely large charge carrier transfer interaction between $TiSe_2$ and $\sim 45\,\%$ of the CuPc molecules, which affects the overall bandstructure, the intrinsic relaxation dynamics of $TiSe_2$ and the molecular structure on a sub-picosecond timescale. With this study we do not only showcase the potential of FEL-based tr-PES experiments, but we also present a hybrid material system in which photoexcitation leads to a macroscopic manipulation of the interfacial electronic and atomic structure on an ultrafast time scale. Such an interplay may potentially have future application in light-driven, molecular scale devices.

4.1 Pentacene atop Ag(110)

The results shown in this chapter have been published in Nature Communications [30] with the title 'Ultrafast orbital tomography of a pentacene film using time-resolved momentum microscopy at a FEL'. They are a combined experimental and theoretical study in collaboration with M. Reuner, C. Metzger, D. Kutnyakhov, M. Heber, F. Pressacco, C.H. Min, T.R.F. Peixoto, M. Reiser, C. Kim, W. Lu, R. Shayduk, M. Izquierdo, G. Brenner, F. Roth, A. Schöll, S. Molodtsov, W. Wurth, A. Madsen, D. Popova-Gorelova, M. Scholz and F. Reinert.

4.1.1 Materials Overview

Pentacene ($C_{22}H_{14}$) is a polycyclic hydrocarbon consisting of five linearly joined benzene rings. Its structural arrangement in various thin film and bulk structures as well as its electronic properties have been extensively studied in the past [115, 151–158]. Owing to its properties such as large hole mobilities and the potential to overcome the Shockley-Queisser limit in solar energy conversion by singlet fission [159], pentacene has found application in organic photovoltaics (OPV) [160], OFET [8, 161, 162] and was recently also implemented in a MASER (microwave amplification by stimulated emission of radiation) prototype [163]. For applications, the interface between organic material and metal contact plays a decisive role in the device performance. Thereby, the relative orientation between molecule and metal surface significantly impacts the alignment of energy levels and the dynamic transfer of charge across the interface [9, 86]. Thus, control over the dynamic aspect of the device performance requires studying the interplay between structure and charge flow across the interface on a femto- to picosecond time scale.

When pentacene is deposited on top of Ag(110), the metallic substrate and the pentacene molecules in direct contact (first layer) show a strong chemisorptive interaction, which manifests itself in a well ordered, flat-lying molecular growth and an electron transfer from the substrate into the (former) LUMO [153]. Molecules adsorbed in consecutive layers, though, remain electronically largely decoupled and are not involved in interfacial charge transfer. This translates also to their adsorption geometry: depending on the conditions during sample growth (Knudsen cell temperature, deposition rate, substrate temperature) pentacene molecules continue to grow either almost flat lying with a slight tilt along their long molecular axis (6° and 8.5° for molecules in the first and second layer, respectively) [153] or they may adsorb in a standing way, similar to when deposited atop semiconducting or insulating substrates [115, 152, 154, 164].

Sample Growth

In this work, a pentacene bilayer with (almost) flat-lying adsorption geometry was chosen, according to the structure determined in ref. [153]. The sample was prepared at a base pressure of $3{\cdot}10^{-9}$ mbar via OMBD. Before adsorbate deposition, the Ag(110) crystal (1 cm diameter) was cleaned by several cycles of annealing at ~ 600 K and Argon sputtering for 30 min at 1.5 kV. The cleanliness and homogeneity of the crystal were judged by XPS and LEED measurements, respectively. A LEED image taken at room temperature of an Ag(110) crystal considered as clean is shown in Fig. 4.1 A. After waiting for the substrate to cool down to room temperature, pentacene (99 % purity, purchased from Sigma Aldrich) was deposited at a Knudsen cell temperature of 473 K and a Knudsen cell-to-sample-distance of ~ 20 cm. A deposition time of ~ 30 min was evaluated for deposition of a monolayer from growth characterization by means of XPS and LEED measurements. This time was evaluated by means of XPS measurements for two samples with different adsorbate coverages. For this, a sample with an adsorbate coverage slighty above one monolayer is prepared and the intensity of a substrate-derived core level peak is evaluated. Then, a reference sample with monolayer coverage is prepared by tempering the initially prepared sample for 30 min at 315 K. The intensity of the same substrate-derived peak is evaluated once again. With knowledge of the deposition time for the initially prepared sample, the monolayer deposition time is obtained from the relative intensity difference of the damped peaks with help of equations (3.7) and (3.8). The evaluation by XPS is supported by LEED measurements of both samples. It has been shown in literature [151, 153], that the LEED pattern of flat-lying pentacene on Ag(110) shows distinct coverage-dependent changes for coverages below two layers. Since the growth of molecules in the first and in the second layer is incommensurate, they create distinguishable reflexes in a LEED experiment. The relative intensities of reflexes belonging to each layer can thus be used as a guide for estimating the adsorbate coverage with an accuracy of ~ 0.2 layers.

Sample Characterization

The distinct LEED patterns of a pentacene monolayer with a molecular superstructure of (3 -1/-1 4) and of a bilayer atop Ag(110) are shown in Fig. 4.1 B and C, respectively. For the bilayer, reflexes belonging to the first layer are overlaid by additional reflexes from molecules in the second layer with a molecular superstructure of (5 2/-2 3). The obtained superstructures contain information on intermolecular distances and reveal a packing density lowered by ~ 13 % within the second layer in comparison to the first layer. Considering the repulsive interaction between neighboring pentacene molecules, the lowered molecular density again emphasizes a decreased interactive strength between the substrate and the

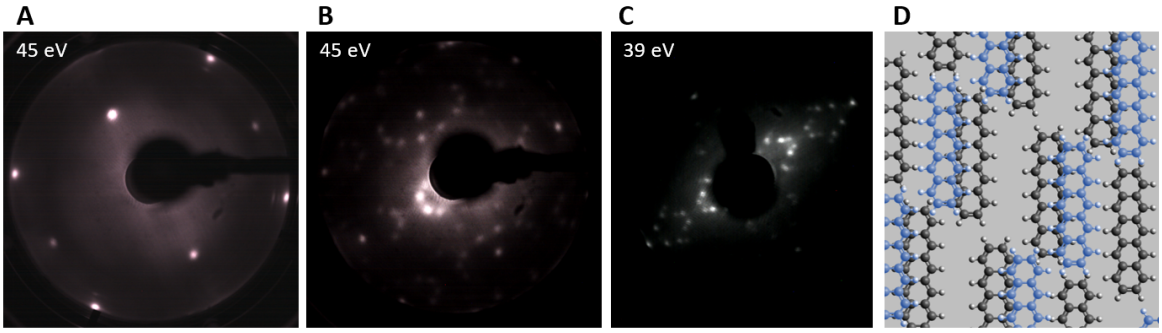

Figure 4.1: Structural sample characterization. LEED characterization of **A** an Ag(110) crystal surface taken at 40 eV, **B** a pentacene monolayer atop Ag(110) taken at 40 eV and **C** a pentacene bilayer atop Ag(110) taken at 39 eV. **D** Schematic depiction of a possible molecule arrangement for a pentacene bilayer atop Ag(110). Molecules in direct contact to the substrate are colored in black and molecules in the second layer are colored in blue.

second layer. Since a characterization by LEED does not reveal adsorption sites, at least 13 different configurations between molecules within the first layer (black) and within the second layer (blue) may exist. An exemplary configuration is shown in Fig. 4.1 D. The relative orientations and large intermolecular distances between neighboring molecules in each layer result in a negligibly small orbital overlap and molecules can be viewed as isolated from each other. While an interaction may be possible between molecules in the first and second layer, their electronic coupling is assumed to be small as well, since the LEED superstructures of the first and second layer are non-commensurable.

The interactive strength between the substrate and molecules in the first layer is reflected by their adsorption height. In literature, no experimentally determined values are found for pentacene atop Ag(110). Calculations performed by M. Reuner and D. Popova-Gorelova as part of the publication discussed in this chapter, estimate an adsorption height of 2.2 Å. In their model, the distance between a cluster of Ag atoms and a pentacene molecule was lowered until an electron transfer into the former LUMO-type orbital was observed, as in the experiment. In literature, comparable values are determined by x-ray standing wave (XSW) and scanning tunneling microscopy (STM) measurements on similar material systems: pentacene atop Cu(111) forms a chemisorptive interface with an adsorption height of 2.43 Å [165] and PTCDA, a molecule similar to pentacene, has an adsorption height between 2.3 Å and 2.6 Å atop Ag(110) [166]. Pentacene atop Ag(111) or atop Au(111), on the other hand, forms physisorptive interfaces with adsorption heights above 3.0 Å [165, 167].

4.1.2 Time-resolved Characterization

Two major questions motivated the FEL-based time-resolved characterization of the pentacene bilayer atop Ag(110): firstly (1), would the organic thin film withstand the radiation fluences provided by the FEL and pump laser? If yes, would an identification of molecular features be possible by probing on a sub-picosecond time-scale? Secondly (2), would the chemisorbed first layer behave differently from the physisorbed second layer under the chosen pump-probe excitation conditions, and if yes, how?

Establishing Experimental Parameters and Gauging the Feasability of the Experiment

It is known that organic samples are prone to UV- or x-ray-radiation induced damage [168]. Also, interactions with low-energy electrons may lead to breaking and reordering of bonds in molecules [169]. As a result, features associated with molecular orbitals may appear distorted, broadened and shifted in energy in a tr-PES experiment [170]. Also additional states – defect states – may appear within the sample's bandgap as the atomic and electronic structure of the interface is significantly altered. In some cases, these radiation damage induced modifications are viewed as positive assets as for example in photodoping or photomicromachining [171, 172]. However, for a pump-probe based characterization, radiation-induced damage to the interface would negatively affect the unambiguous identification of electronic states. Most of all, irreversible changes would prevent an integration over data from several pump-probe cycles thus impeding a time-resolved characterization.

To answer the first question, the experimental conditions needed for minimizing radiation damage and the space charge effect were established in the beginning of the beamtime at the beamline PG2 of *FLASH* (DESY, Hamburg, Germany). For mapping molecular frontier orbitals, a FEL-probe energy of 35 eV was chosen. Based on literature values for bandgaps in pentacene thin films, which are ~ 3 eV for a monolayer of upright standing pentacene molecules atop Bi(111) [164] and ~ 2.5 eV for a flat-lying pentacene monolayer atop Au(111) [173], a pump excitation energy of 3.2 eV was chosen here. The pump laser provided a maximum flux of 1 mJ/cm^2 and the average FEL pulse energy of 30 μJ was attenuated such that the measured spectra resembled spectra from literature obtained by static PES [153].

In Fig. 4.2 A, the experimental geometry is depicted with pump and probe pulses (both *p*-polarized) impinging at a polar angle of 68° and an azimuthal angle of 64° to the [-110] direction of the Ag(110) crystal surface. The pulse structure provided an effective repetition rate of 3.3 kHz with 330 pulses per bunchtrain. The first 299 of these pulses were correlated with the pump laser and the last 31 pulses remained unpumped. A temporal scan sampling

over 3 ps with a temporal resolution of (215 ± 10) fs and energy resolution of ∼ 80 meV was measured within ∼ 6 h on one sample. After this time, a fresh sample was prepared in order to reduce sample-aging effects. To evaluate radiation damage, the irridiated sample position was changed every 30 min to an area with untouched molecules by moving the motorized sample stage of the time-of-flight momentum microscope.

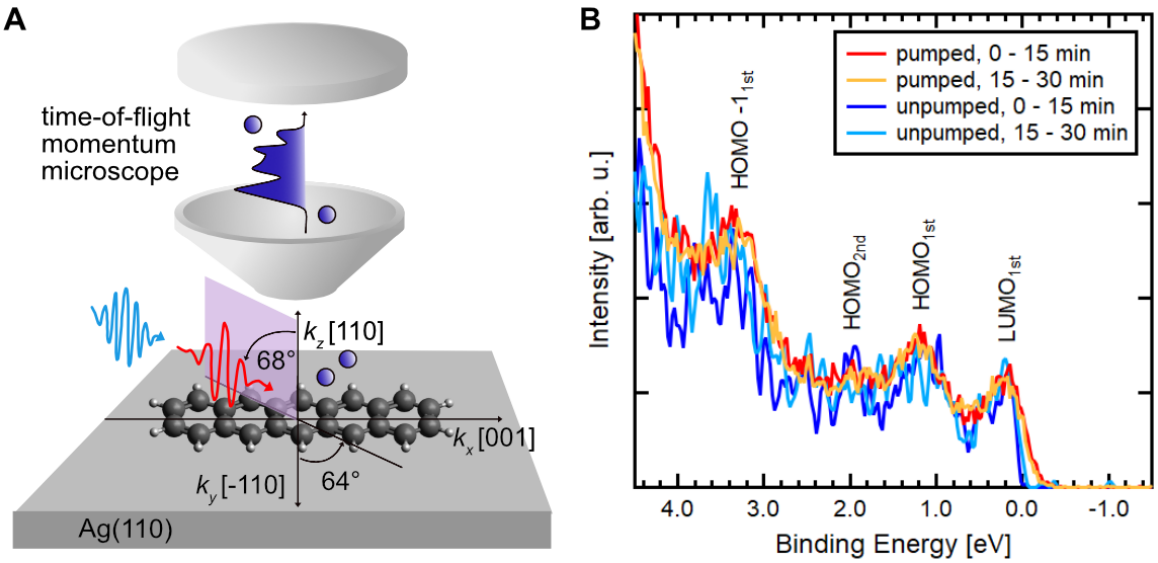

Figure 4.2: Experimental setup and estimation of radiation damage. **A** Schematic depiction of the measurement geometry with pump (red arrow) and probe (blue arrow) pulses exciting the hybrid pentacene/Ag(110) interface and detection of photoelectrons (blue circles) by a time-of-flight momentum microscope. **B** Pumped (red, orange) and unpumped (dark and light blue) energy distribution curves for the pentacene bilayer/Ag(110) valence region taken between minutes 0-15 (red and dark blue) and minutes 15-30 (orange and light blue) during a measurement on one single sample position. Features associated with molecular orbitals in the first and second layer are labeled by the subscripts '1st' and '2nd', respectively. The spectra are normalized in intensity at $E_b = 2.2$ eV.

During data analysis, the 330 spectra obtained per macrobunch were divided into pumped and unpumped spectra and further sorted by the duration of the experiment. Then, pumped and unpumped spectra were individually evaluated and compared at different time stamps during a 30 minute measurement on one single sample position. In Fig. 4.2 B four energy distribution curves (EDCs) are shown, which are integrated over a measurement duration of 15 min each. For pumped (red and orange) as well as unpumped (dark and light blue) spectra, one EDC represents the spectral shape within the first (red and dark blue) and last (orange and light blue) 15 min. Due to the lower amount of unpumped pulses per macrobunch, the unpumped EDCs have a larger signal-to-noise ratio. Nevertheless, all four spectra exhibit distinct features similar to static spectra from literature [153], which are derived from molecular orbitals belonging to the first and second pentacene layer. They are

labeled with the subscripts '1st' and '2nd', respectively. These non-dispersive, molecular orbital derived features have an energetic width of about 500 meV and are well resolvable within the experimental energy resolution. Note, that the features in the pumped spectra appear slightly broadened in energy as a result of the time resolved sampling (see chapter 3.2.3), the increased local (electronic and phononic) temperature and due to space charge effects, which are discussed below. No radiation induced changes are observed when comparing the EDCs obtained during the first and last 15 min on one single sample position. It is thus concluded, that little to no radiation damage occured within 30 min of measurement at the same position with the chosen excitation parameters.

This absence of radiation damage came to a surprise, as the used pump laser energy of ~ 1 mJ per pulse was much higher than, e.g., the excitation energy of ~ 1 nJ per pulse used in a two-photon photoelectron spectroscopy (2PPE) study of pentacene thin films [164]. The absence of radiation damage in this work is explained by an efficient thermalization of the photoexcited carriers at the pentacene/Ag(110) interface. Thermalization of hot carriers describes the process of re-establishing thermal equilibrium between the electronic and phononic temperatures in the sample, e.g., by electron-electron, electron-phonon and phonon-phonon scattering processes. In a metallic substrate such as Ag(110), the thermalization process is efficient due to the large amount of available charge carriers near E_F (see chapter 2.3). Due to the small organic layer thickness at the bilayer pentacene/Ag(110) interface, hot carriers also created in the molecular layers can efficiently thermalize by coupling to these metallic states.

Based on the similarity of pumped and unpumped spectra, we could showcase the feasability of FEL-based tr-PES experiments in the UV-range at the example of the pentacene bilayer /Ag(110). Below, the similarity and assignment of molecular orbitals is further confirmed by comparing the momentum-resolved, pumped data to static calculations and to unpumped data from literature [153].

Identification of Molecular Orbitals

In Fig. 4.3 A-D, experimental photoelectron momentum maps (PMMs) integrated over 500 meV around the central binding energy of the $\mathrm{LUMO}_{1\mathrm{st}}$, $\mathrm{HOMO}_{1\mathrm{st}}$, $\mathrm{HOMO}_{2\mathrm{nd}}$ and $\mathrm{HOMO\text{-}1}_{1\mathrm{st}}$ are shown. The data is pump-probe pulse excited, but integrated over all τ_{delay}. From comparison to static calculations on isolated pentacene (Fig. 4.3 F-I), the observed main features at $k_x \approx \pm 1.2$ Å^{-1} can be clearly assigned to states of molecular orbital-type.

The calculations (performed by M. Reuner and D. Popova-Gorelova) are based on the plane-wave approximation for the photoelectron's final state, as described by P. Puschnig *et al.* [110] for reconstructing molecular orbitals from PMMs by orbital tomography. Thereby,

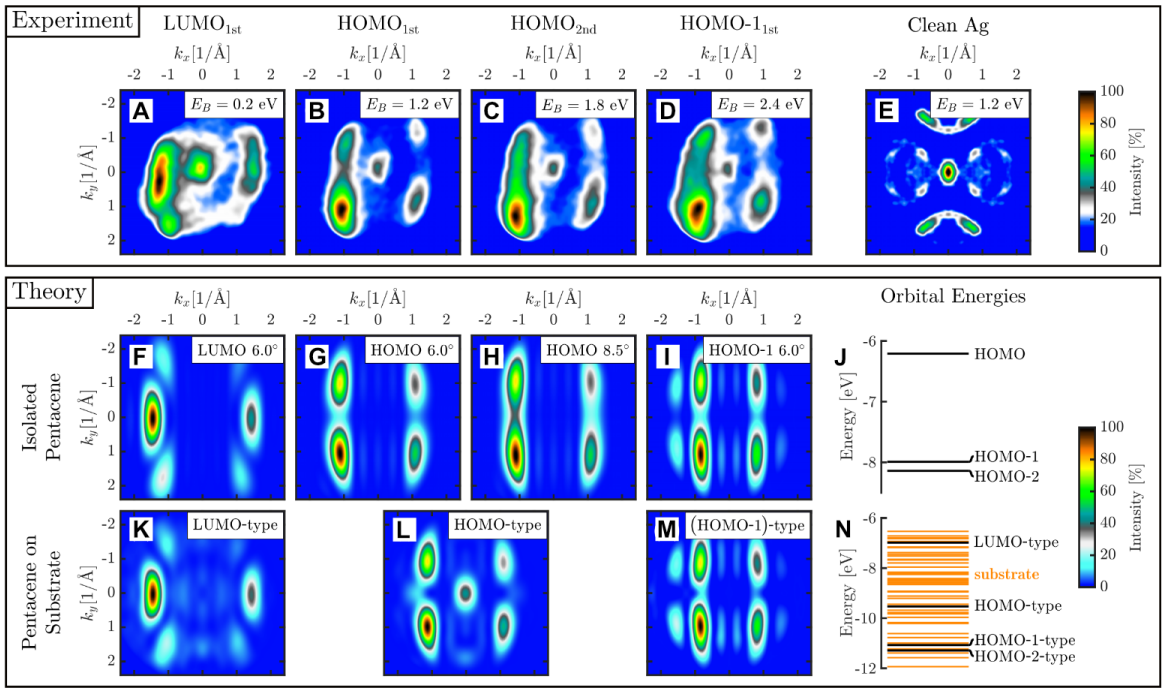

Figure 4.3: Comparison between experimental, pump-probe excited and time-integrated PMMs of a pentacene bilayer atop Ag(110) with calculated PMMs. Experimental PMMs for **A** the partially filled $LUMO_{1st}$, **B** the $HOMO_{1st}$, **C** the $HOMO_{2nd}$, **D** the $HOMO\text{-}1_{1st}$ and **E** clean Ag(110). The data in **E** is unpumped and symmetrized. Calculations on isolated pentacene (**F**-**I**), with a tilt angle denoted in the top right corner of each image, and on pentacene atop a cluster of Ag atoms (**K**-**M**) allow for an assignment of features in the experimental PMMs to molecule and substrate derived features. Hartree-Fock energies for molecular(-type) orbitals calculated for **J** isolated pentacene and **N** pentacene on substrate. Molecular orbital-type energies are colored in black and substrate-derived states in orange. Absolute energy values are irrelevant, but the relative shift of orbital energies towards lower energies (= higher E_B) in **N** indicates a strong molecule-substrate interaction.

a PMM of a molecular orbital is related to the squared Fourier transform of a Dyson orbital, which describes the overlap function between an N-electron initial state with an (N-1)-electron ionized state. Here, Dyson orbitals are replaced by ionized molecular orbitals, which are calculated based on Hartree-Fock theory (for details on the calculation see supplement of [30]). The resulting calculated PMMs in Fig. 4.3 F-I reproduce the corresponding features in the experimental PMMs in A-D and also explain the spectral weight assymmetry introduced by the angle of light incidence and light polarization. Note, that the calculation model also considers the molecular tilt angle towards the detector plane as denoted in the top right corners of images F-I. Thereby, the differences in the PMMs of $HOMO_{1st}$ and $HOMO_{2nd}$ at, e.g., $k_y = 0.0\,\text{Å}^{-1}$, which arise due to changing tilt angles for molecules in the first and second layer, are reproduced.

Aside from the molecular features, the experimental PMMs exhibit an increased inten-

sity close to the Γ-point, which is not reproduced by the calculations on isolated pentacene. We attribute this intensity to hybridzation between molecular frontier orbitals of molecules in the first pentacene layer with *sp*-bands of the Ag(110) substrate. The *sp*-bands of the statically probed, clean Ag(110) crystal are shown in Fig. 4.3 E for reference. This interpretation is derived from calculations on a pentacene molecule adsorbed atop a cluster of Ag atoms representing the (110) surface. Thereby, the molecule is placed at an adsorption height of 2.2 Å above the substrate (explanation in chapter 4.1.1) and it is oriented as shown in Fig. 4.2 A. The in-plane size of the Ag cluster is chosen such that it represents the unit cell size of the system, while its out-of-plane size considers the information depth of the tr-PES experiment. Increasing the cluster size by a computationally achievable amount in any direction (here, almost doubling the amount of Ag atoms), did not noticeably change the interpretation of the results, thus the chosen cluster size was considered as adequate.

Three different types of Hartree-Fock orbitals are obtained for this model: ones with purely substrate character and hybridized ones with predominant contribution from either the molecule or the substrate. Those hybridized orbitals with mainly molecular contribution attributed to the LUMO, HOMO and HOMO-1 are shown in Fig. 4.4 A, B and C, respectively. As a consequence of this hybridization, the electron transfer from the substrate into the former LUMO, which is observed in the experiment, is also confirmed by the calculation. The strong molecule-substrate interaction is also represented by relative binding energy shifts of the Hartree-Fock orbitals of adsorbed pentacene (Fig. 4.3 N) in comparison to isolated pentacene (Fig. 4.3 J). In the corresponding calculated PMMs shown in Fig. 4.3 K-M, all orbitals within an energy window of 500 meV around the mainly molecule-type orbitals are included, which contribute to additional features in the PMMs and reproduce the intensity at the Γ-point for the HOMO. The intensity at the Γ-point could not be reproduced for all PMMs, likely because silver atoms from deeper-lying cluster layers would enhance the substrate derived intensities, which are not included into the applied model.

In consequence of exciting the interface with a comparably large pump pulse energy of ~ 1 mJ per pulse, a non-negligible amount of space charge was present in the spectrometer. The presence of space charge is observed as a slight broadening of the molecular features (see Fig. 4.2 B) in energy and as a heightened background intensity in the measured spectra with a decreasing slope for larger τ_{delay}. Fortunately, the latter could be corrected for by subtracting a linear slope from the τ_{delay}-dependent, momentum-integrated spectra. Additionally, the pumped EDCs in Fig. 4.2 B needed to be linearly shifted by ~ 150 meV towards higher binding energies in order to adjust the energetic positions of orbital features between the pumped and unpumped spectra.

In retrospect, the choice of the pump pulse energy in combination with the pentacene bilayer/Ag(110) interface was not ideal and caused several difficulties for the experiment

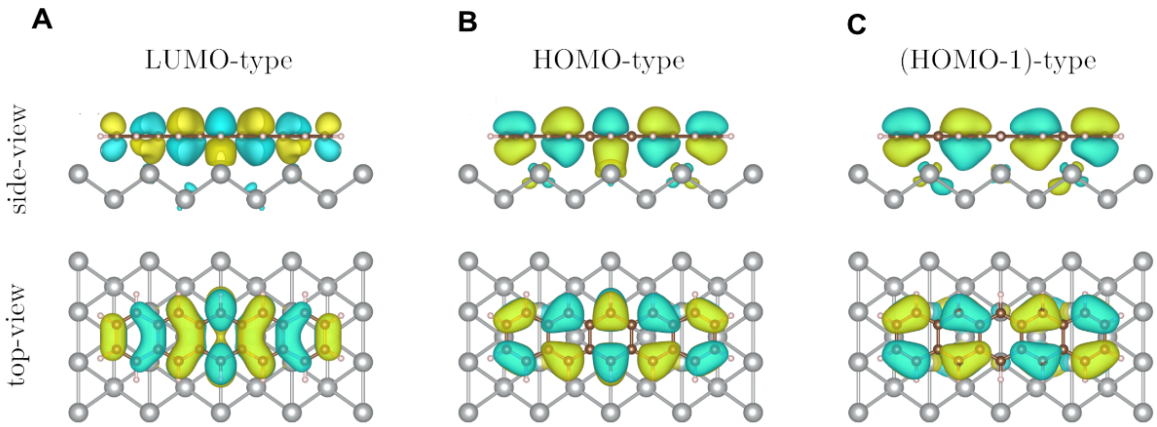

Figure 4.4: Calculated orbitals at the pentacene/Ag(110) interface. Hartree-Fock orbitals calculated for a flat-lying pentacene molecule atop a cluster of silver atoms. Orbital with predominant contribution from **A** the pentacene LUMO, **B** HOMO and **C** HOMO-1.

and its evaluation. Firstly, the abundance of metallic states accessible by the pump laser in comparison to molecule-derived states created a large amount of low energy photoelectrons that contributed to space charge in the spectrometer and dominated over the electrons of interest. Secondly, as explained in chapter 2.3., depending on their energetic distance to E_F, hot carrier life times decrease with the amount of states available for scattering around E_F. For samples of crystalline silver, hot carrier life times below 30 fs are expected from theory [174] and values below 100 fs have been experimentally determined at room temperature [100, 105, 106]. Since the temporal resolution in this experiment was (215 ± 10) fs – at least twice as long as the dynamics of interest – the creation of hot carriers at time zero was obscured, which rendered the search for temporal overlap challenging. The pump pulse fluences were kept high during the beamtime, hoping to find excitation induced band structure changes which would mark time zero. But still, at first glance, no population of states above E_F or other indicators of time zero were observed for pentacene/Ag(110) during the beamtime. At second glance, features marking time zero could be found during data post-processing and time zero was independently confirmed on a reference sample.

Transient Behavior of Molecular Features in the First and Second Pentacene Layer atop Ag(110)

Although, no dynamics above E_F could be traced by means of the chosen experimental settings, transient changes within molecular orbital derived features below E_F are observed and presented in Fig. 4.5 for the $LUMO_{1st}$ (A-D), $HOMO_{1st}$ (E-H) and $HOMO_{2nd}$ (I-L). The shown momentum maps are integrated over 350 fs around the central τ_{delay} denoted in each image's top right corner and they are treated with a Gaussian filter with a full width at

half maximum (FWHM) kernel of 0.16 Å^{-1} for better visualization.

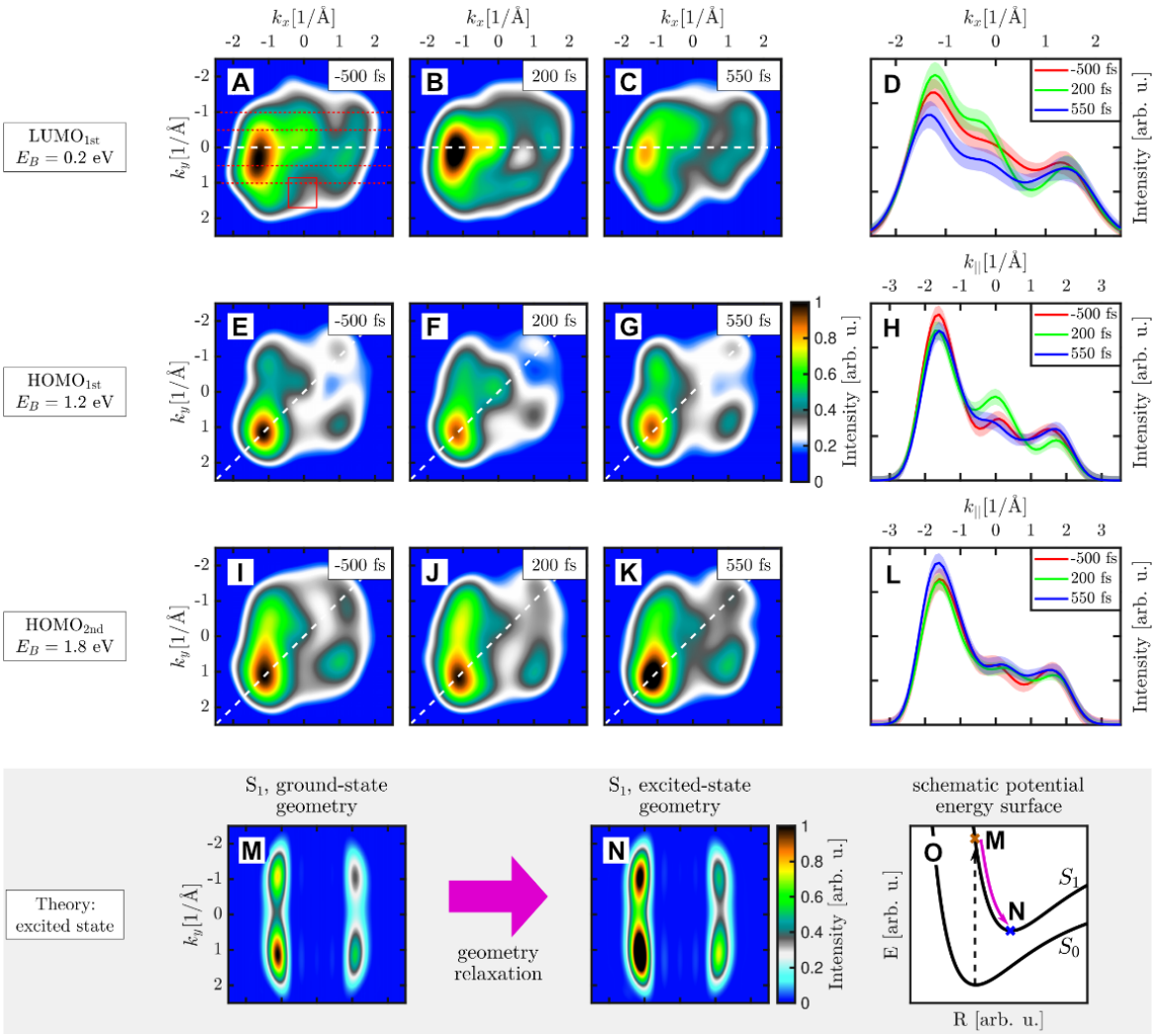

Figure 4.5: Time-resolved orbital momentum maps. Transient momentum maps (integrated over 350 fs around the denoted delay time) of **A**-**C** the LUMO$_{1st}$, **E**-**G** the HOMO$_{1st}$ and **I**-**K** the HOMO$_{2nd}$. Linecuts along the dashed, white lines in the corresponding PMMs are shown in **D** for the LUMO$_{1st}$, in **H** for the HOMO$_{1st}$ and in **L** for the HOMO$_{2nd}$. Experimental error bars to the linecuts are presented as colored, shaded areas. Calculated momentum maps of isolated, excited pentacene in its (**M**) ground state geometry and (**N**) excited state geometry. **O** Schematic depiction of the proposed dynamics within the HOMO$_{2nd}$.

Dynamics in the First Pentacene Layer

Upon excitation, subtle changes are visible in the PMMs for the LUMO$_{1st}$ and HOMO$_{1st}$, which mainly comprise relative intensity variations between the molecular features at $k_x \approx \pm 1.2$ Å^{-1} and the intensity at the Γ-point. Linecuts shown in Fig. 4.5 D and H, which

are taken along the dashed, white lines in the corresponding momentum maps, most prominently reveal an increase in intensity at the Γ-point for both orbitals at $\tau_{delay} = 200$ fs. Simultaneously, the intensity of the molecular features drops for the $HOMO_{1st}$ while it increases for the partially filled $LUMO_{1st}$.

In order to gauge whether these intensity variations are significant or not, an experimental error is estimated, which considers two aspects. Firstly, the background intensity is assumed to be constant for different τ_{delay}. Thus, intensity variations thereof would count towards the experimental error. The background intensity is evaluated within the region marked by a red rectangle in Fig. 4.5 A, since a negligibly small amount of intensity stemming from molecular orbital-derived states is expected therein for all three orbitals (see Fig. 4.3). Secondly, PMMs of the same orbital measured at two different negative τ_{delay} should be identical. Thus, deviations within five different linecuts through molecular features were analyzed, comparing PMMs at τ_{delay} = -500 fs and τ_{delay} = -150 fs. The set of evaluated linecuts is exemplarily marked by red, dashed lines in A for the $LUMO_{1st}$. For the $HOMO_{1st}$ and $HOMO_{2nd}$ sets of linecuts parallel to the dashed lines in the corresponding images are analyzed. The total experimental error is determined by the mean of both error sources and visualized in Fig. 4.5 D, H and L by shaded areas, which are colored like the corresponding linecut. A consideration of these error intervals renders the τ_{delay}-dependent intensity variations observed for the $LUMO_{1st}$ and $HOMO_{1st}$ as significant.

The decrease in intensity for the $HOMO_{1st}$ and simultaneous increase for the $LUMO_{1st}$ is interpreted as an interfacial charge transfer between pentacene and Ag(110), which is enabled by the strong electronic coupling between the molecular π-orbitals and the silver *sp*-band present in the flat-lying molecular adsorption geometry. Thereby, negative charge is fractionally transfered from the $HOMO_{1st}$ into the substrate and redistributed into the partially filled $LUMO_{1st}$.

A previous study [175] on the strongly interacting hybrid interface between the organic component P3HT and gold discussed two possible electron transfer pathways across the hybridized interface: hot charge carriers generated within the substrate can scatter across the interface and transiently alter the charge density within the adsorbed organic material on a time-scale below 500 fs. Further, the delocalization of organic-derived states at the interface facilitates direct electronic transitions to and from the substrate (see Fig. 2.2 A), which leads to a charge separation across the interface creating an interfacial dipole. For P3HT/gold, the localization of charge carriers in the molecules leads to a relaxation time on the nanosecond time scale, which is significantly increased as compared to hot carrier relaxation at metal interfaces, which occurs on the femtosecond time scale (see chapter 2.3). Here, we cannot state the exact mechanism of charge transfer across the pentacene/Ag(110) interface due to the experimental limitations discussed above. Furthermore, there are no

time-resolved theories available currently, by which photoexcitation in extended systems may be treated on a femtosecond to picosecond time scale.

However, the following dynamics observed in the PMMs of $LUMO_{1st}$ and $HOMO_{1st}$ around the Γ-point may be addressed by comparison to static calculations on the pentacene/silver cluster: prominent transient changes occur not only in the molecular features at $k_x \approx \pm 1.2$ Å^{-1}, but simultaneously around the Γ-point, which is associated with the intensity present due to molecule-substrate hybridization (see Fig. 4.5 D and H). An increase in intensity at the Γ-point is observed for both the $LUMO_{1st}$ and $HOMO_{1st}$ at $\tau_{delay} = 200$ fs, while the relative intensity decreases at $\tau_{delay} = 550$ fs for the $LUMO_{1st}$. By comparison to static calculations on the neutral pentacene molecule atop a silver cluster with varied adsorption heights, we derive that the intensity variation at the Γ-point is likely due to a changing adsorption height between molecule and substrate during charge transfer across the interface (for details on the calculation see supplement of [30]). The time scale of the observed dynamics is about two orders of magnitude slower than for electronic processes on the excited, clean silver substrate, and agrees with the time scales of atomic motion in a molecule (see chapter 2.3).

Dynamics in the Second Pentacene Layer

In contrast to the observations in the transient PMMs of molecules in direct contact to the substrate, little to no intensity variations are observed around the Γ-point for the $HOMO_{2nd}$ (see Fig. 4.5 L). This observation agrees well with the decreased interaction strength between the substrate and molecules in the second pentacene layer. Consequently, we argue that molecules in the second layer are indeed electronically largely decoupled from the substrate and can be theoretically treated as isolated molecules.

In order to support this hypothesis, calculations on isolated pentacene in its ground- and excited state are compared to the molecular orbital derived features at $k_x \approx \pm 1.2$ Å^{-1} in the transient PMMs of $HOMO_{2nd}$ (Fig. 4.5 I-K). Before excitation, the PMM of $HOMO_{2nd}$ (see Fig. 4.5 I) corresponds to the calculation on pentacene in its ground state shown in Fig. 4.3 H. With the pump pulse energy of 3.1 eV, the molecule can be vertically excited from its ground state (S_0) to its first excited singlet state (S_1) [176]. In Fig. 4.5 O, the potential energy surfaces of S_0 and S_1 are sketched and the pump pulse excitation is depicted by a vertical, dashed arrow connecting the S_0 potential minimum with the S_1 potential curve. At this point – immediately after excitation – the molecule is still in its ground state geometry as argued within the Born-Oppenheimer approximation (see chapter 2.3). The resulting PMM is shown in Fig. 4.5 M. After a geometry relaxation, the excited molecule takes its relaxed excited state geometry in the potential minimum of S_1. The corresponding PMM is

shown in Fig. 4.5 N.

In literature, singlet life times of ~ 500 fs have been reported for pentacene dimers [177] and of ~ 330 fs for a pentacene bilayer atop C_{60}/Ag(111) [178]. Because the temporal resolution of the PMMs in Fig. 4.5 is 350 fs and thus both the PMMs in J and K agree with the reported singlet life times, we compare the PMMs in J and K to the calculated singlet states of excited pentacene. Thereby, we associate the experimental $HOMO_{2nd}$ at 200 fs (J) with the calculated singlet in its ground state geometry (M) and the experimental PMM at 550 fs (K) with the calculated singlet in its excited state geometry (N). A comparison between the calculated PMMs in M and N reveals an intensity increase of the molecular features as a result of geometry relaxation (see also supplement of [30]). The same is observed in the corresponding experimental data (see, e.g., bottom left quadrant of J and K as well as linecuts in L), although the intensity increase is less pronounced in the experiment. The contribution of both neutral and excited molecules to the experimental PMMs may explain this deviation.

From the overall agreement between the observed dynamics in the second pentacene layer with calculations on isolated pentacene, we conclude two points: firstly, the theoretical description by isolated pentacene is appropriate for molecules in the second layer. Secondly, the dynamics observed for the $HOMO_{2nd}$ resemble excited-state molecular dynamics and may be explained by a geometric relaxation of the molecule.

4.1.3 Summary

Our experiment on a pentacene bilayer on Ag(110) was the first to study hybrid organic/inorganic interfaces at a FEL source. We could successfully explore and optimize the experimental parameters to transiently record momentum maps in the valence region on a subpicosecond time scale. We could image and identify pump-probe excited molecular frontier orbitals separately for molecules in the first and second adsorbate layer. Imaging time-resolved molecular frontier orbitals lies at the forefront of current research as such an orbital has only recently been published in Science [22].

By comparison to calculations, we identify a feature at the Γ-point as the result of hybridization between the substrate and molecules in the first layer. Molecules in the second layer are appropriately modeled by isolated molecules. We find that changes in the momentum maps of molecular orbital-derived states are traceable within several hundreds of femtoseconds after optical excitation. In contrast, excitation-induced changes occur within less than 100 fs in pristine silver samples.

The transient changes in the molecule-derived orbitals can be attributed to electronic and structural changes at the interface. Molecules in the first layer are involved in interfacial

charge transfer with the substrate and simultaneously change their adsorption height within less than 550 fs. Molecules in the second layer are electronically decoupled from the substrate. Their excited state resembles the excited singlet states of isolated pentacene and undergoes a geometric relaxation within ~ 550 fs.

We further conclude that singlet fission has not occured within the time frame of this experiment. However, due to the insufficient statistics aquired during the measurement as well as due to the space-charge induced implications on the energy and momentum resolution and on the τ_{delay}-dependent binding energy shifts, we could not trace all excitation pathways as, e.g., the final state of the electron excited from the $\mathrm{HOMO}_{\mathrm{2nd}}$ could not be resolved. Furthermore, calculating the exact relaxation pathways in large molecules, such as pentacene, on time scales as long as several hundreds of femtoseconds is currently computationally not feasible. A theoretical approach to accurately describe PMMs during charge transfer dynamics needs yet to be developed. Nevertheless, our findings on combined electronic and structural dynamics during charge transfer across a hybrid organic/inorganic interface may set a step towards understanding and controlling photo-induced reactions, catalysis and organics based devices. Also, establishing the second molecular layer in a bilayer pentacene/Ag(110) sample as 'isolated' allows for studying fundamental scientific questions and for shooting 'molecular movies' [179].

4.2 Copper(II)phthalocyanine atop $TiSe_2$

The results shown in this chapter have been submitted for publication. They are a combined experimental and theoretical study in collaboration with M. Nozaki, M. Reuner, N. Wind, C. Metzger, M. Haniuda, M. Heber, D. Kutnyakhov, F. Pressacco, L. Wenthaus, C.-H. Min, F. Roth, S. Mahatha, A. Madsen, T. Wehling, K. Niki, D. Popova-Gorelova, K. Rossnagel, M. Scholz and F. Reinert.

4.2.1 Materials Overview

The adsorbate CuPc is a representative of the molecular class of $3d$-transition metal complexes with nearly planar shape and consists of a positively charged Cu^{2+} atom surrounded by a doubly negatively charged phthalocyanine ligand (see Fig. 4.6 A). The phthalocyanine ligand is made up of two subunits. Firstly, a central azaporphyrin ring consisting of four pyrrole subunits and secondly four benzene rings annulated at 3,4-position of the respective pyrrole units. The sp^2-hybridized carbon atoms and the embedded nitrogen atoms form a planar, delocalized π-electron system with four-fold in-plane symmetry. In the following, a distinction will be made between carbon atoms located within the azaporphyrin ring (circled in blue in the top right of Fig. 4.6 A), which are bound to nitrogen and are thus labeled as "CN", and between carbon atoms in the four benzene rings (circled in purple), which are labeled as "CC". In this work, the bridging carbon atoms between the two subunits will be considered to belong to the outer benzene units.

The substrate $1T$-$TiSe_2$ (see Fig. 4.6 B) is part of the transition metal dichalcogenide (TMDC) family – van-der-Waals layered compounds exhibiting various dimensionality-driven phenomena such as charge density waves and superconductivity [180–182]. $TiSe_2$ is of particular interest, as it is potentially one of two currently known excitonic insulators [183] with a relatively high transition temperature of 200 K [104]. Furthermore, it is – similar to other TMDC compounds – sought after for application in optoelectronics and nanoelectronics due to its high charge carrier injection efficiency across hybrid interfaces [184, 185]. This property is attributed to the quasi-2D nature of the topmost van-der-Waals sheet, where charge carriers are mainly generated, e.g., by photoexcitation. Limited by the weak coupling strength between the van-der-Waals bound sheets, these charge carriers are confined to the topmost sheet for a longer period of time as compared to in a 3D crystal, thus resulting in a higher injection probability into adsorbates. The layered structure of $TiSe_2$ also benefits the preparation of clean sample surfaces by exfoliation during experiments. Each sheet consists of Ti atoms (grey spheres in Fig. 4.6 B), which are sandwiched between two Se atom layers (orange spheres) with triangular structure, resulting in a three-fold sym-

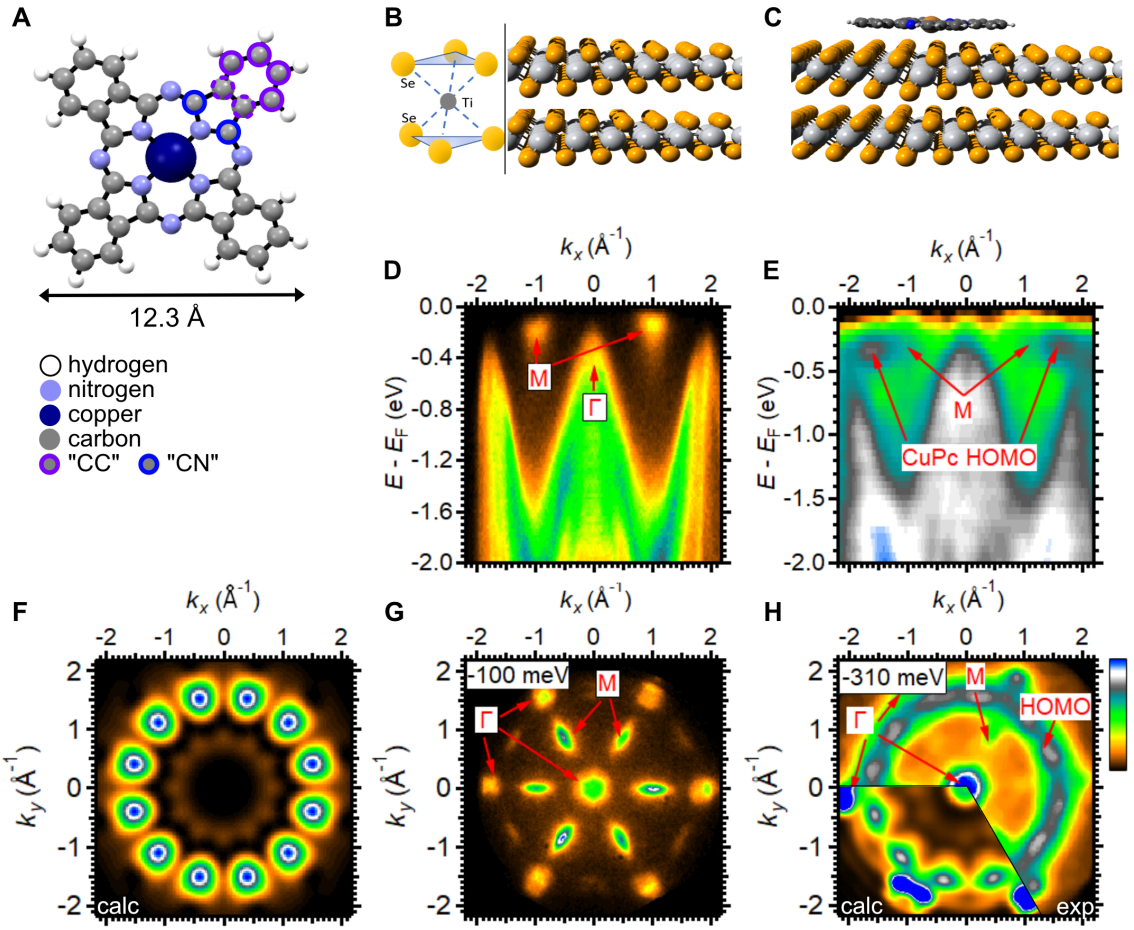

Figure 4.6: Materials overview. Schematic representation of **A** the molecular structure of CuPc, **B** two van-der-Waals bound $TiSe_2$ sheets (right) with triangular crystal structure (left) per layer and **C** of a CuPc molecule adsorbed atop $TiSe_2$. Energy dispersions along the Γ-M-Γ-M-Γ direction for **D** clean $TiSe_2$ and **E** a monolayer of CuPc atop $TiSe_2$, which are probed by 42.0 eV and 36.3 eV, respectively. **F** Calculated momentum map of the HOMO for isolated CuPc in three domains, relatively rotated by 120°. The calculation was provided by C. Metzger and is based on a plane wave final-state approximation with independent atomic centers as initial states. **G** Momentum map of clean $TiSe_2$ probed by 42.0 eV, integrated around -(100 ± 220) meV and three-fold symmetrized. **H** Momentum map of a monolayer CuPc atop $TiSe_2$ probed by 36.3 eV, integrated around -(310 ± 220) meV, three-fold symmetrized and treated with a Gaussian filter. In the bottom third a calculated momentum map is overlaid.

metric surface geometry.

At room temperature, $TiSe_2$ is a small-gapped semiconductor with an energy gap of (74 ± 15) meV [186]. Its dispersion along the Γ-M-Γ-M-Γ direction measured at a probe pulse energy of 42.0 eV at the HHG-source is shown in Fig. 4.6 D. Se 4*p*-derived states appear as downward facing parabolas at the Γ-points, while the electron pockets at the M-points are derived from Ti 3*d* states. In Fig. 4.6 G, the Fermi surface of clean $TiSe_2$ is

shown, also measured at the HHG-source with a probe energy of 42 eV. The momentum map is integrated over $\pm$ 220 meV around the denoted center energy and three-fold symmetrized according to the substrate symmetry. The Γ- and M-points stemming from the bottom Se layer are rotated by 60° relative to the high symmetry points of the top Se layer and appear slightly fainter. Due to its low density of states near E_F and its small band gap, $TiSe_2$ is sensitive towards photoexcitation induced spectral weight redistributions across E_F and into energetically available adsorbate states. Therefore, $TiSe_2$ promised to be a suitable substrate for visualizing the dynamic electronic and structural interplay at the CuPc/$TiSe_2$ interface.

Sample Growth

CuPc (gradient sublimated) was deposited atop a cleaved, room-temperatured $TiSe_2$ surface of $\sim$ 5x5 mm size at a Knudsen cell temperature of 400 K, a deposition rate of 1 monolayer per 40 min and an evaporator-to-sample distance of 15 cm. The molecules adsorb in a flat-lying manner atop $TiSe_2$ (see Fig. 4.6 C) forming a physisorptive interface – no charge redistribution between substrate and molecule is observed for the system in its ground state.

Electronic Sample Characterization

In Fig. 4.6 E, the experimentally obtained energy dispersion of the CuPc/$TiSe_2$ interface is shown along the Γ-M-Γ-M-Γ direction, measured at a probe pulse energy of 36.3 eV. The CuPc HOMO is observed as a dispersion-free state of 400 meV width with its energetic center located at -310 meV below E_F. No hybridization between molecular and substrate states is observed, as expected for weakly interacting interfaces.

The corresponding momentum map at the HOMO energy is shown in Fig. 4.6 H, and is integrated around -(310 $\pm$ 220) meV, three-fold symmetrized and treated with a Gaussian filter. It can be understood as a superposition of the HOMO momentum distribution of isolated CuPc molecules, which are arranged in (at least) three domains according to the substrate high-symmetry directions (see Fig. 4.6 F), with the momentum distribution of clean $TiSe_2$ (G). Twelve prominent intensity features stemming from the CuPc HOMO are radially surrounding the Γ-point at a lateral distance of $k_{||} = 1.67 Å^{-1}$ with an azimuthal separation of 30°. These twelve features have a lateral width of $(0.50 \pm 0.01)\ Å^{-1}$ and thus slightly overlap with the substrate's Γ- and M-points.

For comparison, the experimentally obtained PMM in Fig. 4.6 H is overlaid with a calculated momentum map at the HOMO energy for a CuPc molecule adsorbed on a $TiSe_2$ cluster of 8x8x8 unit cells size in the bottom third (in the calculation the molecule is oriented relative to the substrate as shown in Fig. 4.7 C). This calculation was performed by

Prof. Niki Kaori, Misa Nozaki and Masato Haniuda from the University of Chiba, Japan, and is based on DFT calculated initial states using the 'Vienna Ab Initio Software Package' (VASP) and plane-wave final states as input for simulating PMMs with 'kMap-py' and 'MOPDOS@VASP'. In their band structure calculations, more non-dispersive molecular orbitals appear below -1.5 eV, which are also experimentally observed but will not be analyzed further in this thesis. As a result from their geometric relaxation and optimization procedure, an adsorption height of 3.16 Å is found for CuPc atop $TiSe_2$.

Structural Sample Characterization

In physisorptive systems, van-der-Waals forces and the push-back effect govern the interaction and molecules appear to "float" atop the substrate at submonolayer coverages (see chapter 2.1). Upon increasing coverage, neighboring molecules sterically hinder the free movement and rotation of the molecules. Here, a fixed adsorbate structure was only found for coverages above ~ 0.8 monolayers. The LEED image of a closed monolayer of CuPc atop $TiSe_2$ taken at 24 eV is shown in Fig. 4.7 A. Reflexes originating from substrate and molecular Bragg peaks are marked by blue and red circles, respectively, and unit cell vectors are colored equally. While the substrate has p3m1 symmetry with an angle of 60° between substrate unit cell vectors $\mathbf{s}_1$ and $\mathbf{s}_2$, a nearly quadratic unit cell with an area of (13.8 x 13.8) Å and an angle of 93.7° between unit cell vectors $\mathbf{a}_1$ and $\mathbf{a}_2$ is found for the molecular overlayer. The corresponding adsorbate superstructure $(0, 4\,/\,4.5, 2)$ is noncommensurate but results in a point-on-line arrangement of molecules atop the substrate [187]. Such an arrangement is marked by the direction of one adsorbate unit cell vector coinciding with a substrate unit cell vector. Thereby, molecules have no fixed adsorption sites as in a commensurate superstructure, but rather arrange freely along the high-symmetry direction of the substrate. According to the found superstructure matrix, at least two different adsorption sites along the substrate directions must exist for the densely packed monolayer. Previous studies on phthalocyanines grown atop weakly interacting (111) metal crystal surfaces have also observed point-on-line arrangements [67, 188–191].

From the performed LEED measurement alone, the in-plane orientation of molecules relative to the underlying substrate is not deducible. However, in combination with the HOMO momentum distribution (Fig. 4.2.1 H), the amount of possible molecular orientations can be limited: we find that the twelve-fold symmetry of the HOMO momentum distribution is only explained by the superposition of at least three molecular orientations rotated by 120° each. These orientations correspond to molecules arranged in the three rotational domains according to the substrate symmetry as sketched in Fig. 4.7 B. The LEED pattern confirms that three additional mirror domains exist, thus resulting in at least six total domains which

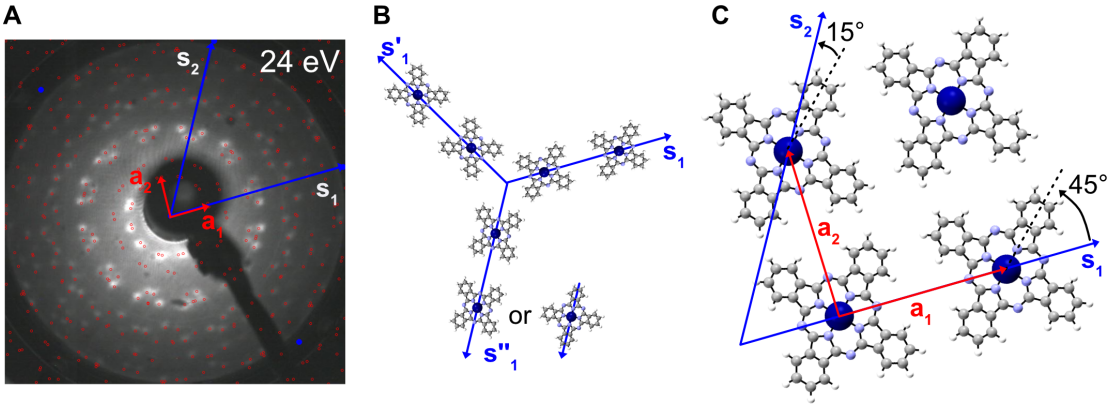

Figure 4.7: Structural characterization of CuPc/$TiSe_2$. A LEED image of a monolayer CuPc atop $TiSe_2$ taken at 24 eV. Unit cell vectors of the molecule and the substrate are marked by red and blue arrows, respectively. **B** Schematic representation of molecules adsorbing along the substrate's high-symmetry directions as in point-on-line growth. **C** Molecular arrangement within one growth domain.

add to the HOMO momentum distribution. In order to obtain twelve-fold symmetry in the HOMO momentum distribution, the orientation of molecules in the domains must be the same as in the mirror domains. This condition is only met if two opposite benzene rings ('wings') of CuPc align either on top of or at an angle of 45° to the substrate unit cell vector $\mathbf{s}_1$ (see B). Although, by regarding the relative positioning of substrate features and HOMO features in Fig. 4.2.1 H an alignment of the CuPc wings with $\mathbf{s}_1$ is excluded [192] and the configuration shown in Fig. 4.7 C is deduced to exist here.

Note, that during the beamtimes of the time-resolved measurements no LEED image of the grown interface could be taken to confirm the structure shown in Fig. 4.7 A. Nevertheless, the intensity of the molecular features suggest a coverage between 0.8 and 1.0 monolayers and the HOMO momentum distribution and the C 1*s* XPD patterns prove the existence of highly ordered CuPc growth atop $TiSe_2$.

4.2.2 Time-resolved Characterization

The time-resolved characterization of the CuPc/$TiSe_2$ interface is motivated by observing the photoinduced electronic interplay between substrate and adsorbate on a sub-picosecond time scale, while simultaneously visualizing the structural response of the molecules. To do so, we combined three modalities of tr-PES – tr-ARPES in the UV-range, tr-XPS and tr-XPD in the soft x-ray-range – which we performed in the same experimental setup (see chapter 3.2.3.1). While tr-ARPES allows for studying electronic dynamics in the valence region, element specificity and quantitative statements can be extracted from tr-XPS measurements at core-levels. Structural dynamics with sub-Ångstrom precision are accessed by tr-XPD. Presented in the following, our findings are ordered by their electronic or structural origin.

Tr-ARPES experiments in the valence region were performed at both the HHG source and at the FEL source *FLASH* with pump pulse excitation energies of 1.6 eV (*p*-polarized) and probe pulse energies of 36.3 eV (*p*-polarized). In both measurements, data-sets sampling over ~ 2 ps were aquired within ~ 15 h, but due to the higher sampling frequency at the HHG source and due to its better temporal resolution of (95 ± 5) fs only valence band data taken at the HHG source will be presented here. The tr-XPD experiments were performed at *FLASH* with a pump pulse energy of 1.6 eV and a probe pulse energy of 370 eV (both *p*-polarized). The temporal resolution of the core-level measurements is evaluated to be (180 ± 10) fs. All presented measurements were taken on the same sample substrate with pump- and probe pulses impinging along the substrate's Γ-M direction. In chapter 3.2.3 further details on the experimental setup and the time-of-flight momentum microscope are discussed. The raw-data output of the time-of-flight momentum microscope provides $\mathbf{k}_{||}$ values in units of pixels and time-of-flight arrival times of electrons at the detector plate need to be translated into binding energies. For this energy- and momentum calibration, characteristic features – here, the HOMO energy and Γ- to M-point distance – were compared to reference values, which were previously determined at a He-I source with a hemispherical analyzer (Scienta Omicron R3000). All shown momentum maps are integrated over ± 220 meV around their denoted center energy and are three-fold symmetrized according to the substrate symmetry. If not stated otherwise, no further data treatment was performed.

4.2.2.1 Electronic Dynamics

A sketch of the experiment is shown in Fig. 4.8 A. For both the valence band and core-level regions four-dimensional data sets of energy-momentum space and time are obtained. Different projections along two of these parameters are imaged in Fig. 4.8 B and C for the data taken in the valence band region. B depicts the time-dependent occupation of electronic states for energies accessible by the pump pulse. In C, momentum (top three rows) and energy-momentum maps (bottom row) are extracted for four selected pump-probe delay times $t_{-1} = -700\,\mathrm{fs}$, $t_0 = 0\,\mathrm{fs}$, $t_1 = 375\,\mathrm{fs}$ and $t_2 = 1800\,\mathrm{fs}$, which are marked in B. The time frames are integrated within a window of $\pm\,100\,\mathrm{fs}$ around the denoted pump-probe delay time.

At t_{-1}, the CuPc HOMO is found as the intensity modulated ring-shaped feature shown in the third row of Fig. 4.8 C next to the substrate-derived features at the Γ- and M-points. Its shape and the calculated momentum distribution, which is overlaid in the bottom part, have been discussed in the previous chapter. Prior to pumping, no intensity is detected above E_F.

Clearly marking t_0, excitation with the pump pulse results in a spectral weight redistribution from the Se $4p$ valence band into the Ti $3d$ conduction band [28]. The depletion of the Se $4p$ band can be traced in the bottom row of Fig. 4.8 C, and the occupation of the three-fold symmetric cigarette-like features characteristic for the Ti $3d$ band is seen in the second row of C.

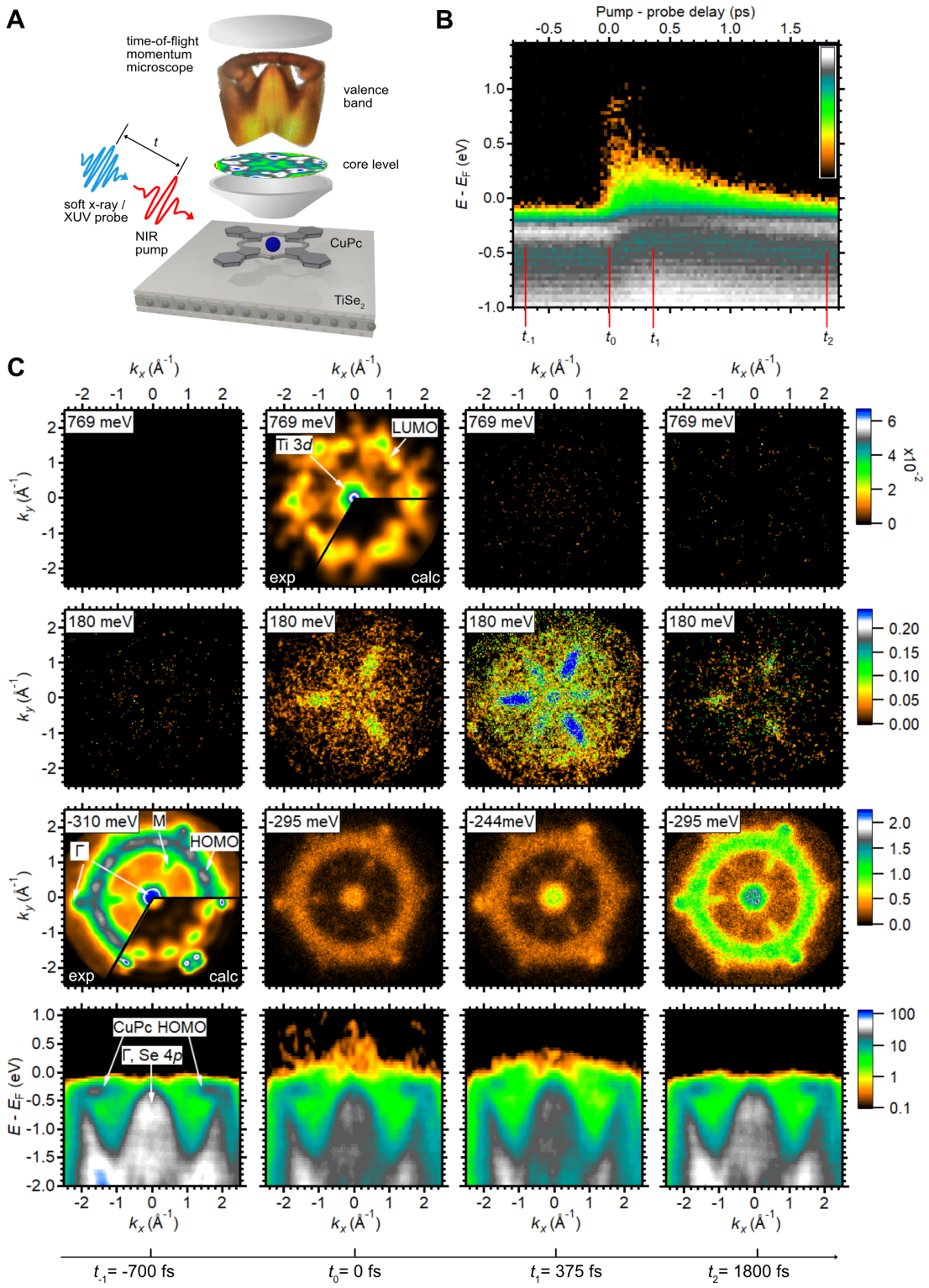

Figure 4.8: Electronic valence band dynamics of CuPc/$TiSe_2$. **A** Schematic drawing of the experiment. **B** Valence band dynamics of CuPc/$TiSe_2$ excited by a 1.6 eV pump pulse energy. **C** Transient momentum maps integrated around the LUMO energy (top row), Ti 3*d* states (second row) and HOMO energy (third row) for four selected pump - probe delay times. The integration window of the HOMO momentum map is adjusted according to its shifting binding energy. Transient energy-momentum maps are shown in the bottom row.

LUMO Occupation

Simultaneously, we observe the occupation of a state at t_0 that is energetically located between 550 and 990 meV. It decays with a time constant of $\tau_{\mathrm{LUMO,decrease}} = (92 \pm 50)$ fs. In its corresponding momentum map, which is shown in the top row of Fig. 4.8 C (treated with a Gaussian filter), a ring-shaped feature with a radius of $(1.60 \pm 0.05)\,\text{Å}^{-1}$ is seen as well as some intensity at the Γ-point, which stems from Ti 3*d* bands. The energetic width of ~ 400 meV and the non-dispersive character suggest that the ring-shaped feature is of molecular origin, e.g., the CuPc LUMO.

Two excitation pathways could lead to its population: firstly, a direct intramolecular excitation from HOMO to LUMO, which would correspond to an optical gap of ~ 1.1 eV. This value would be slightly smaller than the value of (1.4 ± 0.3) eV, which has been reported for CuPc in its thin film phase (~ 1 nm) grown atop a metallic substrate [193], but would still allow a direct excitation via the pump laser due to the energetic width of the molecular orbitals. The second pathway would be an indirect channel, where hot electrons are excited within the substrate and are then scattered from the Ti 3*d* band into the molecular state.

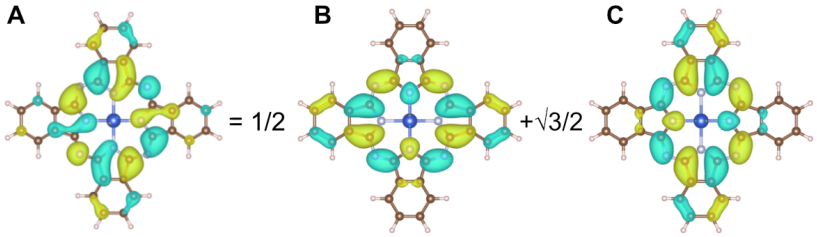

Figure 4.9: Calculated real space LUMO orbitals. A Intermixed excited orbital, which is populated in the experiment via hot electron scattering from the Ti *d* band, and is composed of a linear combination between **B** LUMO and **C** LUMO'.

By comparison of the experimental momentum distribution to excited state calculations on isolated CuPc, which were performed by M. Reuner and D. Popova-Gorelova with the same approach as discussed in chapter 4.1, we identify the origin of the ring-shaped feature to be a substrate induced molecular orbital (Fig. 4.9 A), which is populated via hot-electron transfer from the substrate. The LUMO (B) and LUMO'(C) of CuPc are degenerate in gas-phase and are spread over two opposite benzene rings resulting in a two-fold symmetry each. Assuming either an equal population of LUMO and LUMO' or only population of one orbital in the theoretical model did not reproduce the experimental momentum distribution. Instead, the momentum distribution of a linear combination of both orbitals (1/2 LUMO + $\sqrt{3}$/2 LUMO') could reproduce the observed ring-shaped feature best and is overlaid on the momentum map at t_0 in the top row if Fig. 4.8 C. Such a molecular orbital may emerge due to the interaction between molecule and substrate, which can, e.g., lift the degeneracy

of LUMO and LUMO' and result in new, intermixed excited orbitals that are favored by the substrate symmetry. In the following, the observed intermixed excited orbital will be referred to as 'LUMO' for simplification.

Relaxation Dynamics in $TiSe_2$ and Charge Carrier Transfer into the CuPc HOMO

Immediately after excitation with the pump pulse, hot holes created in the Se p band and hot electrons in the Ti $3d$ band begin to relax by scattering towards E_F. The fraction of hot electrons (< 1 %) scattered into the LUMO quickly decays with a relaxation constant of $\tau_{LUMO,decrease} = (92 \pm 50)$ fs (see brown line in Fig. 4.10 A). Against expectation, the intensity within the Ti $3d$ band (grey line) does not immediately decay but instead increases up until t_1=375 fs with a time constant of $\tau_{Ti3d,increase}$=(243 ± 50) fs. Only after t_1, the population decreases again with $\tau_{Ti3d,decrease}$=(503 ± 250) fs, nearly recovering its initial state at t_2.

For clean $TiSe_2$ in its charge-density phase but under similar excitation conditions, a delayed spectral weight increase above E_F has been observed before, reaching its maximum intensity after 200 fs [104]. This observation has been attributed to the small band gap in $TiSe_2$ and is explained by impact ionization (see chapter 2.3), a mechanism involving electron-scattering between a hot electron in the Ti $3d$ band and a "cold" electron in the Se $4p$ band (or in the previously occupied part of the Ti $3d$ band). Energy- and momentum-transfer between these two electrons results in the creation of two secondary hot electrons within the previously unuccupied part of the Ti $3d$ conduction band.

Here, we find that the impact ionization process is significantly prolonged, which we explain with the presence of the CuPc adsorbate layer. Due to its energetic proximity to E_F, the CuPc HOMO becomes eventually populated by hot holes scattering towards E_F. The black line in Fig. 4.10 A shows the time-dependent HOMO population, which decreases between t_0 and t_1 by up to (30 ± 5) % with $\tau_{HOMO,decrease}$=(222 ± 50) fs an nearly recovers until t_2 with $\tau_{HOMO,increase}$=(769 ± 250) fs – mirroring the dynamics in the Ti $3d$ band. In order to disentangle the intensities stemming from substrate states at the Γ- and M-points from the HOMO intensity, the data was masked in momentum space as pictured in Fig. 4.10 B for the evaluation in A. Due to the complementary population dynamics of the Ti $3d$ band and the HOMO, the involvement of CuPc in the $TiSe_2$ impact ionization process appears obvious.

In Fig. 4.10 D the proposed relaxation mechanism in $TiSe_2$ involving the CuPc HOMO and LUMO is sketched: At t_{-1}, the system is in its ground state. At t_0, hot charge carriers are mainly created in the substrate within the energy region accessible by the pump pulse, hot charge carrier relaxation initiates and shortly populates the LUMO. Subsequently, the

population of Ti 3*d* states increases by impact ionization and hot holes (empty red circles) scatter into the HOMO. In return, electrons (filled red circles) are transferred back into the substrate (see dashed red lines at t_1). These electrons, as well as those decaying from the LUMO, become additionally available for further scattering processes. Ultimately, the frontier orbitals of CuPc function as additional charge carrier reservoirs that increase the amount of impact ionization processes and prolong the $TiSe_2$ relaxation time.

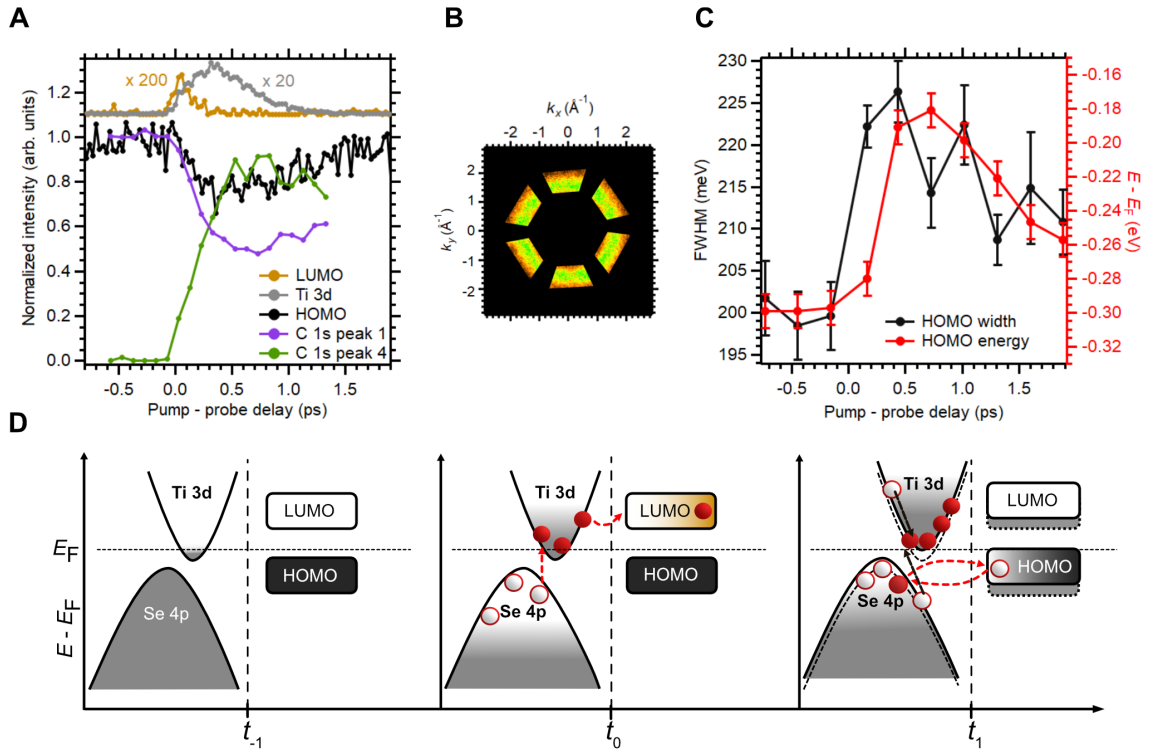

Figure 4.10: Hot carrier relaxation and interfacial charge transfer. A Population dynamics of the LUMO (brown), Ti 3*d* band (grey), HOMO (black), C1s core level of neutral CuPc molecules (purple) and of $CuPc^+$ (green). **B** Masked area integrated for HOMO evaluation in A. **C** Transient energetic width (FWHM, black, left axis) and energetic position (red, right axis) of the HOMO. **D** Schematic drawing of proposed relaxation dynamics in $TiSe_2$ involving the CuPc HOMO and LUMO.

When tracing the HOMO in energy over time, two observations are made: following its population dynamics, the energetic width of the HOMO (black line, Fig. 4.10 C) increases by up to $(12 \pm 2)\,\%$. Simultaneously, the energetic position of the HOMO shifts by up to $(120 \pm 5)\,\mathrm{meV}$ towards E_F. Both effects have been previously observed for molecules involved in charge transfer [47, 194].

Carbon 1*s* Core Level Dynamics

By means of probe pulse energies in the soft x-ray-range and otherwise similar pump pulse excitation parameters to the valence band experiments, the dynamics of the molecular carbon 1*s* (C 1*s*) core level were traced (see Fig. 4.11 A). Marking t_0, side bands (indicated by black arrows) appear towards lower and higher energies of the core level for the duration of temporal overlap between the pump and probe pulse (see 'LAPE effect' in chapter 3.2.3.1). Between t_0 and t_1, a gradual shifting of spectral weight towards lower binding energies as well as the appearance of a new peak is observed. Towards $t_2' = 1.25$ ps, the spectral shape almost recovers again. Due to the likeliness of the C 1*s* spectral evolution to the valence band dynamics (see Fig. 4.8 B), we assume that both dynamics are connected to the charge transfer process between the CuPc HOMO and the substrate (see previous section).

In order to verify this assumption, the C 1*s* spectral shape is analyzed at four selected time points t_{-1}, t_0, t_1 and t_2' (see Fig. 4.11 B). Each C 1*s* spectrum is integrated over $\pm$ 50 fs and is presented in B (grey line+markers) with a vertical offset increasing from t_{-1} to t_2'. For a quantitative analysis, the spectra are fitted by several Gaussian shaped peaks as exemplarily shown for t_{-1} and t_1 (black lines). The spectrum at t_{-1} resembles those for CuPc in its ground state from literature [31, 195, 196] and is composed of two prominent peaks at -284.4 eV and at -285.8 eV and of a tail of smaller peaks towards higher binding energies. The origin of the peak at -284.4 eV is unambiguously attributed to carbon atoms located in the four benzene rings of CuPc ('CC', see purple circled atoms in C, bottom). Due to their differing chemical surrounding, carbon atoms within the azaporphyrin ring ('CN', circled in blue in C) appear shifted towards higher binding energies at -285.8 eV.

Calculations performed by M. Reuner and D. Popova-Gorelova on isolated CuPc, which are shown in the top of Fig. 4.11 B, reproduce this energetic separation between CC and CN peaks. Thereby, vertical lines (purple) depict the energetic positions and relative intensities resulting from the different carbon species. They are broadened in energy by multiplication with a gaussian peak (purple, dashed line) in order to resemble the experiment. The amount of vertical lines underneath the theoretical CC peak suggests, that more than two carbon species should be distinguished, which contribute to the C 1*s* shape. From simply looking at the experimental spectrum at t_{-1} by eye, the presence of an additional peak between the CC and CN peak is obvious under two considerations: firstly, both peaks should have a comparable energetic width and secondly, due to the quantitative potential of tr-XPS, the relative intensity ratio between CC and CN peaks should be 3:1.

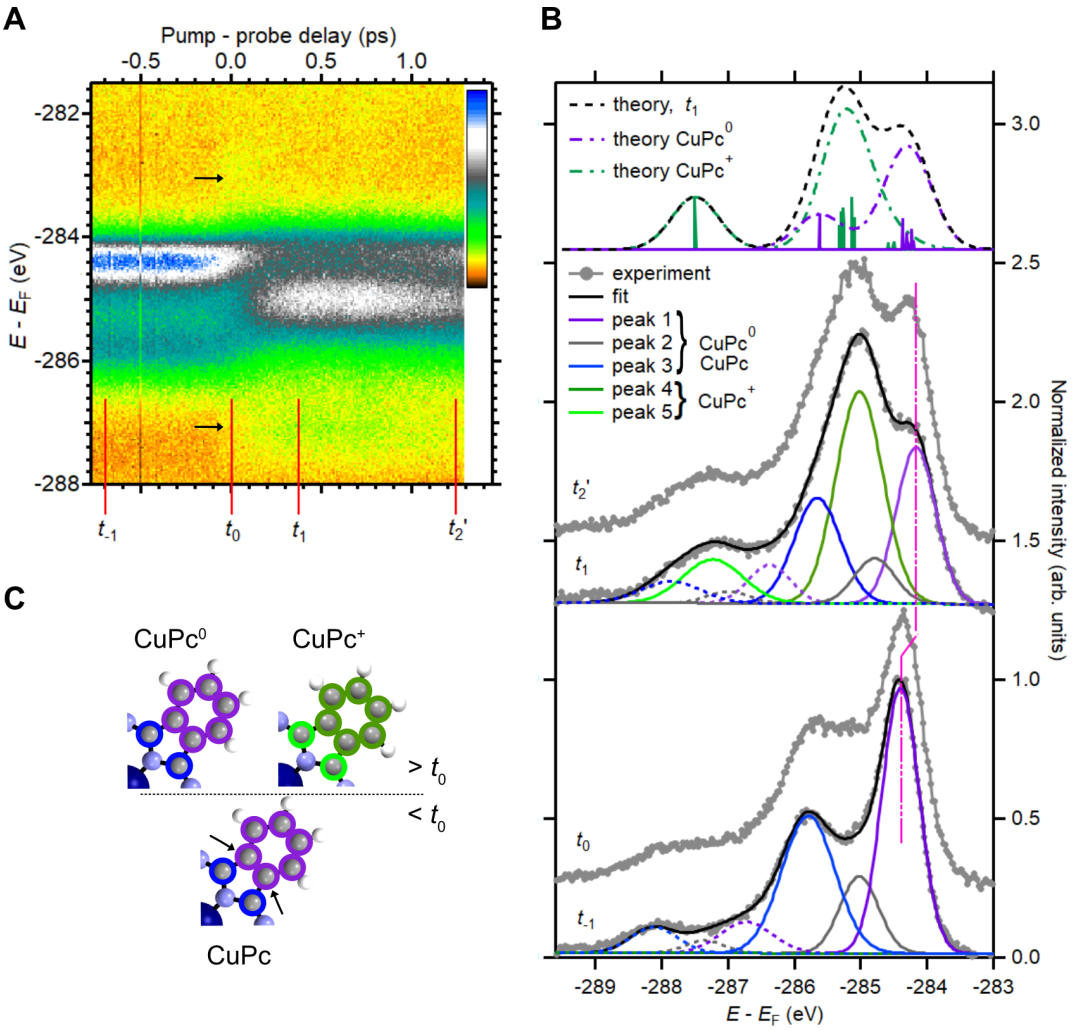

Figure 4.11: C 1*s* core level dynamics at the CuPc/$TiSe_2$ interface. **A** Evolution of the C 1*s* core level. Black arrows indicate side bands due to the LAPE effect at t_0. **B** C 1*s* spectra (grey markers and line) at four selected pump-probe delay times. Fits (black line) including gaussian shaped peaks for carbon atoms in different chemical environments (solid lines, peaks 1-5) and for shake-up satellites (dashed lines) are included to the spectra at t_{-1} and t_1. Calculated line shapes for $CuPc^0$ (purple, dashed line) and $CuPc^+$ (green, dashed line) are shown at the top (calculation by M. Reuner and D. Popova-Gorelova). **C** Section of CuPc structure with carbon atoms colored according to their corresponding peak in B.

In the fitting procedure, these two considerations can only be met, when an additional peak (peak 2) is placed at -285.0 eV in between the CC (peak 1) and the CN peak (peak 3). In few previous studies, this additional peak was addressed [195, 197–199] and attributed to either a shake-up satellite, a vibrational C-H stretch mode or to carbon atoms in the benzene ring, which are not bound to hydrogen (marked by black arrows in C). Within the theoretical model applied here (results shown in top of B), the origin of peak 2 remains unknown and it will not be disclosed in this thesis.

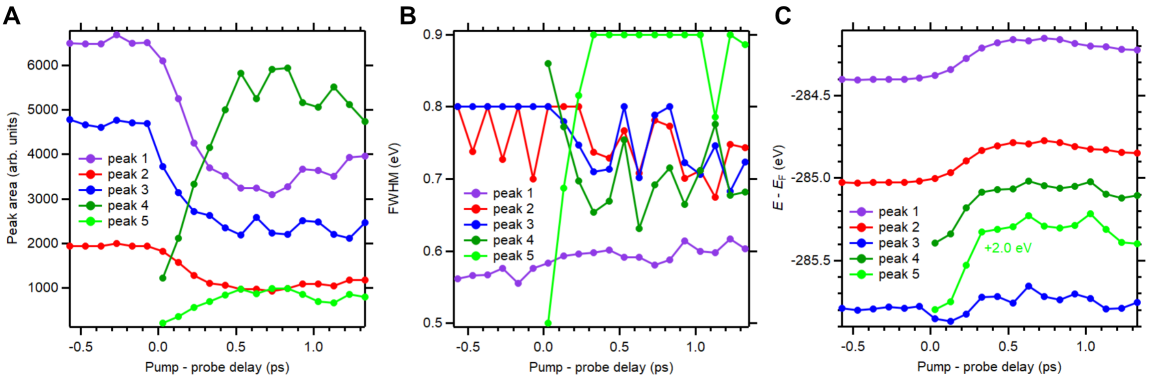

Figure 4.12: Fitting results for C 1*s* core level dynamics. **A** Peak area, **B** peak width and **C** energetic position of peaks 1-5, which are assigned to carbon atoms in different chemical environments in the main text.

For fitting all experimental C 1*s* spectra before t_0 six gaussian peaks were implemented, three peaks for the main peaks 1 through 3 (solid lines) and another three peaks for describing their corresponding shake-up satellites (dashed lines). The fitting results are summarized in Fig. 4.12 with the values for individual peak areas in A, peak widths in B and energetic positions in C.

Already visible in the spectrum in Fig. 4.11 B at t_0, the spectral shape starts to change with intensities increasing energetically below and above peak 3. We connect the changing spectral shape to the charge transfer process between a fraction of the CuPc molecules and the substrate and assume that the spectra between t_0 and t_2' must contain the signatures of both positively charged molecules ($CuPc^+$) and molecules remaining neutral ($CuPc^0$) (see top part of Fig. 4.11 C).

After lifting intial constraints in the fitting procedure (but keeping the relative distance and intensity between peaks 1 and 2 fixed), the signature of $CuPc^0$ is found in all spectra after t_0. As evaluated from Fig. 4.12 A, the intensities of all peaks related to $CuPc^0$ (peak 1, peak 2, peak 3) decrease with $\tau_{\text{peak1,decrease}} = (264 \pm 72)$ fs and recover again with $\tau_{\text{peak1,increase}} = (588 \pm 50)$ fs. Both relaxation constants agree with those of the HOMO within their error. Simultaneously, new peaks emerge at -285.4 eV (peak 4, dark green) and at -285.8 eV (peak 5, light green), which are fitted by two additional gaussian peaks and are

attributed to the CC and CN species of $CuPc^+$, respectively. The intensity evolution of these new peaks behaves complementary to those of $CuPc^0$ and their according values for $\tau_{peak4,increase} = (403 \pm 150)$ fs and $\tau_{peak4,decrease} = (500 \pm 150)$ fs also coincide within their error.

From the fitted energetic positions in Fig. 4.12 C we find that the energetic positions of peak 4 and peak 5 appear shifted towards higher binding energies by (700 ± 10) meV and by (900 ± 10) meV with respect to peak 1 and peak 3. The overall blue-shift of photoexcited $CuPc^+$ is explained by a different core electron stabilization in the charged molecule and by reduced screening of the photoemitted core hole after hot hole transfer to the HOMO. The non-uniform shifts of the CC and CN species on the other hand are likely related to the inhomogeneous HOMO wave function amplitude at different atomic sites in the molecule. The fraction of the positive charge, which is located in the HOMO due to hot hole transfer from the substrate, is thus inequally seen by carbon atoms located at different sites and inequally affects their binding energy shift.

This interpretation has been recently elaborated by a theoretical study on the impact of tr-XPS measurements on spectra of small, cyclic molecules [200] and is also substantiated by the core level study of isolated $CuPc^+$ performed by M. Reuner and D. Popova-Gorelova shown by the green, dashed line in Fig. 4.11 B. The vertical green lines, which mark the energetic positions and intensities of different carbon species in $CuPc^+$, are energetically further separated than for $CuPc^0$. In the experiment this is observed as an increased energetic distance by (70 ± 10) meV between the CC and CN peak in $CuPc^+$ as compared to in $CuPc^0$ (see Fig. 4.12 C). Also, the CC peak 4 in $CuPc^+$ is broadened in energy by (15 ± 5) meV in comparison to the CC peak 1 in $CuPc^0$ – this is observed in both the Gaussian fitting procedure (see Fig. 4.12 B) and the more advanced theoretical study (see Fig. 4.11 B, top).

Additionally to the blue-shift of $CuPc^+$, a rigid red-shift of $CuPc^0$ by up to (260 ± 10) meV is observed, which is shown in the fit results in Fig. 4.12 C and which is marked by the pink, dashed line in Fig. 4.11 B, connecting the position of peak 1 at t_{-1} and at t_1. This red-shift has also been seen for the HOMO in Fig. 4.10 C and will be addressed in a later subsection.

The energetic separation between chemically inequivalent carbon species in the C 1*s* spectra allows us to disentangle the signatures of $CuPc^+$ and $CuPc^0$. By comparison of relative peak areas we quantify the maximal fraction of positively charged molecules $CuPc^+$/CuPc to be (45 ± 2) %. This fraction is surprisingly large, considering that the LUMO of only less than 1 % of the molecules becomes negatively charged by electron transfer across the interface at t_0. In other pump-probe experiments studying charge transfer processes for adsorbed molecules, typically only ~ 1 % of the molecules are directly excited and thus involved in charge transfer, even though the experiments are performed with comparable excitation fluences (between $\sim$ 10-100 μJ/cm^2) [22, 194]. Even though different parameters such as light

polarization, angle of incidence and excitation energy impact the excitation cross-section and thus the charge transfer efficiency, these will not explain the large amount of molecules involved in charge transfer at the photoexcited CuPc/$TiSe_2$ interface. Instead, we attribute the charging of (45 ± 2) % of the CuPc molecules to the high charge carrier injection efficiency of $TiSe_2$ and the energetic location of the HOMO close to E_F. Charge carriers are mainly generated within the substrate and are confined inside the atomically thin van-der-Waals layers at the interface with close proximity to the adsorbates. Furthermore, the proximity between substrate and adsorbate states in energy-momentum space – the small, indirect band gap in $TiSe_2$ and HOMO position just below E_F – aids the efficient transfer of hot charge carriers into the HOMO (see previous section).

Fluence Dependence

The excitation of hot charge carriers in $TiSe_2$ with the pump pulse is decisive for the emergent dynamics at the CuPc/$TiSe_2$ interface since the prolonged relaxation dynamics in the substrate lead to the efficient charge transfer into the molecular adsorbate layer. It is shown below that – against expectation – neither the time scale of the dynamics nor the magnitude of interfacial charge transfer are determined by the pump pulse fluence (within the studied range).

The population of the Ti 3*d* band above E_F is governed by impact ionization processes between electrons in the Se 4*p* and Ti 3*d* bands across the band gap. Thereby, it has been shown that the size of the band gap is indirectly proportional to the efficiency and speed of the impact ionization processes [104]. Since the pump fluence determines not only the number of excited charge carriers, which may participate in impact ionization, but also affects the local sample temperature that is connected to the sample's band gap, a faster thermalization in $TiSe_2$ is expected for larger pump fluences.

To my knowledge, systematic fluence dependent studies in literature have targeted $TiSe_2$ only in its charge density wave (CDW) phase, where a non-linear CDW melting behavior has been observed for fluences between (1 - 1500) μJ/cm^2 [28, 104, 201–203]. At 200 K, the maximum population in the Ti 3*d* band of clean $TiSe_2$ is reached 200 fs after optical excitation with a pump fluence of 0.5 mJ/cm^2 [104]. With pump fluences increasing up to $\sim$ 1500 mJ/cm^2 this time decreases down to $\sim$ 20 fs [28]. At room temperature, the delayed population in the Ti 3*d* band was stated to reach its maximum after 50 fs for a pump fluence of 0.25 mJ/cm^2 [201], at 200 fs for a fluence of 0.5 mJ/cm^2 [204] and at 150 fs for a fluence of 2.1 mJ/cm^2 [205]. Although these values are not part of a consistent fluence dependence study in a fixed experimental environment, they indicate a non-linear relationship with the longest thermalization times observed at intermediate pump fluences.

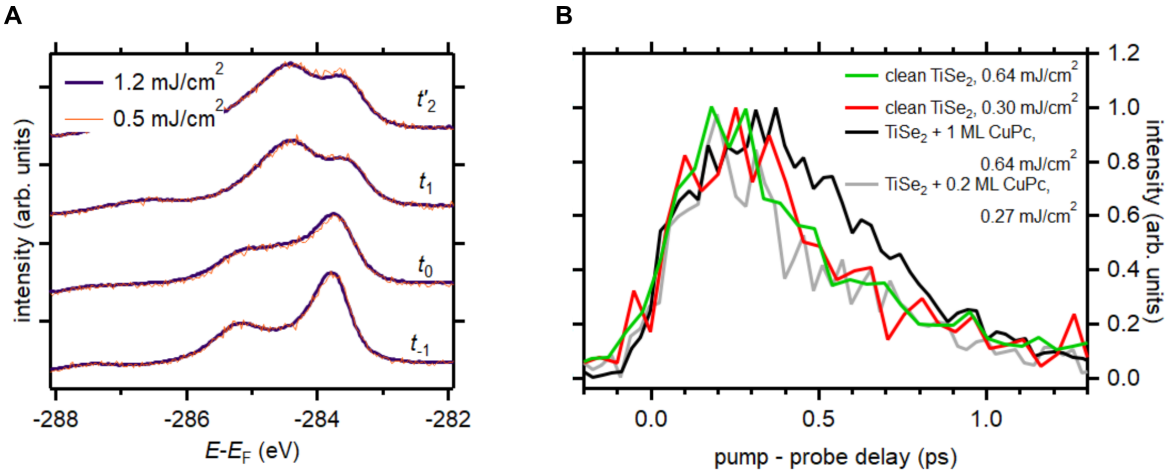

Figure 4.13: Pump pulse fluence dependence of core level and valence band data of CuPc/$TiSe_2$. **A** C 1*s* core level spectra at four selected pump-probe delay times measured with varying pump pulse fluence on one $TiSe_2$ sample with monolayer CuPc coverage. **B** Comparison of Ti 3*d* population dynamics above E_F of four different samples under varying excitation conditions.

In this work, spectra have been measured with varying pump pulse fluences (see Fig. 4.13). They indicate that the observed charge transfer dynamics are not limited by the pump pulse fluence but rather by the adsorbate coverage.

The magnitude of charge transfer under different pump fluences can be quantified by tr-XPS: in Fig. 4.13 A, four C 1*s* core level spectra are presented at selected pump-probe delay times. They have been obtained on one sample with a coverage of one monolayer CuPc atop $TiSe_2$ but with different pump excitation fluences. Spectra obtained with a pump pulse fluence of 1.2 mJ/cm^2 (black line) are overlaid by spectra, which were measured with 0.5 mJ/cm^2 pump pulse fluence. Due to a shorter measurement duration, the latter spectra appear noisier, but still both datasets clearly show the same dynamics. Since no line shape change is observed by almost doubling the pump fluence, we can state that the amount of interfacial charge transfer is independent of the excitation fluence within the studied range.

The time scale for the charge transfer process under different excitation conditions is traced in the Ti 3*d* band: in Fig. 4.13 B, the population dynamics in Ti 3*d* above E_F are compared for different samples and different pump pulse fluences. A clean $TiSe_2$ substrate was excited with 0.30 mJ/cm^2 (red line) and with 0.64 mJ/cm^2 (green line). Within their noise level, both show the same transient population reaching a maximum after ~ 200 fs - similar to the value stated in literature [204]. The other two curves in this graph present $TiSe_2$ samples with varying CuPc coverages: the sample with monolayer coverage (black line) was excited with 0.64 mJ/cm^2 and a sample with a coverage of (0.2 ± 0.1) monolayers CuPc (grey line) was excited with 0.27 mJ/cm^2. Interestingly, the sample with low coverage follows the same dynamics as the clean substrate sample, but for the monolayer coverage

an increased spectral weight reaching a maximum after 375 fs is observed. Additional measurements at intermediate coverages would benefit the understanding of this observation. At this point, one may speculate that an efficient involvement of the molecules in the $TiSe_2$ relaxation process only becomes relevant at higher coverages, when molecules are locked into a fixed adsorbate overstructure.

Charge Separation Induced Shifting of Interfacial Energy Levels

As hot holes populate (45 ± 2) % of the CuPc molecules, a rigid shift by ~ 200 meV towards E_F is observed for all states. The transient magnitude of this shift is evaluated in Fig. 4.14 A for the C 1*s* core level of $CuPc^0$ (peak 1, purple line), for the HOMO (black line) and for the Se 4*p* band maximum at the Γ-point (grey line). Note, that the shifts for the HOMO ((130 ± 5) meV) and for the Se 4*p* maximum ((180 ± 5) meV) are slightly smaller than for the C 1*s* core level ((260 ± 5) meV), since they are limited by the proximity of E_F.

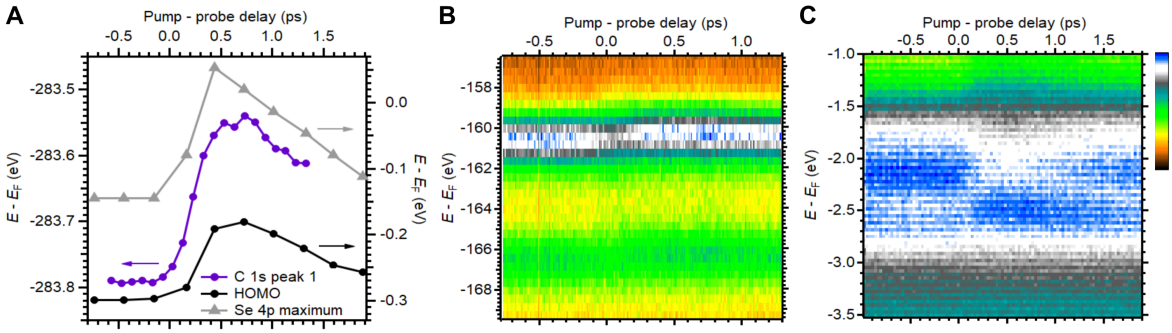

Figure 4.14: Charge separation induced surface potential modulation. **A** Evaluated energy shifts in time of the $CuPc^0$ C 1*s* core level (peak 1, purple line), the HOMO (black line) and the Se 4*p* band maximum at the Γ-point (grey line). **B** Energetic shifts for molecular states in the valence region and **C** for the Se 3*p* bands.

The same red-shift is observed also for the Se 3*p* band (B) and other molecular states in the valence region (C). Additionally to the rigid red-shift, spectral weight is shifted towards higher binding energies for the molecular valence states – similar to the observed spectral weight evolution in the C 1*s* core level (see Fig. 4.11). For clean $TiSe_2$ at room temperature, such a rigid shifting of all states has not been observed in literature [201]. Thus, we relate this effect to the involvement of the CuPc adsorbate layer in the $TiSe_2$ thermalization process, which leads to a charge separation across the hybrid interface. As a result from spatially localizing positive charges within (45 ± 2) % of the molecules, the sample's surface potential becomes modulated. In a photoemission experiment, the average vertical potential difference is then observed as a shift of all states in energy.

With help of a simplified dielectric model, the *dielectric continuum model* which was introduced in chapter 2.1, these shifts as well as the relative shifts between $CuPc^0$ and $CuPc^+$

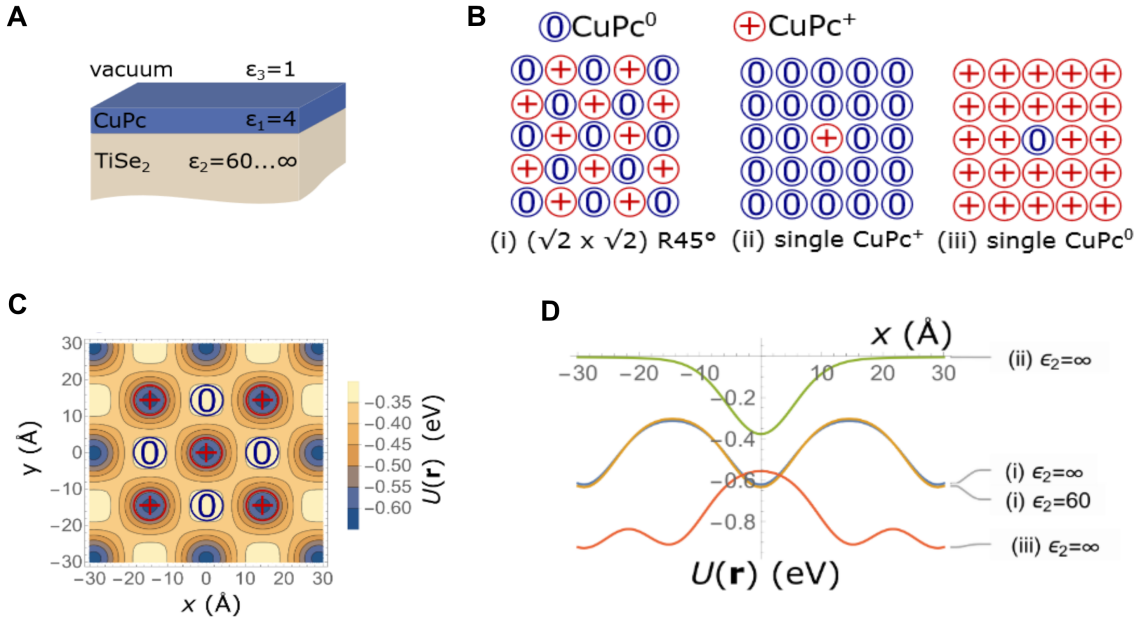

E

Model	$CuPc^+$ (eV)	$CuPc^0$ (eV)
(i) $(\sqrt{2} \times \sqrt{2})$ R45° cell, $\varepsilon_2 = 60$	-0.6	-0.3
(i) $(\sqrt{2} \times \sqrt{2})$ R45° cell, $\varepsilon_2 = \infty$	-0.6	-0.3
(ii) (10×10) cell, single $CuPc^+$, $\varepsilon_2 = \infty$	-0.4	0.0
(iii)(10×10) cell, single $CuPc^0$, $\varepsilon_2 = \infty$	-0.9	-0.6
Experiment	-0.843 (core level)	-0.08 (HOMO) +0.05 (core level)

Figure 4.15: Calculations for the charge separation induced surface potential modulation. Model for surface potential calculations in **A** side-view and **B** top-view. **C** Calculated surface potential modulations (provided by T. Wehling) in top-view for an alternating charge arrangement in the molecular layer and **D** as vertical linecuts for all charge arrangements. **E** Summarized values for calculated and experimental energy shifts in the molecular layer relative to the substrate (Se 4*p* band maximum).

with respect to the substrate can be understood in terms of classical electrostatics. The following calculations have been performed by T. Wehling (University of Hamburg) and consider a quasi two-dimensional adsorbate layer with $\varepsilon_r = \varepsilon_1 = 4$ [206] and $h = 3.95$ Å, which is sandwiched in between a semi-infinite substrate with $\varepsilon_r = \varepsilon_2 = 60$ [207] (and when assuming a perfect metal $\varepsilon_2 = \infty$) below and vacuum with $\varepsilon_r = \varepsilon_3 = 1$ above (see Fig. 4.15 A). Within the adsorbate layer, molecules are arranged in a quadratic 10x10 cluster with a lattice constant of 14.5 Å. Positive charges are introduced to a fraction of the molecules, while the opposite amount of charge is carried by the substrate, the sample thus remains neutral. Since the arrangement of charges within the adsorbate layer is not known from the experiment, three scenarios are considered (see Fig. 4.15 B): (i) alternating positive and neutral charges, (ii) a single positive charge surrounded by neutral charges and (iii) a single neutral charge surrounded by positive charges. Thereby, all positive charges are modeled by

Gaussian shaped charge densities with a width of 5 Å and a charge of $+e$. The screened potential at different positions inside the adsorbate layer $V_{\text{screened}}(\mathbf{r})$ is then calculated following equations (2.2) and (2.4). After defining the potential at the substrate surface to be zero, $V_{\text{screened}}(\mathbf{r})$ is shown in Fig. 4.15 C for configuration (i) (V_{screened} is denoted as $U(\mathbf{r})$ here). Cuts along x are shown in D for all charge arrangement models (i)-(iii).

As expected from having localized charges at the sample surface, potential modulations arise between the positions of $CuPc^0$ and $CuPc^+$ in all models. Noteably, almost no difference is seen in model (i) when exchanging ε_2=60 for ε_2=∞. Therefore, the screening length r_{TF} in $TiSe_2$ is deduced to be similarily small as in a metal. The determined shifts at the $CuPc^0$ and $CuPc^+$ centers with respect to $TiSe_2$ are summarized in Fig. 4.15 E and are compared to experimental shifts of the C 1s core level (peak 1) and HOMO relative to the Se 4p band maximum. In all calculations the potential difference at the $CuPc^0$ and $CuPc^+$ centers amounts to ~ 0.3 eV, while an energetic distance of ~ 0.85 eV is observed in the experiment. The absolute values for the calculated adsorbate shifts relative to $TiSe_2$ show some quantitative uncertainty with respect to the experiment. But considering that the model at hand was not optimized for a best fit, the observed shifts are qualitatively reproduced.

Aside from the relative potential modulations, the average vertical potential inside the adsorbate layer is differently offset with respect to the substrate potential depending on the model, which would translate to the rigid shift observed in the experiment. For model (i) an average vertical potential difference $\Delta V = 0.42$ eV is determined (see equation (2.5)), which comes close to the experimental red-shift by (260 ± 10) meV (C 1s core level). Due to the qualitative agreement between experiment and theory we conclude that the observed shifts upon interfacial hot hole transfer are to a significant extent of electrostatic nature.

4.2.2.2 Structural Dynamics

Simultaneous to the electronic dynamics – hot hole transfer into (45 ± 2) % of the molecules and modulation of the surface potential – structural changes occur within the hybrid interface. Such changes are observed on both a microscopic and macroscopic scale: while the charge transfer interaction between $CuPc^+$ and the substrate induces structural rearrangements within $CuPc^+$ on the intramolecular level, simultaneous in-plane rotations within (60 ± 10) % of the molecules are traced on a length scale of $\sim (200 \text{ x } 100)\ \mu\text{m}^2$.

Due to the focussed directionality of electron scattering at higher E_{kin}, structural information is easier to reconstruct from XPD data at the C 1s core level than from the momentum distribution of molecular frontier orbitals. But when assuming that the orbital shape is tied to the atomic structure of a molecule – which is a reasonable assumption even when probing the excited state with a temporal resolution of (95 ± 5) fs – structural rearrangements

can also be indirectly inferred from the transient HOMO momentum distribution. This allows for a cross-check between the two independent measurements at the HOMO and C 1*s* core level and can strengthen the conclusions drawn from the XPD analysis, which may be complicated by limitations in the theoretical model as well as in the experimental resolution.

Structural Dynamics Inferred from the CuPc HOMO Data

From the transient HOMO momentum distribution, three parameters are evaluated and traced in time: the average lateral extent of the twelve intensity maxima forming the 'HOMO ring' labeled 'HOMO ring width' (indicated by white arrows in Fig. 4.16 A), their average distance from the Γ-point labeled 'HOMO ring radius' (red arrow) and their azimuthal position along the HOMO ring circumference (dashed, red line). For data analysis, the momentum distribution at the HOMO energy is masked as shown in A in order to isolate HOMO intensities from substrate derived features. Then, the coordinates of the masked data are converted from (k_x, k_y) into (azimuthal angle, $\mathbf{k}_{||}$) values, which facilitates tracing changes in the lateral position and extent of the HOMO maxima. The HOMO ring width and radius are evaluated by integrating over all azimuthal angles and by fitting the intensity distribution of the HOMO along the polar angle ($\mathbf{k}_{||}$ values) with a Gaussian.

The transient evaluation of the HOMO ring width (black line) and radius (red line) is shown in Fig. 4.16 B with error bars according to the fit quality. The underlying dataset is binned over 250 fs in time. On the time scale of hot hole transfer an increase of the HOMO ring width by up to $(27 \pm 1)\,\%$ is observed while the HOMO ring radius simultaneously decreases by $(2.1 \pm 0.3)\,\%$. The initial value of $1.67\,\text{Å}^{-1}$ for the HOMO ring radius can be translated into an intermolecular distance of 7.5 Å in real-space by a Fourier transform. Such a distance is found in CuPc as the diameter of the azaporphyrin ring and as the distance between the outer-most carbon atoms in the benzene rings to the azaporphyrin ring [18]. The observed reduction of the HOMO ring radius in momentum space thus indicates an increase of these distances in real-space.

These findings are corroborated by calculations on isolated CuPc and $CuPc^+$ which were performed by M. Reuner and D. Popova-Gorelova. Different atomic structures are found for CuPc in its ground state (marked by the purple cross in Fig. 4.16 C) as compared to $CuPc^+$ in its relaxed ionized state configuration (green cross). The structural differences are marked in Fig. 4.16 C by red arrows pointing from atomic positions in CuPc towards their direction of displacement in $CuPc^+$. Based on these structures HOMO momentum distributions are evaluated and compared: with respect to CuPc, a theoretical HOMO ring radius reduction by 0.4 % and a HOMO ring width reduction by 12 % is evaluated for $CuPc^+$. Even though the magnitude of the HOMO ring radius reduction is smaller in the simulation than in the ex-

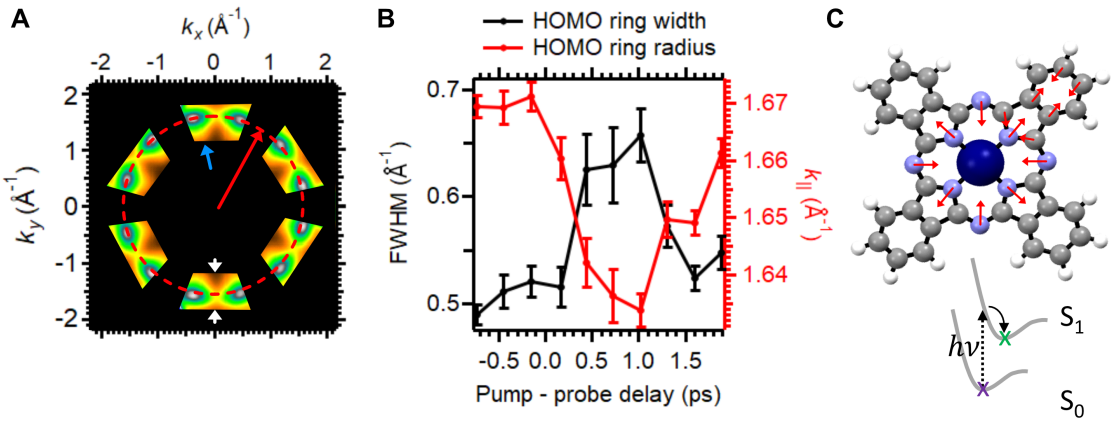

Figure 4.16: Transient momentum distribution of the CuPc HOMO. A Sketch of evaluated parameters in the HOMO momentum distribution. **B** Transient width (black line, left axis) and radius (red line, right axis) of the HOMO ring in momentum space. **C** Illustrated atomic in-plane rearrangements between CuPc in its ground state (purple cross) and $CuPc^+$ in its relaxed excited state configuration (green cross). Red arrows point in the direction of atomic displacements in $CuPc^+$.

periment, possibly due to the neglect of out-of-plane deformations induced by the substrate, the trend is qualitatively reproduced. We thus reason that structural rearrangements in in-plane direction occur within $CuPc^+$ during hot hole transfer from the substrate. Note, that these in-plane rearrangements are expected to be accompanied by much larger out-of-plane deformations since the resetting force of displaced atoms is much weaker in out-of-plane direction for planar molecules. Values of $\sim 30\,\%$ have been reported in literature for out-of-plane distortions in charged CuPc as the result of Coulomb repulsion from the substrate [76].

Aside from the neglect of the substrate in the simulation one should note that the experimental data include both signatures from $CuPc^0$ and $CuPc^+$ after t_0. This explains why contrary to expectation from the simulation an increase of the HOMO ring width is experimentally observed after t_0: assuming that the HOMO ring radius of neutral CuPc and $CuPc^0$ remains the same, then the shift of $CuPc^+$ features closer to the Γ-point will broaden the evaluated average HOMO ring width.

Lastly, the positions of the twelve intensity maxima along the HOMO ring circumference (dashed red line in Fig. 4.16 A) are traced in time. For a better presentation of the dynamics in the individual maxima, a close-up of one maximum (marked in A by blue arrow) is shown in Fig. 4.17 A at t_{-1} and in B at t_1. The data is treated with a Gaussian filter and is displayed in coordinates of azimuthal angle and $\mathbf{k}_{||}$. Thereby changes in the HOMO ring radius can be directly seen as deviations from the horizontal arrangement of the intensity maxima. At t_{-1} (A), the position of the viewed HOMO intensity maximum is labeled 'a' and appears

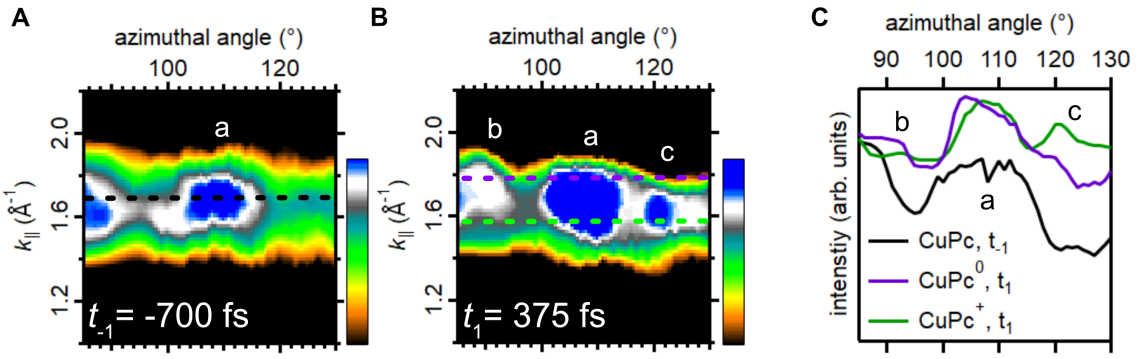

Figure 4.17: Transient momentum distribution of the CuPc HOMO. Momentum distribution of the HOMO in azimuthal angle versus $k_{||}$ presentation at *A* t_{-1} and at **B** t_1. Only a zoomed in sector is shown, which is marked in Fig. 4.16 A by a blue arrow. **C** Linecuts along the dashed lines in A and B, show the appearance of additional features at azimuthal angles of $(15 \pm 3)^\circ$ next to the main intensity.

centered at $\mathbf{k}_{||} = 1.67$ Å^{-1}. At t_1, the intensity in the HOMO is reduced by (30 ± 5) % due to hot hole transfer, therefor the data shown in B is depicted overly saturated in order to visually enhance the appearance of two new features 'b' and 'c'. The positions of these new features 'b' and 'c' are rotated by an azimuthal angle of $\pm(15 \pm 3)^\circ$ with respect to 'a' and they are present in addition to the twelve initial HOMO maxima at t_{-1}. This results in a total of 24 intensity maxima along the HOMO ring circumference at t_1, with an azimuthal separation by $(15 \pm 3)^\circ$ between each maximum. This doubling of HOMO derived features at t_1 suggests that additional domains are present during hot hole transfer, in which CuPc molecules are reoriented with an in-plane angle of $\pm(15 \pm 3)^\circ$ with respect to their initial rotation. At t_2, the initial shape of the HOMO momentum distribution is nearly recovered and features 'b' and 'c' are no longer visible.

Next to appearing rotated in azimuthal direction, the feature at 'c' is centered at a slightly smaller $\mathbf{k}_{||}$ value in comparison to 'a'. Because the signature of CuPc$^+$ is expected to appear closer to the Γ-point, the intensity at 'c' likely originates from CuPc$^+$ molecules. The feature at 'b' is less intense than the other features. In order to compare the lateral extents of all features, azimuthal linecuts are extracted along the dashed lines in Fig. 4.17 A and B and are presented in C. At t_1, two linecuts are extracted - one at smaller $\mathbf{k}_{||}$ (green) and one at larger $\mathbf{k}_{||}$ (purple). The feature at 'a' is present in all linecuts at t_{-1} (black) and t_1 (purple, green). At t_1 additional intensites emerge at 'b' and 'c' that are observed as non-vanishing intensities in, both, the green and purple linecut. But, while the feature at 'c' is more prominent at smaller $\mathbf{k}_{||}$ values (green linecut) the feature at 'b' is more intense at larger $\mathbf{k}_{||}$ values (purple linecut). From this we can conclude: the intensity at 'c' mainly contains the signature of CuPc$^+$ molecules. The intensity at 'b' contains less thereof. As the spectral weight at 'b' is largely centered at the same $\mathbf{k}_{||}$ value as the feature at 'a', it is at-

tributed to $CuPc^0$ molecules. This will be further substantiated with the XPD measurements shown below. Note, that no quantitative information is deduced from the peak intensities in C. Not only does the reduced intensity in the HOMO of $CuPc^+$ impair the comparison of features at t_1, but also experimental factors such as the low E_{kin} and inequal photoemission matrix elements for rotated molecules complicate a direct quantitative comparison.

Structural Dynamics Reconstructed from the C 1*s* Core Level Data

The effect of elastic photoelectron scattering to the C 1*s* momentum distribution is expected to result in intensity variations below 1 % at the given E_{kin} and experimental settings [26]. Thus, a careful normalization of the background intensity is essential prior to evaluation of the tr-XPD data. To do so, two momentum maps were extracted at energies smaller and larger than the C 1*s* peak signature - at -281.0 eV and at -289.0 eV. At these energies no momentum dependent sample features are expected and the obtained momentum distributions reflect the experimental background of inelastically scattered photoelectrons as well as detector related artifacts such as irregular illumination or visibility of the delay line detector (DLD) grid. In order to compensate for these pixel dependent irregularities, a linear function is determined for every individual pixel by connecting the intensities in both momentum maps. This linear function is then subtracted from each momentum map in the C 1*s* spectrum. Afterwards, a constant background is subtracted from each momentum map and their intensities are normalized to 1. Due to a detector related artifact at large $\mathbf{k}_{||}$ in one DLD panel only data with $\mathbf{k}_{||} < 1.5$ Å^{-1} is evaluated and shown here. Furthermore, the data is smoothed in momentum space with a gaussian filter.

Due to the energetic separation between the C 1*s* spectra of CuPc, $CuPc^+$ and $CuPc^0$ (see Fig. 4.18 A), their momentum dependent signatures can be individually visualized and analyzed. In Fig. 4.18 B-D the momentum distributions of CC carbon atoms in CuPc (peak1, t_{-1}, purple), $CuPc^+$ (peak 4, t_1, green) and $CuPc^0$ (peak 1, t_1, pink) are shown. Their energetic integration windows are marked in A by correspondingly colored rectangles. For the CC peak in CuPc (B) the momentum map is marked by six prominent intensity maxima, which are circularly arranged around the Γ-point at a distance of ~ 1.1 Å^{-1}. In $CuPc^+$ (C), the signature of the CC peak is noteably changed - here, three prominent intensity maxima surround the Γ-point at different azimuthal $\mathbf{k}_{||}$ values. The signature of CC peaks in $CuPc^0$ (D), though, resembles the one of CuPc.

In order to obtain structural information from these experimental XPD patterns, they are compared to a series of simulated momentum maps, each based on a possible sample geometry, and their agreement is quantified by evaluation of the R-factor (see chapter 3.2.2). Thereby, an initially guessed sample geometry, which serves as input for the simulation,

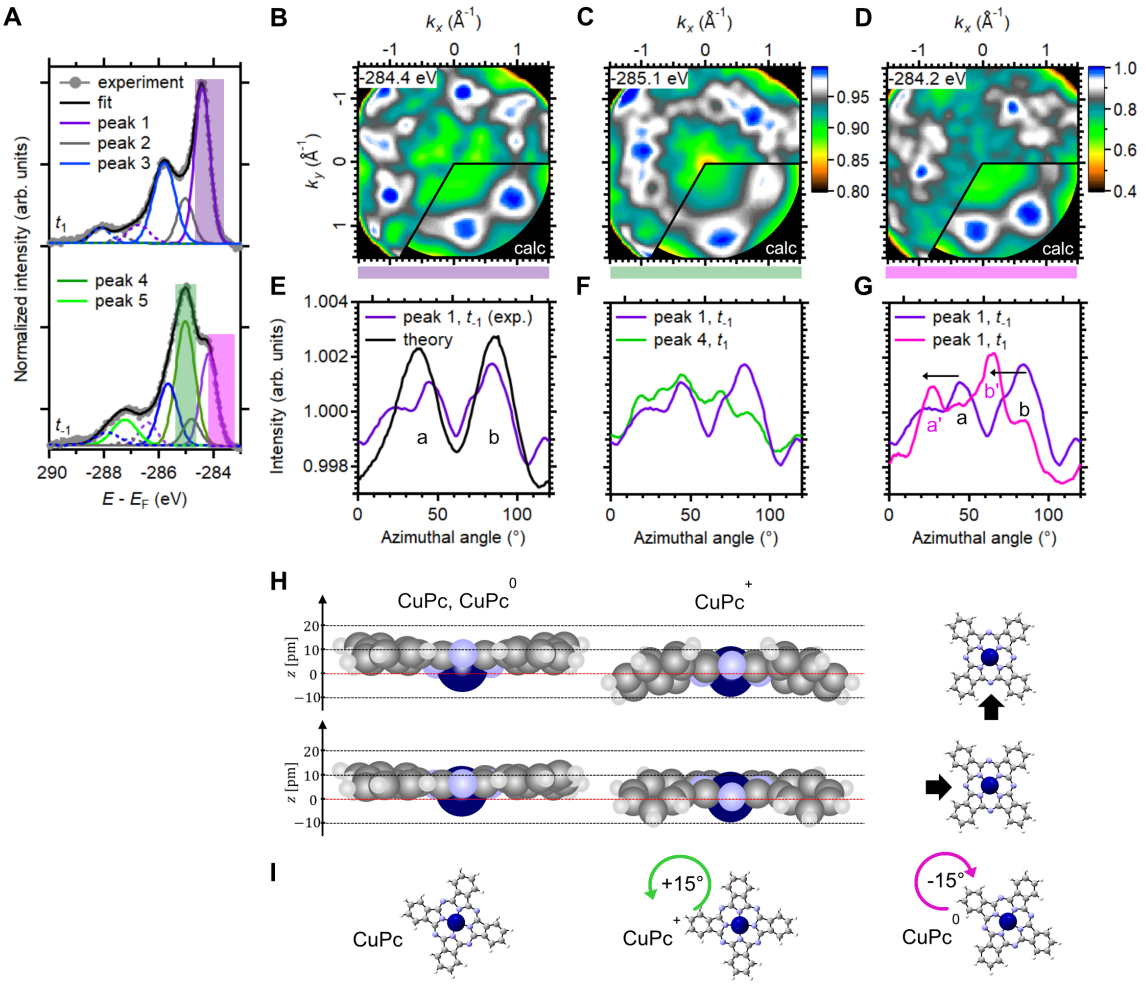

Figure 4.18: XPD at the CuPc C 1*s* core level. **A** C 1*s* core level spectra at t_{-1} and t_1 with marked integration ranges for XPD patterns of **B** the CC atoms in CuPc (purple), **C** the CC atoms in $CuPc^+$ (green) and **D** the CC atoms in $CuPc^0$ (pink). The corresponding simulations are overlaid to the bottom thirds of **B**-**C**. Azimuthal linecuts at $\mathbf{k}_{||} = (1.0 \pm 0.2)\,\text{Å}^{-1}$ for the CC atoms in CuPc in comparison to **E** the simulation, **F** the CC atoms in $CuPc^+$ and **G** the CC atoms in $CuPc^0$. **H** Side-view and **I** azimuthal orientation of CuPc models for CuPc, $CuPc^0$ and $CuPc^+$.

is iteratively adjusted such that the lowest possible R-factor value is obtained and is then considered as the model closest to the geometry in the experiment. In the bottom thirds of Fig. 4.18 B-D, sections of the simulations are shown, which are associated with the closest geometric model of CuPc, $CuPc^+$ and $CuPc^0$. R-factors of a total of 43 different geometric models were evaluated, which are summarized in Fig. 4.19. The simulations were performed by K. Niki, M. Nozaki and M. Haniuda from the university of Chiba, Japan, and are based on their developed multiple scattering theory which has been published recently [208]. The calculations are based on a single CuPc molecule placed at an adsorption height of 3.16 Å^{-1} atop a cluster of 58 atoms modeling the substrate. This adsorption height was

found to reproduce the interfacial momentum distribution at the HOMO energy best. Then, the momentum maps for photoemission from each of the 32 carbon atoms in CuPc were calculated considering multiple intramolecular and interfacial scattering processes. For comparison with the experimental data in Fig. 4.18 B-D, the sum of all 24 momentum maps stemming from CC atoms was taken. To account for the molecular arrangement in (at least) three domains according to the substrate symmetry, three model calculations were added, in which the molecule was rotated by 0°, 120° and 240° relative to the substrate. The polarization dependence of the momentum maps shown in B-D is lost since the simulation is three-fold symmetrized according to the experimental data treatment.

To further assess the resemblance between experiment and simulation, azimuthal linecuts along the prominent intensity maxima at $\mathbf{k}_{||} = (1.0 \pm 0.2)\,\text{Å}^{-1}$ are extracted from the experimental and calculated data in Fig. 4.18 B and shown in E. Due to the three-fold symmetry of the data only a section of 120° is shown here. Both, the linecuts through the experimental data at t_{-1} (purple) and the calculation (black) are characterized by two repeated intensity maxima labeled 'a' and 'b'. After normalizing the linecuts at their mean intensity, their relative intensity variations can be evaluated, which serve as a measure for the homogeneity or ordering in the sample: in the calculation and experiment variations by $(0.40 \pm 0.05)\,\%$ and by $(0.20 \pm 0.05)\,\%$ are extracted, respectively. The smaller value found in the experiment may be explained by either the influence of additional scattering channels which have not been considered in theory, e.g. additional growth domains or defect states, or it may reflect that the chosen integration window (purple rectangle in A) also partially integrates over other signatures of, e.g., shake-up satellites or vibronic progressions included in peak 2. Still, the order of magnitude of the intensity variations is in agreement with values found in literature for XPD measurements on graphene at similar experimental parameters [26]. In Fig. 4.18 F and G, respectively, the azimuthal linecuts along the prominent features in the momentum maps of CC atoms in $CuPc^+$ (green) and $CuPc^0$ (pink) are presented in comparison to the corresponding linecut in CuPc (purple). Note, that while the integration window of $CuPc^+$ (green rectangle in A) does not allow for a clear separation between signatures of $CuPc^+$ and $CuPc^0$ resulting in a slightly smaller intensity variation, the signal of CC atoms in $CuPc^0$ is easier to isolate and thus shows larger intensity variations of $(0.30 \pm 0.05)\,\%$.

A list of all investigated molecular structures, their side-views and R-factors with respect to the experimental data are presented in Fig. 4.19. Those molecular structures that correspond to the smallest evaluated R-factors (0.47 for CuPc, 0.54 for $CuPc^0$ and 0.46 for $CuPc^+$) come closest to the experimental geometry and are shown in Fig. 4.18 H. Both, CuPc and $CuPc^0$ are in a nearly flat-lying adsorption geometry atop $TiSe_2$. Note, that the atomic radii are scaled by a factor of 0.1 for better visualization of out-of-plane displacements relative to the adsorption height (dashed, red line). In the structure found for $CuPc^+$

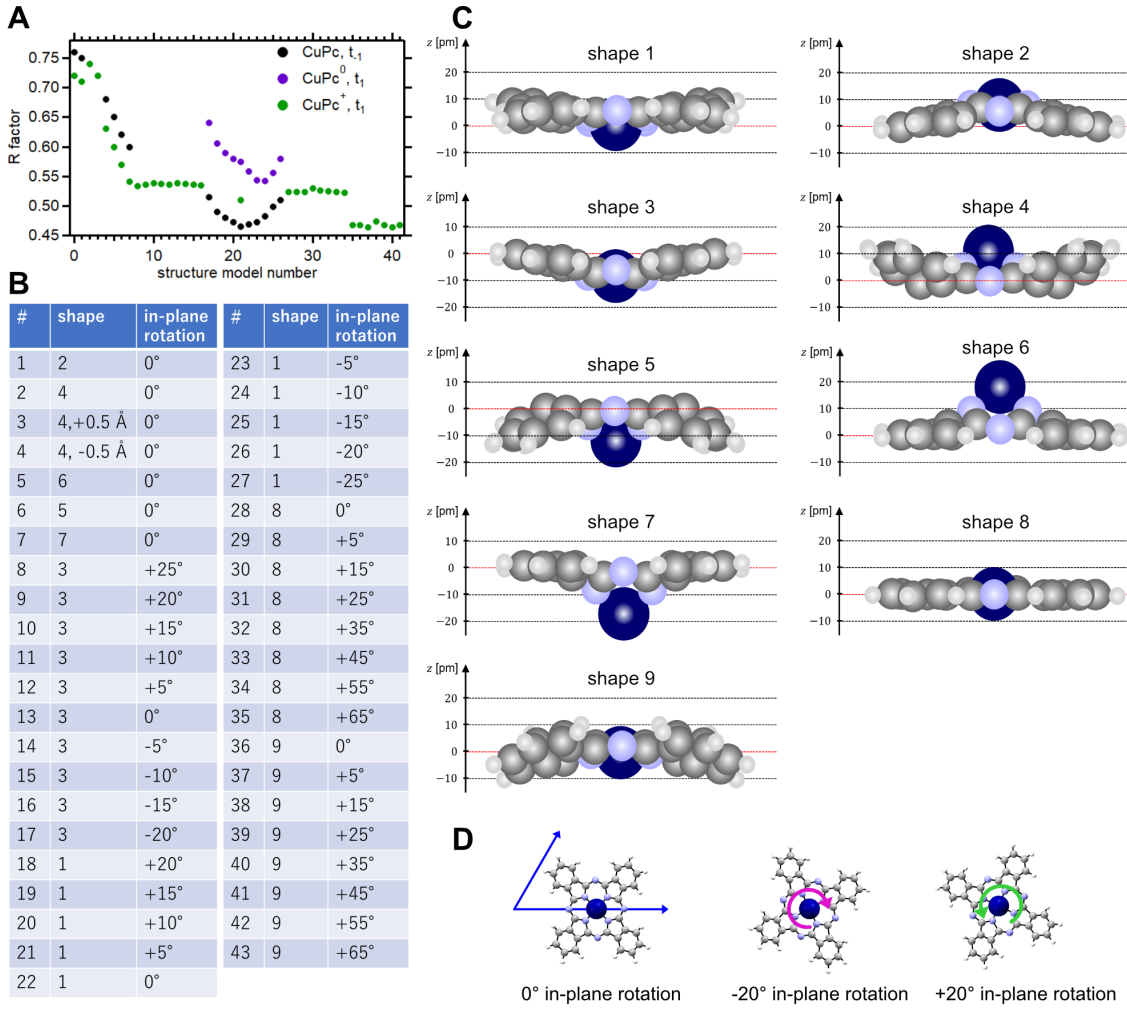

#	shape	in-plane rotation	#	shape	in-plane rotation
1	2	0°	23	1	-5°
2	4	0°	24	1	-10°
3	4,+0.5 Å	0°	25	1	-15°
4	4, -0.5 Å	0°	26	1	-20°
5	6	0°	27	1	-25°
6	5	0°	28	8	0°
7	7	0°	29	8	+5°
8	3	+25°	30	8	+15°
9	3	+20°	31	8	+25°
10	3	+15°	32	8	+35°
11	3	+10°	33	8	+45°
12	3	+5°	34	8	+55°
13	3	0°	35	8	+65°
14	3	-5°	36	9	0°
15	3	-10°	37	9	+5°
16	3	-15°	38	9	+15°
17	3	-20°	39	9	+25°
18	1	+20°	40	9	+35°
19	1	+15°	41	9	+45°
20	1	+10°	42	9	+55°
21	1	+5°	43	9	+65°
22	1	0°			

Figure 4.19: R-factor analysis for the CuPc C 1*s* XPD patterns. A Evaluated R-factors between the experimental momentum maps of the CC atoms in CuPc (black), $CuPc^0$ (purple) and $CuPc^+$ (green) and the simulated models, which are listed in **B**. **C** Side-view and **D** top-view of considered molecular structures.

the benzene rings are displaced by nearly 10 pm (0.3 %) in direction of the substrate. When considering that the charge density of the HOMO is largely distributed across the benzene rings, then this site-specific lowering of the molecule's adsorption height can be understood as the result of a temporarily increased interactive strength between the HOMO and the substrate during charge transfer [75].

When comparing the momentum distributions (Fig. 4.18 B and D) and linecuts (G) of CuPc and $CuPc^0$ their overall resemblance is apparent. Both their linecuts are characterized by two prominent intensity maxima labeled 'a', 'b' for CuPc (purple) and 'a" and 'b" for $CuPc^0$ (pink), but the positions of the intensity maxima in $CuPc^0$ appear rotated by $-(15 \pm 3)^\circ$ with respect to those in CuPc. From the XPD calculations we find that the in-

tensity maxima appearing in the momentum distributions around $\mathbf{k}_{||} = (1.0 \pm 0.2)\,\text{Å}^{-1}$ are defined by intramolecular scattering distances and are nearly independent of the molecular adsorption site on the substrate. Features resulting from molecule-substrate scattering mainly appear at larger $\mathbf{k}_{||}$ values which are not evaluated here. Thus, the azimuthal rotation of features in $CuPc^0$ translates to an in-plane rotation of the molecule relative to the substrate.

Not all molecules rotate at t_1: the pink linecut of $CuPc^0$ contains smaller intensities at 'a' and 'b' reminiscent of molecules in their orientation at t_{-1}. A comparison of the relative peak heights at 'b' and 'b" reveals that (60 ± 5) % of $CuPc^0$ molecules rotated by -$(15 \pm 3)^\circ$ at t_1, while the remaining $CuPc^0$ molecules do not rotate. A similar behavior is observed for $CuPc^+$ molecules at t_1: while the in-plane rotation can not be as easily traced in the azimuthal linecut in F since the signature of $CuPc^+$ differs from CuPc, the best agreement with the calculation is found for the model, in which the $CuPc^+$ structure is rotated by +15° with respect to its original position. Similarly as for $CuPc^0$, the amount of rotating $CuPc^+$ molecules is estimated to be (60 ± 10) %. Although, this quantification is afflicted with a larger error of 10 % since $CuPc^+$ features are inseparabely overlaid with other signatures from $CuPc^0$, vibronic progression or shake-up sattelites (see Fig. 4.18 A). In Fig. 4.18 I a summary of the deduced in-plane orientations in the majority of CuPc, $CuPc^+$ and $CuPc^0$ molecules is sketched. The rotation of molecules deduced from tr-XPD agrees with the observations made in the transient HOMO momentum distributions (see previous section). With tr-XPD it is further specified that $CuPc^+$ and $CuPc^0$ molecules are rotated in opposite directions at t_1.

Possible Explanations for the Directed Rotation in the Molecular Film During Hot Hole Transfer

Several questions arise from the observation of the directional movement in $CuPc^0$ and $CuPc^+$: firstly, what causes the rotation of molecules, secondly why is a directional rotation observed for $CuPc^0$ and $CuPc^+$ molecules and thirdly, how come that $\sim 2/3$ of $CuPc^0$ molecules rotate while the remaining $CuPc^0$ molecules stay in their original position? To answer these questions, a few concepts discussing molecule-substrate as well as molecule-molecule interactions will be reviewed briefly in this section and connected to the experimental findings in this thesis.

Molecular Switch?

Rotational movements in molecules in general have been part of the active fields of research on molecular switches and molecular motors since the 1980s with the goal to create molecule-based devices for storing and transmitting information as well as machines for performing mechanical work [1, 16, 209–212]. In 2016, the Nobel prize in chemistry was awarded to J.-P. Sauvage, J. F. Stoddart and B. L. Feringa for designing and synthesizing such molecular machines. To realize molecular switches and machines two requirements need to be met: repetitive rotation and conversion of external energy, e.g. light, chemical or electric energy, into mechanical movement in the molecule [210]. A distinction between switches and motors is made in the reversibility of the rotation: while the rotation is reversible in a molecular switch leading to the recovery of the system's intial state, the rotation in a molecular motor is non-reversible and results in the performance of progressive work [17].

Based on the first requirement, the rotations observed here may be classified as a molecular switching motion occurring on the time-scale of interfacial charge carrier transfer since the system's initial state is recovered after ~ 2 ps. Regarding the second requirement - the conversion of external energy - light is excluded as a direct external stimulus, since the rotation doesn't correlate with the arrival of the pump pulse but rather with the hot hole transfer dynamics and the build-up of the interfacial potential modulation. Thus, the simultaneously altered interactive forces across the interface as well as between neighboring molecules are considered to drive the rotational movement in the molecular film.

Increasing the Overlap between Molecular and Substrate States

To elaborate on this, the in-plane arrangements of molecules at t_{-1} and t_1 are regarded (see Fig. 4.20 A and B, respectively). The arrangement in A is discussed in section 4.2.1 and is deduced from the combined information on the momentum distribution at the HOMO energy (see Fig. 4.6 H) and on the LEED pattern shown in Fig. 4.7 A. Note that the obtained information on the C 1*s* core level (see Fig. 4.18 B) is less reliable regarding relative molecule-to-substrate orientations, because the field-of-view in momentum-space mainly revealed features resulting from intramolecular scattering.

Assuming a checkerboard arrangement of $CuPc^+$ and $CuPc^0$ molecules, then the molecular arrangement shown in Fig. 4.20 B is obtained at t_1 based on the initial configuration shown in A. In B, two opposite benzene rings of $CuPc^0$ and of $CuPc^+$ are now aligned parallel to $\mathbf{s'}_1$ and $\mathbf{s}_2$ of the substrate, respectively. For phthalocyanines atop (111) surfaces such a configuration, in which two opposite benzene rings are aligned with a most densely packed

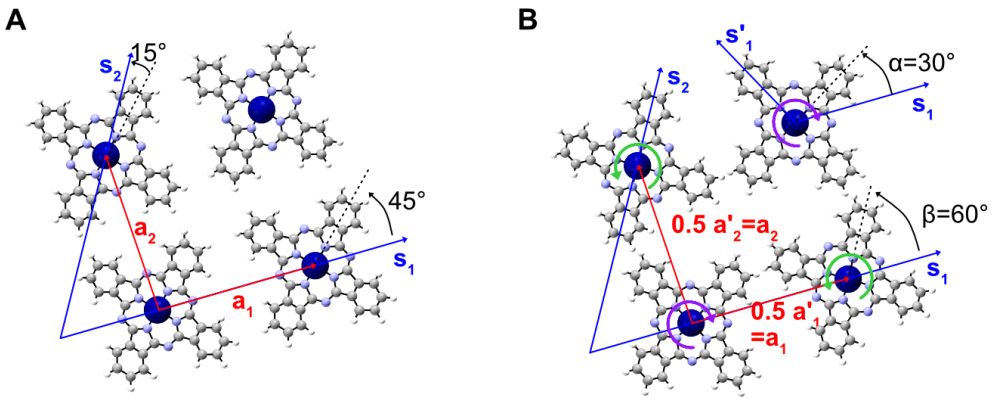

Figure 4.20: Molecular arrangement after sample preparation. **A** Molecular arrangement after sample preparation and **B** at t_1 based on the initial configuration in A.

substrate direction, is often observed - likely due to an increased overlap between molecular and substrate states [67, 213–215]. Here, such an increased overlap would benefit the observed hot hole transfer across the interface at t_1. Although the increased molecule-substrate interaction in B would motivate a rotation of $CuPc^+$ molecules, it fails to explain why also $CuPc^0$ molecules rotate. Furthermore the question remains, why all $CuPc^+$ molecules rotate in anti-clockwise direction (green arrow in B) when a rotation in clockwise direction (purple arrow) would similarily lead to an increased overlap between molecular and substrate states.

Intermolecular Interactions

'Pair potential' calculations [216] present a way to predict in-plane orientations of molecules relative to their unit cell in 2D films. Thereby, the potential energy landscape of a molecular film is modeled by calculating van-der-Waals and electrostatic interactions between the atomic sites of neighboring molecules. Depending on the unit cell size or intermolecular distance $\mathbf{a}_1 = \mathbf{a}_2 = \mathbf{a}$, in-plane orientations of molecules are found for which the potential is minimized. Interactions with a substrate are neglected in these calculations. Even though previous studies on CuPc adsorbed on metals have shown that molecule-substrate interactions can mediate a repulsive interaction between neighbording adsorbates [67], the pair potential approach could adequately model the molecular in-plane orientations for this case and also for other chemisorbed systems [190, 216].

M. Reuner has performed such a pair potential calculation for this work in order to compare the potential energy landscapes in the molecular films at t_{-1} and t_1. Thereby, the sample

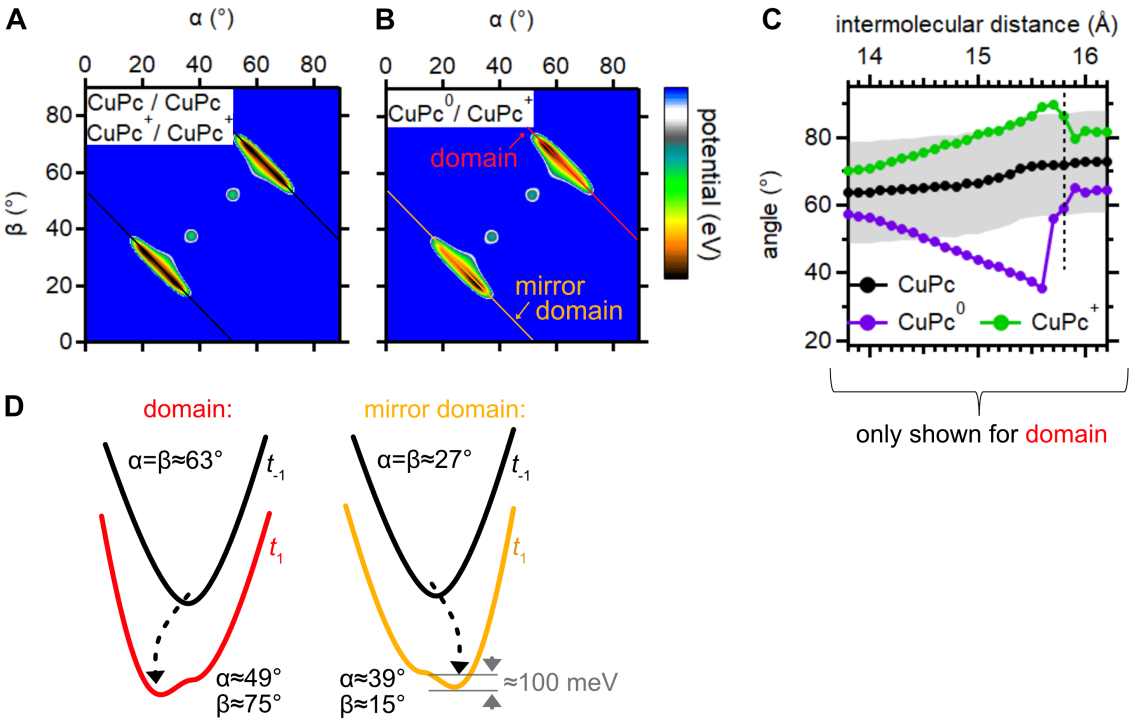

Figure 4.21: Pair potential calculations for a cluster of 5 CuPc molecules. Pair potential calculation for **A** a cluster of neutral CuPc molecules or a cluster of $CuPc^+$ molecules and **B** for a checkerboard arrangement of $CuPc^+$ and $CuPc^0$ molecules. In A and B the molecules are arranged at a fixed distance of $\mathbf{a}_1 = \mathbf{a}_2 = \mathbf{a} = 13.8$ Å. **C** Angles of CuPc, $CuPc^0$ and $CuPc^+$ leading to a minimized potential interface for varying **a**. **D** Sketched linecuts along the colored lines in A and B revealing an opposite rotation of $CuPc^+$ and $CuPc^0$ at t_1, while the direction of rotation is switched in mirror domains.

is modeled by a cluster of five CuPc molecules: a central CuPc molecule is laterally surrounded by its four nearest neighbors which are arranged in nearly-quadratic unit cells as deduced from the LEED measurement. Since the actual unit cell vector length could not be measured during the experiment, a series of calculations were performed for intermolecular distances ranging from 13.8 Å to 16.2 Å corresponding coverages between 1 and 0.85 monolayers. To determine the optimal in-plane orientation of the molecules, angles α and β are defined that refer to the angle between the CuPc wing and the unit cell vector $\mathbf{a}_1$ as marked in Fig. 4.20 B. Thereby, α describes the in-plane orientation of the central molecule and β the orientations of the surrounding molecules. α and β are then varied from 0° to 90° in increments of 1° while keeping the intermolecular distance fixed. For each configuration, the system's potential energy is calculated and finally the angles leading to a minimized potential are evaluated.

Two of such pair potential maps are shown in Fig. 4.21 A and B for a fixed intermolecular distance of 13.8 Å. At t_{-1} (A), the cluster is comprised of neutral CuPc molecules and potential minima are obtained for which α and β take the same value. At an intermolecular

distance of 13.8 Å two equal global minima are found at $\alpha = \beta = 63°$ and $\alpha = \beta = 27°$. The pair of global minima can be viewed as two complimentary molecular arrangements: one is corresponding to the molecular orientation in the domain and the other to the mirror domain. With increasing intermolecular distance the position of the global minimum in a domain shifts - the dependency is shown in Fig. 4.21 C. Thereby, the black markers indicate the value of $\alpha = \beta$ in the cluster of CuPc molecules with equal charge. Note, that for a cluster consisting of only $CuPc^+$ molecules the same angles are found as in the neutral film (see A). While an in-plane angle of 63° is preferred at monolayer coverage, angles of up to 74° are assumed for coverages down to 0.85 monolayers. This trend visualizes the repulsive interaction between CuPc molecules and provides molecular orientations for which the average interatomic distances in neighboring molecules can be maximized.

At t_1, the cluster no longer consists of neutral molecules, instead a checkerboard pattern of $CuPc^0$/$CuPc^+$ molecules is assumed in which the central molecule has neutral charge and its neighbors are of positive charge. For the $CuPc^+$ molecules, partial charges are assigned to each atom based on the charge distribution obtained from the calculation of relaxed, isolated $CuPc^+$ (discussed in section 4.2.2.2). Van-der-Waals parameters are taken from [216]. The pair potential map of this checkerboard pattern is shown in Fig. 4.21 B. Two equal global potential minima are obtained for which α and β take values different from each other. Hence, two energetically equivalent molecular arrangements are expected to form at t_1 and in both arrangements $CuPc^0$ and $CuPc^+$ molecules are rotated against one another.

For better illustration of the shifting potential minima, linecuts are sketched in Fig. 4.21 D with corresponding colors to the directions marked in A and B. At t_{-1}, the potentials in the domain and mirror domain (black) are symmetric with respect to the bisector. At t_1, the potentials become asymmetric and are biased towards opposite sides of the bisector for the domain and mirror domain. In the domains (red) $CuPc^0$ appears to be rotated by -14° and $CuPc^+$ by +12°. In the mirror domains (yellow) the opposite is observed: $CuPc^0$ molecules rotate by +14° and $CuPc^+$ by -12°. This reversed direction of rotation in mirror domains is suggested by all studied models with varying intermolecular distance.

Further, the magnitude of the relative rotation between $CuPc^0$ and $CuPc^+$ molecules appears to be determined by their distance **a**. The angles of $CuPc^0$ and $CuPc^+$ in the domain are shown in Fig. 4.21 C by purple and green markers, respectively. An increase of the relative rotation magnitude is observed for **a** increasing up to ~ 15.5 Å. This can be understood when considering that the rotation of molecules is sterically hindered in a densely packed film. For values of **a** larger than 15.5 Å, the magnitude of the rotations decrease again as interactive forces continue to decrease in less densely packed films.

Based on the qualitative agreement between the experiment and the findings from the pair potential calculations, it appears plausible to attribute the relative rotations in $CuPc^0$ and

$CuPc^+$ observed in the experiment to altered electrostatic interactions within the molecular film after hot hole transfer from the substrate. The pair potential calculations can also offer an explanation for the question why (40 ± 5) % of $CuPc^0$ appear not to rotate at t_1: Figs. 4.21 A and B imply that a relative rotation is only observed if $CuPc^0$ and $CuPc^+$ molecules are placed adjacent to one another. In the case of a clustered arrangement of only $CuPc^0$ or $CuPc^+$ molecules no rotation is expected. Hence, we infer that (60 ± 5) % of $CuPc^0$ molecules must be arranged adjacent to $CuPc^+$ molecules and do therefore rotate at t_1 while the remaining (40 ± 5) % is not. For $CuPc^+$ molecules, this number is more difficult to extract from the experimental data in Fig. 4.18 C since the momentum distribution is inseparable from signatures of $CuPc^0$ molecules (see Fig. 4.18 A). In consequence to the findings of the pair potential calculations although, it is expected that the same amount of $CuPc^+$ molecules rotate as $CuPc^0$ molecules do. A pie chart summarizing the numbers of rotating and non-rotating $CuPc^0$ and $CuPc^+$ molecules is shown in Fig. 4.22.

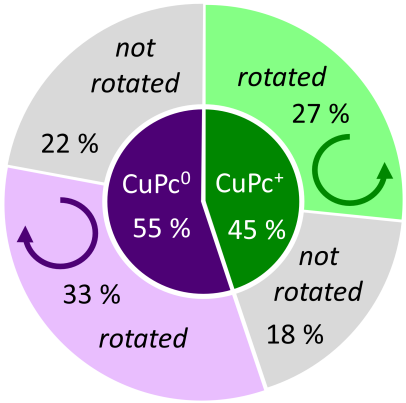

Figure 4.22: Quantitative Summary of Rotating Molecules. Representation of the quantitative numbers of rotating and non-rotating $CuPc^0$ (purple) and $CuPc^+$ (green) molecules evaluated from tr-XPD measurements and pair potential calculations.

In order to quantitatively compare the pair potential findings with the experiment, it needs to be addressed that the angle $\alpha = \beta = 45°$ of the molecular arrangement in Fig. 4.20 A is not reproduced by the pair potential calculation (see Fig. 4.21 C, black markers). The calculation predicts rotations of $CuPc^0$/$CuPc^+$ molecules only for initial in-plane angles larger than 60°. Moreover, rotations with values close to $\pm$ 15° are expected for two initial angles at 63° and 75°, which correspond to arrangements at intermolecular distances of $\mathbf{a} = 14.5$ Å and $\mathbf{a} = 15.8$ Å respectively. This is visualized in Fig. 4.21 C by the positions at which the purple and green markers meet the border of the area shaded in grey around the black markers. From the relative positioning of substrate and HOMO features in momentum space at t_{-1} (Fig. 4.2.1 H) an initial angle of 63° can be definitely excluded for this experiment. The initial angle of 75° although would be experimentally indistinguishable from the 45° ar-

rangement shown in Fig. 4.20 A due to the twelve-fold symmetry in the HOMO momentum distribution. Below, it will be argued why the molecular arrangements in Fig. 4.24 A and B have likely been present during the experiment at t_{-1} and t_1, respectively.

Unidirectionality of the Rotation

Lastly, the question remains why only one direction of rotation is observed for $CuPc^0$ and $CuPc^+$ molecules each. The LEED measurement taken of the sample after preparation reveals the existence of, both, domains and mirror domains. From the pair potential calculations reversed directions of rotation are predicted for $CuPc^0$/$CuPc^+$ in domains and mirror domains (see Fig. 4.23 A). During the experiment although, only one direction of rotation is observed: $CuPc^+$ rotate by $+(15 \pm 3)^\circ$ and $CuPc^0$ rotate by $-(15 \pm 3)^\circ$ at t_1. Because the direction of rotation is tied to the molecular arrangement in domains and mirror domains, it is suspected that a reordering of the molecular film must have taken place during the experiment leading to the absence of mirror domains (Fig. 4.23 B). This absence would allow for assuming Fig. 4.24 A without its mirror domain as the molecular arrangement present at t_{-1}.

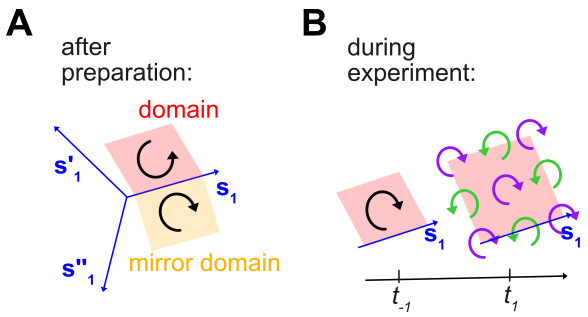

Figure 4.23: Substrate imposed organizational chirality in the molecular film. Sketch of molecular arrangements **A** after sample preparation and **B** during the experiment. Black arrows indicate the organizational chirality per domain and shouldn't be confused with the direction of rotation of individual molecules (purple, green arrows).

The mirror domain to a domain is constructed by mirroring the molecular unit cell at the substrate high symmetry direction $\mathbf{s}_1$ (see Fig. 4.23 A). Both are energetically equivalent, thus why should only one be experimentally observed? The formation of a perfectly quadratic unit cell could explain this: in this case unit cells of mirror domains would equal those of domains. In a LEED experiment, this would be then observable as the absence of additional reflexes originating from mirror domains. Quadratic unit cells have been reported for FePc/Ag(111) [189] before. In this work, the unit cell evaluated from LEED is almost quadratic with $\mathbf{a}_1 = \mathbf{a}_2$ enclosing an angle of 94°. It seems plausible that a quadratic

unit cell could have formed after recurrently charging the molecular film in the pump-probe experiment. Electrostatic forces imposed to mobile adsorbates by STM tips have shown to trigger lateral movements in the adsorbates by up to $\sim 60\,\mathrm{nm}$ [217]. Here, a lateral movement of less than 1 nm would be needed to create a quadratic molecular unit cell. There is a downfall to this consideration though: the condition for domains equalling mirror domains is only met if also the molecular in-plane orientations match. This would be the case for the initial angle $\alpha = \beta = 45°$ shown for the molecular arrangement in Fig. 4.20 A. It would not be supported by the arrangement in Fig. 4.24 A which is derived from the pair potential calculations.

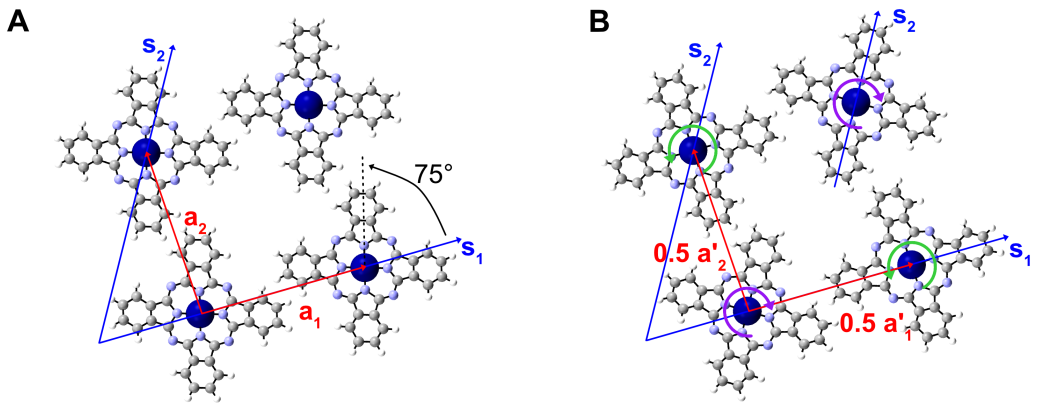

Figure 4.24: Molecular arrangements derived from the pair potential calculations and assuming organizational homochirality. Assumed molecular arrangements at **A** t_{-1} and **B** t_1.

Macroscopic Rearrangement of the Molecular Film?

An alternative explanation can be found in literature on the topic of chirality in molecular ensembles. External stimuli such as light, thermal and electrical energy have been discussed to not only trigger lateral and switching motions in single molecules [2] but also to induce large-scale molecular rearrangements. Driven by the goal to minimize the interfacial potential energy, these rearrangements often result in the creation of so-called 'homochirality'.

Prior to defining homochirality, a few termini regarding chirality will be introduced briefly: chirality can be seen as an intrinsic property to a single molecule where it is predefined by its atomic structure. The chiral molecule exists in a second form with mirrored atomic structure – both forming a pair of non-superimposable 'enantiomers'. Also achiral molecules (such as CuPc) can become chiral upon adsorption: when placed on a substrate with mismatched

symmetry (such as $TiSe_2$), the interactive strength with the substrate may be inhomogeneous at different molecular sites. As a result, asymmetric molecular distortions [218, 219] or asymmetric charge transfer [190, 220] can occur that have shown to impose a chirality to the molecule. In systems where achiral molecules and the substrate interact weakly, a macroscopic form of chirality has been discussed – a so-called 'organizational chirality' [221–224]. Organizational chirality emerges from the relative arrangement of molecules in a molecular film and is present here in the form of domains and mirror domains (black arrows in Fig. 4.23 B) which represent an enantiomeric pair of opposite handedness. After sample preparation, the domain and mirror domain exist in equal amounts and the sample is on average achiral. Over the course of the measurement duration, 'homochirality' – the overall existence of domains of only one handedness – appears to have formed in this work.

Creating homochirality is of important interest to current research: while the enantiomers share many physical properties they can be of different function in nature as biological processes are often enantiospecific. Also, concepts on molecule-based information storage devices rely on chirality-switching of large-scale molecular domains [225]. To fabricate such devices and to control their function it is crucial to understand how and why homochiral samples form. In the past three decades, many efforts have been put forward in this direction, valuable reviews are provided by Ernst [226] and Sallembien et al. [227]. While several individual concepts have been proposed with explanations varying from case to case, two main principles have been established that describe the creation of homochirality in a molecular film: the 'seargents-and-soldiers' [221, 228, 229] and the 'majority rules' [230–233] principle.

Both principles rely on the interchangeability between the two enantiomers, which are initially present in the sample. Here, this would mean that the lateral arrangement of molecules is altered such that domains transform into their mirror domains or vice versa. While the seargents-and-soldiers principle relies on skewing the interchangeability in an assembly of achiral molecules ('soldiers') by adding a few chiral molecules ('seargents'), the amplification of an initial enantiomeric imbalance creates homochirality in the majority rules principle. For the latter, Oswald ripening [220], entropy considerations [231] or energy optimizations at domain boundaries [230] have been discussed to drive the amplification.

In the case studied here, the 'majority rules' principle is considered to apply. While the sample may be globally achiral after sample preparation, a slight imbalance between domains and mirror domains is likely present within the illuminated part of the sample. This initial imbalance is then amplified during the pump-probe measurement by interconversion of the minority domain into the majority (mirror) domain. This interconversion would require lateral movements of molecules by < 2 nm and molecular rotations by 0° and by 30° for the configurations in Fig. 4.20 A and in Fig. 4.24 A, respectively. Sources that could aid

to overcome the potential barrier between domain and mirror domain are the local heating of the sample by the laser pulses, the structural changes in $CuPc^+$ and the long-range potential modulation at the CuPc/$TiSe_2$ interface [229, 233, 234].

The exact mechanism as well as time-scale for this interconversion is unknown and not accessible with the present measurement techniques. Future developments towards imaging macroscopic molecular arrangements on sub-picosecond time-scales, e.g. by time-resolved LEED, may provide a means to provide further insight. Yet, it can be stated that in the present data averaging over several hours measurement time no signature of the minority enantiomer (mirror domain) is traced - assuming the pair potential predictions to be valid. From the amount of molecules participating in the rotation at t_1 we would thus infer that at least (60 ± 5) % of the molecules were arranged in homochiral domains within the studied sample area.

With this, the question about the directional rotation in $CuPc^+$ and $CuPc^0$ is addressed and connected to the creation of organizational homochirality in large areas of the sample. Based on the conclusion that mirror domains are suppressed in the experiment, the molecular arrangements shown in Fig. 4.24 A and B can be assumed to describe the sample at t_{-1} and t_1, respectively. These arrangements would agree with the experimental observations in the valence and core level data and allow for explaining the observed molecular rotations with the pair potential model.

4.2.3 Summary

With our study on the CuPc/$TiSe_2$ interface we provide a suitable platform for visualizing and disentangling the dynamic interplay of electronic motion and structural rearrangement at hybrid interfaces in response to light excitation. Unique to the specific material combination at hand, we discover an ultrafast concerted gearing motion within the molecular layer that is driven by the flow of charge and energy across the hybrid interface. In our experiment we integrate three modalities of time-resolved photoemission spectroscopy – tr-ARPES, tr-XPS and tr-XPD – in a single setup and detect the emission from interfacial valence states and core levels with a time-of-flight momentum microscope. This combined approach allows us to access dynamic electronic and structural information with femtosecond and sub-Ångstroem resolution and to record an 'interfacial movie', i.e., imaging atomic positions and molecular orbital wavefunctions in reciprocal space simultaneously with the population of electronic states in energy-momentum space as bonds and bands are rearranging in time.

Upon optical excitation we trace the transfer of spectral weight from the substrate's Se $4p$ valence band into the Ti $3d$ conduction band. Immediately afterwards hot electrons and hot holes start to relax by scattering towards E_F. The CuPc adsorbates are involved in this relaxation pathway: in ~ 1 % of the molecules the LUMO becomes populated by hot electrons scattering across the interface and the HOMO of (45 ± 2) % of the molecules is filled by hot holes originating from the substrate. The amount of molecules becoming positively charged is surprisingly large and – to my knowledge – such charge carrier transfer magnitudes have not been observed in other pump-probe experiments yet. The high charge carrier transfer efficiency at the CuPc/$TiSe_2$ interface is attributed to the 2D-like nature of $TiSe_2$ in combination with the energetic location of the CuPc HOMO close to E_F. As a consequence of charging a significant fraction of the adsorbed molecules the interfacial electronic and structural properties are significantly altered: on a molecular scale, we observe in-plane as well as out-of-plane deformations in the charged $CuPc^+$ molecules. On a macroscopic scale, the 'supercharging' evokes a surface potential modulation which leads to energetic shifts in substrate and adsorbate states on the order of ~ 200 meV. Simultaneously, the macroscopic molecular arrangement adopts to the new potential surface (see Fig. 4.25): $CuPc^0$ and $CuPc^+$ molecules perform gearing motions with relative in-plane rotations by $\pm(15 \pm 3)^\circ$ within 375 fs after excitation. The chemical specificity of our experiment allows us to separately trace the rotations in $CuPc^0$ and $CuPc^+$ molecules which are always of opposite sign. We can explain these opposite rotations by means of pair potential calculations and connect them to altered electrostatic forces between $CuPc^0$ and $CuPc^+$ species in the charged film. After sample preparation, at least six domains (3 domains, 3 mirror domains) are present within the sample. Based on the pair potential calculations molecules are expected to re-

verse their rotation in mirror domains. This is inconsistent with the experiment - we observe only one direction of rotation per species. We therefor assume that a structural rearrangement of the molecular film has taken place during the pump-probe experiment resulting in the suppression of mirror domains. Inducing and imaging such a concerted rotation on a micrometer length scale is a novelty to research and may improve our understanding on creating function in molecule based devices.

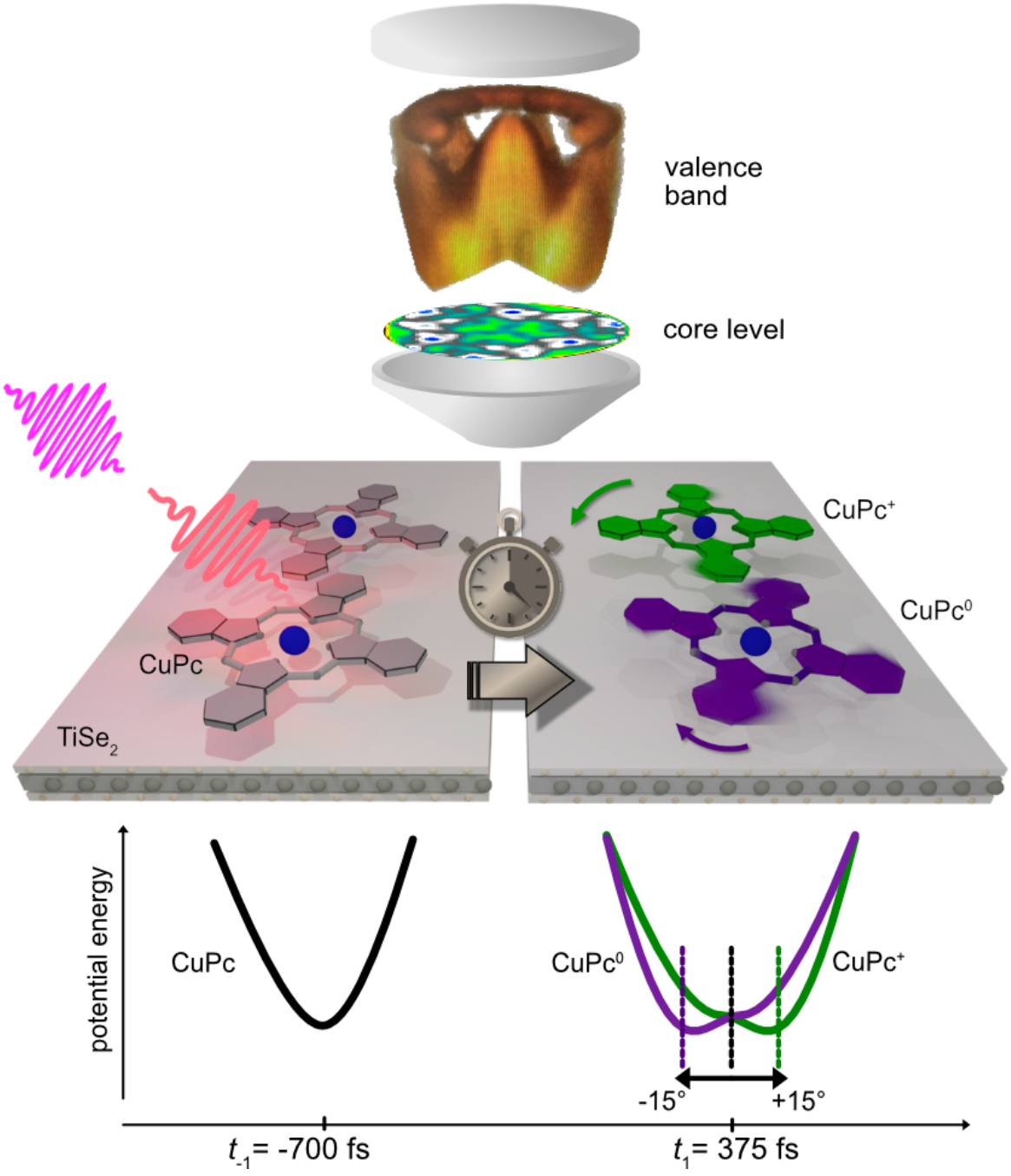

Figure 4.25: Gearing motion in $CuPc^0$ and $CuPc^+$ induced by the surface potential modulation. Excitation induced charge transfer between CuPc and $TiSe_2$ leads to a surface potential modulation and rotation of $CuPc^0$ and $CuPc^+$ molecules by -15° and +15°, respectively. This concerted rotation occurs on a sub-picosecond time-scale and on a length-scale of several hundreds of micrometers.

5 Conclusion and Outlook

In the late 19th century snapshot photography was introduced as a way to study processes that are too fast for our eyes to follow. With his famous picture series of a galopping horse taken with millisecond resolution, E. Muybridge set out to answer the question whether there was a point in time when all four feet of the horse were simultaneously lifted from the ground [235]. What initially started as a scientific endeavor of little interest to the masses was soon integrated in our every-day-life in the form of cinematography. Today, snapshot photography has evolved and the dynamics we are interested in have become orders of magnitude faster as well as smaller. Although one might doubt that a film about atoms or electrons in motion will sell out cinemas in the near future, I believe that the insight gained from molecular movies will enable us to understand ultrafast processes and help to eventually design future devices with faster and smaller functionality.

As the goal of this thesis, such an ultrafast movie was shot for two selected hybrid organic/inorganic interfaces with sub-picosecond and sub-Ångström resolutions. The obtained transient images could shed light on how the flow of charge and energy across the hybrid interface is interconnected to its electronic and atomic structure. The experiments were conducted at a HHG source and at the free-electron-laser *FLASH* (Hamburg, Germany). The tunable excitation energies provided by *FLASH* allowed for accessing information on both the interfacial valence band and core level dynamics of the studied samples in a single setup. By means of a time-of-flight momentum microscope, signatures from substrate and molecular states could be disentangled and separately traced in time. The comparison of their transient population and distribution in momentum space revealed a complex interplay between electronic and atomic structure of the hybrid components upon light excitation. For the CuPc/$TiSe_2$ interface it was found that after excitation of hot charge carriers in the substrate a significant fraction (45 %) of the adsorbed CuPc molecules becomes positively charged by interfacial hot hole scattering. This 'supercharging' triggers a series of events: beginning with a modification of the surface potential, the global electronic structure of the interface appears shifted, charged CuPc molecules are bent (mainly) in out-of-plane direction and the lateral arrangement in 60 % of all adsorbates is altered. In this macroscopic ensemble of molecules, unidirectional in-plane rotations by +15° and -15° are observed for neutral and charged CuPc molecules, respectively. This concerted rotation is reversible and is repeatedly initiated by supercharging the molecular film. With our approach on shooting an interfacial movie by means of surface-integrating measurement techniques we were the

first to detect such a macroscopic structural rearrangement occurring on a sub-picosecond time scale.

Conducting such FEL-based time-resolved studies is challenging. It requires the combined efforts from many experimentalists while on-site and from theorists during the stage of data evaluation. In order to estimate whether our findings are universal and whether the performed approach is applicable to other material systems, we need the confimation from many more studies. As of today, on-going efforts are made towards making FEL science more accessible and versatile. On the experimental side, a new generation of FELs is being built at *FLASH*, at the *European EuXFEL* (Schenefeld, Germany) and at *LCLS-II* (Stanford, USA). By implementing upgrades on both the repetition rate and performance, more beamtime will be available for user experiments. Photon pulses will be of variable polarization and *FLASH* will slightly increase its photon energy range to cover energy resonances in the water window for energy research. With this progress being made, hopefully new techniques, such as time-resolved LEED (tr-LEED), time-resolved x-ray standing waves measurements (tr-XSW) or time- and spin-resolved PES, will also become established at FELs. By means of tr-LEED and tr-XSW, macroscopic information on the sample's lateral and vertical structure could be transiently accessed – information valuable for tracing macroscopic dynamics such as the switching motion at the CuPc/$TiSe_2$ interface. Including spin-selectivity to trPES will not only allow for tracing the dynamics of processes such as singlet fission or intersystem crossing but also for shooting 'complete interfacial movies' including the parameters energy, momentum, spin and time. The growing demand and new possibilities of time-resolved techniques will hopefully also motivate the development of new theoretical approaches towards describing excited state dynamics on a femto- to picosecond time scale. Currently, such dynamic calculations are computationally not feasible for large models such as excited hybrid interfaces. Instead, the dynamics are explained – as for this thesis – by static models at selected time-frames. With these both experimental and theoretical future developments we may soon establish 'ultrafast interfacial movies' as a new tool for understanding and manipulating device function.

Danksagung

Marina Keegan schreibt in ihrem Abschlussessay für die Yale Daily News: "We don't have a word for the opposite of loneliness, but if we did, I could say that's what I want in life. What I'm grateful and thankful to have found at Yale, and what I'm scared of losing when we [...] leave this place. [...] it's just this feeling that there are people, an abundance of people, who are in this together. Who are on your team."

Ein ganz ähnliches Gefühl verspüre ich jetzt, nachdem sich fünf Jahre Studium und fünf Jahre Doktorarbeit hier in Würzburg einem Ende neigen. Ich möchte mich an dieser Stelle bei all denjenigen bedanken, die mich auf dem Weg zum Abschluss dieser Arbeit begleitet haben und mir das Gefühl des "Gegenteils von Einsamkeit" vermittelt haben.

An erster Stelle gilt mein Dank meinem Doktorvater Friedel Reinert. Danke, dass du mir ermöglicht hast ein Teil der EP7 zu sein und dass du mir die Freiheit und Zeit gegeben hast meine eigenen Interessen in der Forschung zu entwickeln und ihnen nachzugehen! Danke auch dafür, dass du mich gleich zu Beginn meiner Doktorarbeit dabei unterstützt hast mich auf die Summerschool in Lund (Schweden) zu bewerben; und später an Messzeiten bei Diamond (UK), Soleil (Frankreich), DESY (Hamburg) und in Chiba (Japan) teilzunehmen. Bei den Aufenthalten durfte ich nicht nur einen Einblick in die Welt der Forschung gewinnen und Begegnungen mit vielen Menschen machen, die sich für ähnliche Interessen begeistern, sondern ich konnte auch wunderbare Orte bereisen (und deiner schier unmöglichen Herausforderung nachgehen in Nikko alle Statuen mit roten Hüten zu zählen)! Danke für das jährliche Aufstellen der EP7-Weihnachtsband! :)

Besonders möchte ich mich bei Markus Scholz bedanken, der mich seit meinem ersten Besuch am DESY betreut hat und mich für die Forschung am FEL begeistert hat. Danke, dass du mit mir dein Wissen über Zeitauflösung, die Abläufe bei *FLASH*, das Auswerten mit Python ;), das Schreiben von Papern und über vieles mehr geteilt hast! Danke für die vielen Zoom Sessions während der Corona Lockdown Phase, die teilweise bis in die Nacht dauerten, und die gute Zusammenarbeit!

Auch Christian Metzger möchte ich besonders danken. Nicht nur für deine Betreuung, dass du mich im Labor eingelernt hast und mich auch während frustrierenden Zeiten der Auswertung immer wieder motiviert hast, sondern vor allem für deine Freundschaft. Ohne dich wären die langen Stunden im Büro, die Nachtschichten auf Messzeit und die vielen Reisen sicherlich langweilig gewesen.

Mein Dank gilt außerdem meinen Kollegen, nur mit deren Unterstützung und Zusammenarbeit diese Arbeit in dieser Form entstehen konnte: Nils Wind, Michael Heber und

Dima Kutnyakhov, die mir bei den Experimenten im HHG-Labor und bei *FLASH* zur Seite standen; Lukas Wenthaus, Federico Pressacco, Chul-Hee Min, Thiago Peixoto und das restliche Team von *FLASH* und *EuXFEL*, mit denen ich viele Tage und Nächte während den Strahlzeiten bei *FLASH* gearbeitet, geknobelt und Gummibärchen gegessen habe; Kai Roßnagel für die vielen Diskussionen per Zoom und die Unterstützung beim Paperschreiben; Marvin Reuner, Daria Popova-Gorelova, Kaori Niki, Misa Nozaki und Masato Haniuda für die theoretische Unterstützung bei der Datenauswertung, viele bereichernde Diskussionen über Physik aber auch über Interkulturelles und für die gemeinsamen monatelangen Anstrengungen Reviewer- und Editorbriefe zu beantworten; Tim Wehling für seine eingängliche Erklärung zum Thema Elektrostatik.

Außerdem möchte ich meinen Kollegen an der EP7 für die schöne Atmosphäre an unserem Lehrstuhl danken. Ich denke gerne an die Kaffeepausen, das gemeinsame Mittagessen, die Joghurt-Blindverkostung, die Ausflüge zum Pole Dancing und zum Crossfit und das Literaturseminar in Thüringen zurück! Danke an Martin Graus, Manuel Grimm, Raphael Vidal, Julia Issing, Philipp Kagerer, Hendrik Bostelmann-Arp, Sonja Schatz, Katharina Kißner, Max Ünzelmann, Tim Figgemeier, Simon Müller, Celso Fornari, Hibiki Orio, Johannes Heßdörfer, Hendrik Bentmann, Peter Kastenhofer und an meine Bacheloranden Dominik Krauße, Christopher Reiser und Cornelius Boeckhoff für die schöne Zeit!

Ich möchte diese Gelegenheit weiterhin nutzen, um auch denjenigen zu danken, die mich während meines Studiums hier in Würzburg unterstützt und begleitet haben:

Ich habe meine Bachelor- sowie Masterarbeit am Lehrstuhl EP6 bei Jens Pflaum geschrieben mit Betreuung von Alexander Steeger und Florian Hüwe. Ich möchte euch danken, dafür, dass ihr mir so viel Freude an der Wissenschaft und dem Wissenschaftsumfeld vermittelt habt! Ich denke dabei besonders gerne an die wöchentlichen Lehrstuhldiskussionen mit Frühstücksei und Kickerturnier zurück, mein erster Besuch auf der DPG Frühjahrstagung in Dresden und die Escape Room Herausforderungen. Ich freue mich jedes mal in eurem Gemeinschaftsraum bekannte Gesichter wiederzusehen.

Auch meinen Freunden, die mich in Würzburg begleitet haben, gilt besonderer Dank:

Jan Hajer, Kathi Wimmer, Johannes Beierlein, Matthias Hartl und Willi Mantei – wir haben uns während den Ersti-Tagen kennengelernt, bei dem Versuch ein Ei unbeschadet aus dem ersten Stock fallen zu lassen. Seitdem sind wir als "Nanos" zusammengeblieben und haben es durchs Studium geschafft, haben unzählige Stunden in der Domerschulstraße verbracht und waren sogar ein Jahr in Berkeley. Ich bin froh, euch als meine Freunde zur Seite zu haben!

Julia Issing – ich bin froh eine Freundin wie dich gefunden zu haben, mit der man sowohl im Labor als auch außerhalb durch Dick und Dünn gehen kann!

Raphael Vidal – danke dir für die guten Gespräche auf den langen Wanderungen! Und die Reise nach Crimlak ;)

Paul Hoppstock – danke für deine wöchentlichen Mittwochabend Besuche :)!

Mein größter Dank gilt meiner Familie: meinen Eltern Sepideh und Reiner, meinem Bruder Arvid, meinem Freund Bernhard und meinen Großeltern Mimi und Apa – ihr habt immer an mich geglaubt, seid mir mit viel Liebe (und manchmal einem Glas frischem Orangensaft) während langen Abenden am Schreibtisch zur Seite gestanden und habt mit mir gelacht und geweint. Danke für eure Liebe!

Bibliography

[1] T. Kudernac, N. Ruangsupapichat, M. Parschau, B. Maciá, N. Katsonis, S. R. Harutyunyan, K.-H. Ernst, and B. L. Feringa, "Electrically driven directional motion of a four-wheeled molecule on a metal surface", Nature **479**, 208–211 (2011).

[2] D. Peller, L. Z. Kastner, T. Buchner, C. Roelcke, F. Albrecht, N. Moll, R. Huber, and J. Repp, "Sub-cycle atomic-scale forces coherently control a single-molecule switch", Nature **585**, 58–62 (2020).

[3] C. Pei and J. Gong, "Tandem catalysis at nanoscale", Science **371**, 1203–1204 (2021).

[4] M. Heber, N. Wind, D. Kutnyakhov, F. Pressacco, T. Arion, F. Roth, W. Eberhardt, and K. Rossnagel, "Multispectral time-resolved energy–momentum microscopy using high-harmonic extreme ultraviolet radiation", Review of Scientific Instruments **93**, 083905 (2022).

[5] K. Tiedtke, A. Azima, N. von Bargen, L. Bittner, S. Bonfigt, S. Düsterer, B. Faatz, U. Frühling, M. Gensch, C. Gerth, N. Guerassimova, U. Hahn, T. Hans, M. Hesse, K. Honkavaar, U. Jastrow, P. Juranic, S. Kapitzki, B. Keitel, T. Kracht, M. Kuhlmann, W. B. Li, M. Martins, T. Núñez, E. Plönjes, H. Redlin, E. L. Saldin, E. A. Schneidmiller, J. R. Schneider, S. Schreiber, N. Stojanovic, F. Tavella, S. Toleikis, R. Treusch, H. Weigelt, M. Wellhöfer, H. Wabnitz, M. V. Yurkov, and J. Feldhaus, "The soft x-ray free-electron laser FLASH at DESY: beamlines, diagnostics and end-stations", New Journal of Physics **11**, 023029 (2009).

[6] D. Kutnyakhov, R. P. Xian, M. Dendzik, M. Heber, F. Pressacco, S. Y. Agustsson, L. Wenthaus, H. Meyer, S. Gieschen, G. Mercurio, A. Benz, K. Bühlman, S. Däster, R. Gort, D. Curcio, K. Volckaert, M. Bianchi, C. Sanders, J. A. Miwa, S. Ulstrup, A. Oelsner, C. Tusche, Y.-J. Chen, D. Vasilyev, K. Medjanik, G. Brenner, S. Dziarzhytski, H. Redlin, B. Manschwetus, S. Dong, J. Hauer, L. Rettig, F. Diekmann, K. Rossnagel, J. Demsar, H.-J. Elmers, P. Hofmann, R. Ernstorfer, G. Schönhense, Y. Acremann, and W. Wurth, "Time- and momentum-resolved photoemission studies using time-of-flight momentum microscopy at a free-electron laser", Review of Scientific Instruments **91**, 013109 (2020).

[7] H. Kroemer, "Quasi-electric fields and band offsets: teaching electrons new tricks.", Nobel Lecture (2000).

[8] N. Koch, "Organic Electronic Devices and Their Functional Interfaces", ChemPhysChem **8**, 1438–1455 (2007).

[9] H. Ishii, K. Sugiyama, E. Ito, and K. Seki, "Energy level alignment and interfacial electronic structures at organic/metal and organic/organic interfaces", Advanced Materials **11**, 605–625 (1999).

[10] X.-Y. Zhu, "Charge Transport at Metal-Molecule Interfaces: A Spectroscopic View", The Journal of Physical Chemistry B **108**, 8778–8793 (2004).

[11] C. Dimitrakopoulos and P. Malenfant, "Organic thin film transistors for large area electronics", Advanced Materials **14**, 99–117 (2002).

[12] S. Braun, W. R. Salaneck, and M. Fahlman, "Energy-Level Alignment at Organic/Metal and Organic/Organic Interfaces", Advanced Materials **21**, 1450–1472 (2009).

[13] E. Goiri, P. Borghetti, A. El-Sayed, J. E. Ortega, and D. G. de Oteyza, "Multicomponent organic layers on metal substrates", Advanced Materials **28**, 1340–1368 (2015).

[14] S. Reineke, F. Lindner, G. Schwartz, N. Seidler, K. Walzer, B. Lüssem, and K. Leo, "White organic light-emitting diodes with fluorescent tube efficiency", Nature **459**, 234–238 (2009).

[15] M. Małachowski and J. Żmija, "Organic field-effect transistors", Opto-Electronics Review **18**, 121–136 (2010).

[16] F. Raymo, "Digital processing and communication with molecular switches", Advanced Materials **14**, 401–414 (2002).

[17] S. Kassem, T. van Leeuwen, A. S. Lubbe, M. R. Wilson, B. L. Feringa, and D. A. Leigh, "Artificial molecular motors", Chemical Society Reviews **46**, 2592–2621 (2017).

[18] C. Stadler, S. Hansen, I. Kröger, C. Kumpf, and E. Umbach, "Tuning intermolecular interaction in long-range-ordered submonolayer organic films", Nature Physics **5**, 153–158 (2009).

[19] H. Wang, W. Liu, X. He, P. Zhang, X. Zhang, and Y. Xie, "An excitonic perspective on low-dimensional semiconductors for photocatalysis", Journal of the American Chemical Society **142**, 14007–14022 (2020).

[20] R. J. D. Miller, "Femtosecond crystallography with ultrabright electrons and x-rays: capturing chemistry in action", Science **343**, 1108–1116 (2014).

[21] C. W. Nicholson, A. Lücke, W. G. Schmidt, M. Puppin, L. Rettig, R. Ernstorfer, and M. Wolf, "Beyond the molecular movie: dynamics of bands and bonds during a photoinduced phase transition", Science **362**, 821–825 (2018).

[22] R. Wallauer, M. Raths, K. Stallberg, L. Münster, D. Brandstetter, X. Yang, J. Güdde, P. Puschnig, S. Soubatch, C. Kumpf, F. C. Bocquet, F. S. Tautz, and U. Höfer, "Tracing orbital images on ultrafast time scales", Science **371**, 1056–1059 (2021).

[23] S. Vogelgesang, G. Storeck, J. G. Horstmann, T. Diekmann, M. Sivis, S. Schramm, K. Rossnagel, S. Schäfer, and C. Ropers, "Phase ordering of charge density waves traced by ultrafast low-energy electron diffraction", Nature Physics **14**, 184–190 (2017).

[24] T. Frigge, B. Hafke, T. Witte, B. Krenzer, C. Streubühr, A. S. Syed, V. M. Trontl, I. Avigo, P. Zhou, M. Ligges, D. von der Linde, U. Bovensiepen, M. H. von Hoegen, S. Wippermann, A. Lücke, S. Sanna, U. Gerstmann, and W. G. Schmidt, "Optically excited structural transition in atomic wires on surfaces at the quantum limit", Nature **544**, 207–211 (2017).

[25] G. Sciaini and R. J. D. Miller, "Femtosecond electron diffraction: heralding the era of atomically resolved dynamics", Reports on Progress in Physics **74**, 096101 (2011).

[26] D. Curcio, S. Pakdel, K. Volckaert, J. A. Miwa, S. Ulstrup, N. Lanatà, M. Bianchi, D. Kutnyakhov, F. Pressacco, G. Brenner, S. Dziarzhytski, H. Redlin, S. Y. Agustsson, K. Medjanik, D. Vasilyev, H.-J. Elmers, G. Schönhense, C. Tusche, Y.-J. Chen, F. Speck, T. Seyller, K. Bühlmann, R. Gort, F. Diekmann, K. Rossnagel, Y. Acremann, J. Demsar, W. Wurth, D. Lizzit, L. Bignardi, P. Lacovig, S. Lizzit, C. E. Sanders, and P. Hofmann, "Ultrafast electronic linewidth broadening in the C 1*s* core level of graphene", Physical Review B **104**, l161104 (2021).

[27] S. Dong, M. Puppin, T. Pincelli, S. Beaulieu, D. Christiansen, H. Hübener, C. W. Nicholson, R. P. Xian, M. Dendzik, Y. Deng, Y. W. Windsor, M. Selig, E. Malic, A. Rubio, A. Knorr, M. Wolf, L. Rettig, and R. Ernstorfer, "Direct measurement of key exciton properties: energy, dynamics, and spatial distribution of the wave function", Natural Sciences **1**, e10010 (2021).

[28] T. Rohwer, S. Hellmann, M. Wiesenmayer, C. Sohrt, A. Stange, B. Slomski, A. Carr, Y. Liu, L. M. Avila, M. Kalläne, S. Mathias, L. Kipp, K. Rossnagel, and M. Bauer, "Collapse of long-range charge order tracked by time-resolved photoemission at high momenta", Nature **471**, 490–493 (2011).

[29] M. K. L. Man, J. Madéo, C. Sahoo, K. Xie, M. Campbell, V. Pareek, A. Karmakar, E. L. Wong, A. Al-Mahboob, N. S. Chan, D. R. Bacon, X. Zhu, M. M. M. Abdelrasoul, X. Li, T. F. Heinz, F. H. da Jornada, T. Cao, and K. M. Dani, "Experimental measurement of the intrinsic excitonic wave function", Science Advances **7**, 2375–2548 (2021).

[30] K. Baumgärtner, M. Reuner, C. Metzger, D. Kutnyakhov, M. Heber, F. Pressacco, C.-H. Min, T. R. F. Peixoto, M. Reiser, C. Kim, W. Lu, R. Shayduk, M. Izquierdo, G. Brenner, F. Roth, A. Schöll, S. Molodtsov, W. Wurth, F. Reinert, A. Madsen, D. Popova-Gorelova, and M. Scholz, "Ultrafast orbital tomography of a pentacene film using time-resolved momentum microscopy at a FEL", Nature Communications **13**, 2741 (2022).

[31] F. Roth, M. Borgwardt, L. Wenthaus, J. Mahl, S. Palutke, G. Brenner, G. Mercurio, S. Molodtsov, W. Wurth, O. Gessner, and W. Eberhardt, "Direct observation of charge separation in an organic light harvesting system by femtosecond time-resolved XPS", Nature Communications **12**, 1196 (2021).

[32] S. Hellmann, M. Beye, C. Sohrt, T. Rohwer, F. Sorgenfrei, H. Redlin, M. Kalläne, M. Marczynski-Bühlow, F. Hennies, M. Bauer, A. Föhlisch, L. Kipp, W. Wurth, and K. Rossnagel, "Ultrafast melting of a charge-density wave in the Mott insulator $1T$-TaS_2", Physical Review Letters **105**, 187401 (2010).

[33] J. Feldhaus, "FLASH—the first soft x-ray free electron laser (FEL) user facility", Journal of Physics B: Atomic, Molecular and Optical Physics **43**, 194002 (2010).

[34] N. Koch, "Electronic structure of interfaces with conjugated organic materials", physica status solidi (RRL) - Rapid Research Letters **6**, 277–293 (2012).

[35] X.-Y. Zhu, "Electronic structure and electron dynamics at molecule–metal interfaces: implications for molecule-based electronics", Surface Science Reports **56**, 1–83 (2004).

[36] J. E. Lennard-Jones, "The electronic structure of some diatomic molecules", Transactions of the Faraday Society **25**, 668 (1929).

[37] R. S. Mulliken, "Spectroscopy, Molecular Orbitals, and Chemical Bonding", Science **157**, 13–24 (1967).

[38] R. Otero, A. V. de Parga, and J. Gallego, "Electronic, structural and chemical effects of charge-transfer at organic/inorganic interfaces", Surface Science Reports **72**, 105–145 (2017).

[39] X. Crispin, V. Geskin, A. Crispin, J. Cornil, R. Lazzaroni, W. R. Salaneck, and J.-L. Brédas, "Characterization of the Interface Dipole at Organic/Metal Interfaces", Journal of the American Chemical Society **124**, 8131–8141 (2002).

[40] E. Zojer, T. C. Taucher, and O. T. Hofmann, "The impact of dipolar layers on the electronic properties of organic/inorganic hybrid interfaces", Advanced Materials Interfaces **6**, 1900581 (2019).

[41] H. Fukagawa, H. Yamane, S. Kera, K. K. Okudaira, and N. Ueno, "Experimental estimation of the electric dipole moment and polarizability of titanyl phthalocyanine using ultraviolet photoelectron spectroscopy", Physical Review B **73**, 041302 (2006).

[42] H. Fukagawa, S. Hosoumi, H. Yamane, S. Kera, and N. Ueno, "Dielectric properties of polar-phthalocyanine monolayer systems with repulsive dipole interaction", Physical Review B **83**, 085304 (2011).

[43] G. Greczynski, M. Fahlman, and W. Salaneck, "Electronic structure of hybrid interfaces of poly(9,9-dioctylfluorene)", Chemical Physics Letters **321**, 379–384 (2000).

[44] D. M. Newns, "Self-consistent model of hydrogen chemisorption", Physical Review **178**, 1123–1135 (1969).

[45] M. Wießner, J. Ziroff, F. Forster, M. Arita, K. Shimada, P. Puschnig, A. Schöll, and F. Reinert, "Substrate-mediated band-dispersion of adsorbate molecular states", Nature Communications **4**, 1514 (2013).

[46] M. Hollerer, D. Lüftner, P. Hurdax, T. Ules, S. Soubatch, F. S. Tautz, G. Koller, P. Puschnig, M. Sterrer, and M. G. Ramsey, "Charge transfer and orbital level alignment at inorganic/organic interfaces: the role of dielectric interlayers", ACS Nano **11**, 6252–6260 (2017).

[47] S. Emmerich, S. Hedwig, B. Arnoldi, J. Stöckl, F. Haag, R. Hemm, M. Cinchetti, S. Mathias, B. Stadtmüller, and M. Aeschlimann, "Ultrafast charge-transfer exciton dynamics in C_{60} thin films", The Journal of Physical Chemistry C **124**, 23579–23587 (2020).

[48] G. Zamborlini, D. Lüftner, Z. Feng, B. Kollmann, P. Puschnig, C. Dri, M. Panighel, G. D. Santo, A. Goldoni, G. Comelli, M. Jugovac, V. Feyer, and C. M. Schneider, "Multi-orbital charge transfer at highly oriented organic/metal interfaces", Nature Communications **8**, 335 (2017).

[49] S. Hüfner, *Photoelectron spectroscopy* (Springer Berlin Heidelberg, 1995).

[50] H. J. Wörner, C. A. Arrell, N. Banerji, A. Cannizzo, M. Chergui, A. K. Das, P. Hamm, U. Keller, P. M. Kraus, E. Liberatore, P. Lopez-Tarifa, M. Lucchini, M. Meuwly, C. Milne, J.-E. Moser, U. Rothlisberger, G. Smolentsev, J. Teuscher, J. A. van Bokhoven, and O. Wenger, "Charge migration and charge transfer in molecular systems", Structural Dynamics **4**, 061508 (2017).

[51] R. A. Marcus, "Electron transfer reactions in chemistry. Theory and experiment", Reviews of Modern Physics **65**, 599–610 (1993).

[52] J.-L. Brédas, D. Beljonne, V. Coropceanu, and J. Cornil, "Charge-Transfer and Energy-Transfer Processes in π-Conjugated Oligomers and Polymers: A Molecular Picture", Chemical Reviews **104**, 4971–5004 (2004).

[53] F. Flores, J. Ortega, and H. Vázquez, "Modelling energy level alignment at organic interfaces and density functional theory", Physical Chemistry Chemical Physics **11**, 8658 (2009).

[54] M. Oehzelt, N. Koch, and G. Heimel, "Organic semiconductor density of states controls the energy level alignment at electrode interfaces", Nature Communications **5**, 4174 (2014).

[55] S. Duhm, A. Gerlach, I. Salzmann, B. Bröker, R. Johnson, F. Schreiber, and N. Koch, "PTCDA on Au(111), Ag(111) and Cu(111): correlation of interface charge transfer to bonding distance", Organic Electronics **9**, 111–118 (2008).

[56] M. Willenbockel, D. Lüftner, B. Stadtmüller, G. Koller, C. Kumpf, S. Soubatch, P. Puschnig, M. G. Ramsey, and F. S. Tautz, "The interplay between interface structure, energy level alignment and chemical bonding strength at organic–metal interfaces", Physical Chemistry Chemical Physics **17**, 1530–1548 (2015).

[57] B. Stadtmüller, I. Kröger, F. Reinert, and C. Kumpf, "Submonolayer growth of CuPc on noble metal surfaces", Physical Review B **83**, 085416 (2011).

[58] A. Natan, L. Kronik, H. Haick, and R. Tung, "Electrostatic Properties of Ideal and Non-ideal Polar Organic Monolayers: Implications for Electronic Devices", Advanced Materials **19**, 4103–4117 (2007).

[59] F. Bussolotti, J. Yang, A. Hinderhofer, Y. Huang, W. Chen, S. Kera, A. T. S. Wee, and N. Ueno, "Origin of the energy level alignment at organic/organic interfaces: the role of structural defects", Physical Review B **89**, 115319 (2014).

[60] P. Phillips, "Screening and plasmons", in *Advanced solid state physics* (Cambridge University Press), pp. 115–145.

[61] M. Rösner, E. Şaşıoğlu, C. Friedrich, S. Blügel, and T. O. Wehling, "Wannier function approach to realistic coulomb interactions in layered materials and heterostructures", Physical Review B **92**, 085102 (2015).

[62] A. Emelyanenko and L. Boinovich, "On the effect of discrete charges adsorbed at the interface on nonionic liquid film stability: charges in the film", Journal of Physics: Condensed Matter **20**, 494227 (2008).

[63] J. D. Jackson, *Classical electrodynamics, 3rd edition* (Wiley, 1998).

[64] C. B. Harris, N.-H. Ge, R. L. Lingle, J. D. McNeill, and C. M. Wong, "Femtosecond dynamics of electrons on surfaces and at interfaces", Annual Review of Physical Chemistry **48**, 711–744 (1997).

[65] N. Koch, N. Ueno, and A. T. S. Wee, eds., *The molecule–metal interface* (Wiley, 2013).

[66] J. D. Baran, J. A. Larsson, R. A. J. Woolley, Y. Cong, P. J. Moriarty, A. A. Cafolla, K. Schulte, and V. R. Dhanak, "Theoretical and experimental comparison of SnPc, PbPc, and CoPc adsorption on Ag(111)", Physical Review B **81**, 075413 (2010).

[67] I. Kröger, B. Stadtmüller, C. Stadler, J. Ziroff, M. Kochler, A. Stahl, F. Pollinger, T.-L. Lee, J. Zegenhagen, F. Reinert, and C. Kumpf, "Submonolayer growth of copper-phthalocyanine on Ag(111)", New Journal of Physics **12**, 083038 (2010).

[68] G. Heimel, S. Duhm, I. Salzmann, A. Gerlach, A. Strozecka, J. Niederhausen, C. Bürker, T. Hosokai, I. Fernandez-Torrente, G. Schulze, S. Winkler, A. Wilke, R. Schlesinger, J. Frisch, B. Bröker, A. Vollmer, B. Detlefs, J. Pflaum, S. Kera, K. J. Franke, N. Ueno, J. I. Pascual, F. Schreiber, and N. Koch, "Charged and metallic molecular monolayers through surface-induced aromatic stabilization", Nature Chemistry **5**, 187–194 (2013).

[69] L. Romaner, G. Heimel, J.-L. Brédas, A. Gerlach, F. Schreiber, R. L. Johnson, J. Zegenhagen, S. Duhm, N. Koch, and E. Zojer, "Impact of bidirectional charge transfer and molecular distortions on the electronic structure of a metal-organic interface", Physical Review Letters **99**, 256801 (2007).

[70] I. Kröger, B. Stadtmüller, C. Kleimann, P. Rajput, and C. Kumpf, "Normal-incidence x-ray standing-wave study of copper phthalocyanine submonolayers on Cu(111) and Au(111)", Physical Review B **83**, 195414 (2011).

[71] A. Hauschild, R. Temirov, S. Soubatch, O. Bauer, A. Schöll, B. C. C. Cowie, T.-L. Lee, F. S. Tautz, and M. Sokolowski, "Normal-incidence x-ray standing-wave determination of the adsorption geometry of PTCDA on Ag(111): comparison of the ordered room-temperature and disordered low-temperature phases", Physical Review B **81**, 125432 (2010).

[72] B. Stadtmüller, D. Lüftner, M. Willenbockel, E. M. Reinisch, T. Sueyoshi, G. Koller, S. Soubatch, M. G. Ramsey, P. Puschnig, F. S. Tautz, and C. Kumpf, "Unexpected interplay of bonding height and energy level alignment at heteromolecular hybrid interfaces", Nature Communications **5**, 3685 (2014).

[73] B. Stadtmüller, S. Schröder, and C. Kumpf, "Heteromolecular metal–organic interfaces: electronic and structural fingerprints of chemical bonding", Journal of Electron Spectroscopy and Related Phenomena **204**, 80–91 (2015).

[74] P. Guaino, D. Carty, G. Hughes, O. McDonald, and A. A. Cafolla, "Long-range order in a multilayer organic film templated by a molecular-induced surface reconstruction: pentacene on Au(110)", Applied Physics Letters **85**, 2777–2779 (2004).

[75] C. Krull, R. Robles, A. Mugarza, and P. Gambardella, "Site- and orbital-dependent charge donation and spin manipulation in electron-doped metal phthalocyanines", Nature Materials **12**, 337–343 (2013).

[76] P. Scheuerer, L. L. Patera, F. Simbürger, F. Queck, I. Swart, B. Schuler, L. Gross, N. Moll, and J. Repp, "Charge-induced structural changes in a single molecule investigated by atomic force microscopy", Physical Review Letters **123**, 066001 (2019).

[77] M. Graus, M. Grimm, C. Metzger, M. Dauth, C. Tusche, J. Kirschner, S. Kümmel, A. Schöll, and F. Reinert, "Electron-vibration coupling in molecular materials: assignment of vibronic modes from photoelectron momentum mapping", Physical Review Letters **116**, 147601 (2016).

[78] D. R. T. Zahn, G. N. Gavrila, and G. Salvan, "Electronic and vibrational spectroscopies applied to organic/inorganic interfaces", Chemical Reviews **107**, 1161–1232 (2007).

[79] V. Gupta, "Interaction of radiation and matter and electronic spectra", in *Principles and applications of quantum chemistry* (Elsevier, 2016), pp. 291–337.

[80] X.-Y. Liu, X.-Y. Xie, W.-H. Fang, and G. Cui, "Theoretical insights into interfacial electron transfer between zinc phthalocyanine and molybdenum disulfide", The Journal of Physical Chemistry A **122**, 9587–9596 (2018).

[81] G. Witte and C. Wöll, "Growth of aromatic molecules on solid substrates for applications in organic electronics", Journal of Materials Research **19**, 1889–1916 (2004).

[82] J. Fraxedas, S. García-Gil, S. Monturet, N. Lorente, I. Fernández-Torrente, K. J. Franke, J. I. Pascual, A. Vollmer, R.-P. Blum, N. Koch, and P. Ordejón, "Modulation of surface charge transfer through competing long-range repulsive versus short-range attractive interactions", The Journal of Physical Chemistry C **115**, 18640–18648 (2011).

[83] G. Dutton and X.-Y. Zhu, "Unoccupied states in C_{60} thin films probed by two-photon photoemission", The Journal of Physical Chemistry B **106**, 5975–5981 (2002).

[84] A. Schöll, L. Kilian, Y. Zou, J. Ziroff, S. Hame, F. Reinert, E. Umbach, and R. H. Fink, "Disordering of an organic overlayer on a metal surface upon cooling", Science **329**, 303–305 (2010).

[85] S Kowarik, A Gerlach, and F Schreiber, "Organic molecular beam deposition: fundamentals, growth dynamics, and in situ studies", Journal of Physics: Condensed Matter **20**, 184005 (2008).

[86] S. R. Forrest, "Ultrathin organic films grown by organic molecular beam deposition and related techniques", Chemical Reviews **97**, 1793–1896 (1997).

[87] K. Ramasesha, S. R. Leone, and D. M. Neumark, "Real-time probing of electron dynamics using attosecond time-resolved spectroscopy", Annual Review of Physical Chemistry **67**, 41–63 (2016).

[88] S. M. Falke, C. A. Rozzi, D. Brida, M. Maiuri, M. Amato, E. Sommer, A. D. Sio, A. Rubio, G. Cerullo, E. Molinari, and C. Lienau, "Coherent ultrafast charge transfer in an organic photovoltaic blend", Science **344**, 1001–1005 (2014).

[89] M. Jacobs, J. Krumland, A. M. Valencia, H. Wang, M. Rossi, and C. Cocchi, "Ultrafast charge transfer and vibronic coupling in a laser-excited hybrid inorganic/organic interface", Advances in Physics: X **5**, 1749883 (2020).

[90] M. Pedio and B. Ressel, "Introduction to electronic properties and dynamics of organic complexes as self-assembled monolayers", in *Molecular self-assembly in nanoscience and nanotechnology* (InTech, 2017).

[91] U. Bovensiepen and P. Kirchmann, "Elementary relaxation processes investigated by femtosecond photoelectron spectroscopy of two-dimensional materials", Laser & Photonics Reviews **6**, 589–606 (2012).

[92] Y. Zhang, S. He, W. Guo, Y. Hu, J. Huang, J. R. Mulcahy, and W. D. Wei, "Surface-plasmon-driven hot electron photochemistry", Chemical Reviews **118**, 2927–2954 (2017).

[93] B. Ziaja, N. Medvedev, V. Tkachenko, T. Maltezopoulos, and W. Wurth, "Time-resolved observation of band-gap shrinking and electron-lattice thermalization within x-ray excited gallium arsenide", Scientific Reports **5**, 18068 (2015).

[94] Y. Zhang, J. Dai, X. Zhong, D. Zhang, G. Zhong, and J. Li, "Probing ultrafast dynamics of ferroelectrics by time-resolved pump-probe spectroscopy", Advanced Science **8**, 2102488 (2021).

[95] S. Mathias, C. La-O-Vorakiat, P. Grychtol, P. Granitzka, E. Turgut, J. M. Shaw, R. Adam, H. T. Nembach, M. E. Siemens, S. Eich, C. M. Schneider, T. J. Silva, M. Aeschlimann, M. M. Murnane, and H. C. Kapteyn, "Probing the timescale of the exchange interaction in a ferromagnetic alloy", Proceedings of the National Academy of Sciences **109**, 4792–4797 (2012).

[96] D. Brinks, R. Hildner, E. M. H. P. van Dijk, F. D. Stefani, J. B. Nieder, J. Hernando, and N. F. van Hulst, "Ultrafast dynamics of single molecules", Chem. Soc. Rev. **43**, 2476–2491 (2014).

[97] V. Tkachenko, V. Lipp, M. Büscher, F. Capotondi, H. Höppner, N. Medvedev, E. Pedersoli, M. J. Prandolini, G. M. Rossi, F. Tavella, S. Toleikis, M. Windeler, B. Ziaja, and U. Teubner, "Effect of auger recombination on transient optical properties in XUV and soft x-ray irradiated silicon nitride", Scientific Reports **11**, 5203 (2021).

[98] M. B. Smith and J. Michl, "Singlet fission", Chemical Reviews **110**, 6891–6936 (2010).

[99] E. A. A. Pogna, X. Jia, A. Principi, A. Block, L. Banszerus, J. Zhang, X. Liu, T. Sohier, S. Forti, K. Soundarapandian, B. Terrés, J. D. Mehew, C. Trovatello, C. Coletti, F. H. L. Koppens, M. Bonn, H. I. Wang, N. van Hulst, M. J. Verstraete, H. Peng, Z. Liu, C. Stampfer, G. Cerullo, and K.-J. Tielrooij, "Hot-carrier cooling in high-quality graphene is intrinsically limited by optical phonons", ACS Nano **15**, 11285–11295 (2021).

[100] H. Petek and S. Ogawa, "Femtosecond time-resolved two-photon photoemission studies of electron dynamics in metals", Progress in Surface Science **56**, 239–310 (1997).

[101] M. Bonn, A. Kleyn, and G. Kroes, "Real time chemical dynamics at surfaces", Surface Science **500**, 475–499 (2002).

[102] L. Hirst, "Principles of solar energy conversion", in *Comprehensive renewable energy* (Elsevier, 2012), pp. 293–313.

[103] K. Wandelt, ed., *Surface and interface science* (Wiley, 2013).

[104] S. Mathias, S. Eich, J. Urbancic, S. Michael, A. V. Carr, S. Emmerich, A. Stange, T. Popmintchev, T. Rohwer, M. Wiesenmayer, A. Ruffing, S. Jakobs, S. Hellmann, P. Matyba, C. Chen, L. Kipp, M. Bauer, H. C. Kapteyn, H. C. Schneider, K. Rossnagel, M. M. Murnane, and M. Aeschlimann, "Self-amplified photo-induced gap quenching in a correlated electron material", Nature Communications **7**, 12902 (2016).

[105] M. Aeschlimann, M. Bauer, and S. Pawlik, "Competing nonradiative channels for hot electron induced surface photochemistry", Chemical Physics **205**, 127–141 (1996).

[106] E. Knoesel, A. Hotzel, T. Hertel, M. Wolf, and G. Ertl, "Dynamics of photoexcited electrons in metals studied with time-resolved two-photon photoemission", Surface Science **368**, 76–81 (1996).

[107] L. Wang, Z. Wang, H.-Y. Wang, G. Grinblat, Y.-L. Huang, D. Wang, X.-H. Ye, X.-B. Li, Q. Bao, A.-S. Wee, S. A. Maier, Q.-D. Chen, M.-L. Zhong, C.-W. Qiu, and H.-B. Sun, "Slow cooling and efficient extraction of C-exciton hot carriers in MoS_2 monolayer", Nature Communications **8**, 13906 (2017).

[108] W. Qiu, W. Liang, J. Guo, L. Fang, N. Li, Q. Feng, and S. N. Luo, "Thickness-dependent ultrafast hot carrier and phonon dynamics of $PtSe_2$ films measured with femtosecond transient optical spectroscopy", Journal of Physics D: Applied Physics **54**, 075102 (2020).

[109] M. Wolf and G. Ertl, "Electron dynamics at surfaces", Science **288**, 1352–1353 (2000).

[110] P. Puschnig and C. Ambrosch-Draxl, "Excitons in organic semiconductors", Comptes Rendus Physique **10**, 504–513 (2009).

[111] C. J. Bardeen, "The structure and dynamics of molecular excitons", Annual Review of Physical Chemistry **65**, 127–148 (2014).

[112] I. Langmuir, "The adsorption of gases on plane surfaces of glass, mica and platinum", Journal of the American Chemical Society **40**, 1361–1403 (1918).

[113] Z. Liu, Y. Song, A. Rajappan, E. N. Wang, and D. J. Preston, "Temporal evolution of surface contamination under ultra-high vacuum", Langmuir **38**, 1252–1258 (2022).

[114] N. Comini, T. Huthwelker, J. T. Diulus, J. Osterwalder, and Z. Novotny, "Factors influencing surface carbon contamination in ambient-pressure x-ray photoelectron spectroscopy experiments", Journal of Vacuum Science &amp Technology A **39**, 043203 (2021).

[115] R. Ruiz, D. Choudhary, B. Nickel, T. Toccoli, K.-C. Chang, A. C. Mayer, P. Clancy, J. M. Blakely, R. L. Headrick, S. Iannotta, and G. G. Malliaras, "Pentacene thin film growth", Chemistry of Materials **16**, 4497–4508 (2004).

[116] S. R. Kachel, P.-M. Dombrowski, T. Breuer, J. M. Gottfried, and G. Witte, "Engineering of TMDC–OSC hybrid interfaces: the thermodynamics of unitary and mixed acene monolayers on MoS_2", Chemical Science **12**, 2575–2585 (2021).

[117] M. P. Seah and W. A. Dench, "Quantitative electron spectroscopy of surfaces: a standard data base for electron inelastic mean free paths in solids", Surface and Interface Analysis **1**, 2–11 (1979).

[118] C. J. Powell and A. Jablonski, "Evaluation of calculated and measured electron inelastic mean free paths near solid surfaces", Journal of Physical and Chemical Reference Data **28**, 19–62 (1999).

[119] T. Graber, F. Forster, A. Schöll, and F. Reinert, "Experimental determination of the attenuation length of electrons in organic molecular solids: the example of PTCDA", Surface Science **605**, 878–882 (2011).

[120] A. Damascelli, "Probing the electronic structure of complex systems by ARPES", Physica Scripta **T109**, 61 (2004).

[121] H. Hertz, "Ueber einen Einfluss des ultravioletten Lichtes auf die electrische Entladung", Annalen der Physik und Chemie **267**, 983–1000 (1887).

[122] A. Einstein, "Über einen die Erzeugung und Verwandlung des Lichtes betreffenden heuristischen Gesichtspunkt", Annalen der Physik **322**, 132–148 (1905).

[123] M. A. Brisk and A. Baker, "Shake-up satellites in x-ray photoelectron spectroscopy", Journal of Electron Spectroscopy and Related Phenomena **7**, 197–213 (1975).

[124] J. Moulder and J. Chastain, *Handbook of x-ray photoelectron spectroscopy: a reference book of standard spectra for identification and interpretation of xps data* (Physical Electronics Division, Perkin-Elmer Corporation, 1992).

[125] K. Siegbahn, "Electron spectroscopy for atoms, molecules, and condensed matter", Science **217**, 111–121 (1982).

[126] P. Puschnig, S. Berkebile, A. J. Fleming, G. Koller, K. Emtsev, T. Seyller, J. D. Riley, C. Ambrosch-Draxl, F. P. Netzer, and M. G. Ramsey, "Reconstruction of molecular orbital densities from photoemission data", Science **326**, 702–706 (2009).

[127] C. Metzger, M. Graus, M. Grimm, G. Zamborlini, V. Feyer, M. Schwendt, D. Lüftner, P. Puschnig, A. Schöll, and F. Reinert, "Plane-wave final state for photoemission from nonplanar molecules at a metal-organic interface", Physical Review B **101**, 165421 (2020).

[128] A. G. Shard, "Practical guides for x-ray photoelectron spectroscopy: quantitative XPS", Journal of Vacuum Science & Technology A **38**, 041201 (2020).

[129] J. Yeh and I. Lindau, "Atomic subshell photoionization cross sections and asymmetry parameters: $1 \leq Z \leq 103$", Atomic Data and Nuclear Data Tables **32**, 1–155 (1985).

[130] D. P. Woodruff and A. M. Bradshaw, "Adsorbate structure determination on surfaces using photoelectron diffraction", Reports on Progress in Physics **57**, 1029–1080 (1994).

[131] J. Osterwalder, P. Aebi, R. Fasel, D. Naumovic, P. Schwaller, T. Kreutz, L. Schlapbach, T. Abukawa, and S. Kono, "Angle-scanned photoelectron diffraction", Surface Science **331-333**, 1002–1014 (1995).

[132] C. Fadley, M. V. Hove, Z. Hussain, and A. Kaduwela, "Photoelectron diffraction: new dimensions in space, time, and spin", Journal of Electron Spectroscopy and Related Phenomena **75**, 273–297 (1995).

[133] M. Muntwiler, W. Auwärter, F. Baumberger, M. Hoesch, T. Greber, and J. Osterwalder, "Determining adsorbate structures from substrate emission x-ray photoelectron diffraction", Surface Science **472**, 125–132 (2001).

[134] D. Woodruff, "Photoelectron diffraction: past, present and future", Journal of Electron Spectroscopy and Related Phenomena **126**, 55–65 (2002).

[135] D. Woodruff, "Surface structural information from photoelectron diffraction", Journal of Electron Spectroscopy and Related Phenomena **178-179**, 186–194 (2010).

[136] J. Osterwalder, T. Greber, P. Aebi, R. Fasel, and L. Schlapbach, "Final-state scattering in angle-resolved ultraviolet photoemission from copper", Physical Review B **53**, 10209–10216 (1996).

[137] M. Greif, L. Castiglioni, A. P. Seitsonen, S. Roth, J. Osterwalder, and M. Hengsberger, "Photoelectron diffraction in the x-ray and ultraviolet regime: Sn-phthalocyanine on Ag(111)", Physical Review B **87**, 085429 (2013).

[138] M. Greif, L. Kasmi, L. Castiglioni, M. Lucchini, L. Gallmann, U. Keller, J. Osterwalder, and M. Hengsberger, "Access to phases of coherent phonon excitations by femtosecond ultraviolet photoelectron diffraction", Physical Review B **94**, 054309 (2016).

[139] P. Krüger, "Photoelectron diffraction from valence states of oriented molecules", Journal of the Physical Society of Japan **87**, 061007 (2018).

[140] W. D. Grobman, "Angle-resolved photoemission from molecules in the independent-atomic-center approximation", Physical Review B **17**, 4573–4585 (1978).

[141] R. Fasel, J. Wider, C. Quitmann, K.-H. Ernst, and T. Greber, "Determination of the absolute chirality of adsorbed molecules", Angewandte Chemie International Edition **43**, 2853–2856 (2004).

[142] G. Schönhense and H.-J. Elmers, "Spin- and time-resolved photoelectron spectroscopy and diffraction studies using time-of-flight momentum microscopes", Journal of Vacuum Science & Technology A **40**, 020802 (2022).

[143] G. Saathoff, L. Miaja-Avila, M. Aeschlimann, M. M. Murnane, and H. C. Kapteyn, "Laser-assisted photoemission from surfaces", Physical Review A **77**, 022903 (2008).

[144] B. Schönhense, K. Medjanik, O. Fedchenko, S. Chernov, M. Ellguth, D. Vasilyev, A. Oelsner, J. Viefhaus, D. Kutnyakhov, W. Wurth, H.-J. Elmers, and G. Schönhense, "Multidimensional photoemission spectroscopy—the space-charge limit", New Journal of Physics **20**, 033004 (2018).

[145] A. McPherson, G. Gibson, H. Jara, U. Johann, T. S. Luk, I. A. McIntyre, K. Boyer, and C. K. Rhodes, "Studies of multiphoton production of vacuum-ultraviolet radiation in the rare gases", J. Opt. Soc. Am. B **4**, 595–601 (1987).

[146] J. Zhou, J. Peatross, M. M. Murnane, H. C. Kapteyn, and I. P. Christov, "Enhanced high-harmonic generation using 25 fs laser pulses", Physical Review Letters **76**, 752–755 (1996).

[147] Z. Chang, A. Rundquist, H. Wang, M. M. Murnane, and H. C. Kapteyn, "Generation of coherent soft x-rays at 2.7 nm using high harmonics", Physical Review Letters **79**, 2967–2970 (1997).

[148] F. Krausz and M. Ivanov, "Attosecond physics", Reviews of Modern Physics **81**, 163–234 (2009).

[149] M. Martins, M. Wellhöfer, J. T. Hoeft, W. Wurth, J. Feldhaus, and R. Follath, "Monochromator beamline for FLASH", Review of Scientific Instruments **77**, 115108 (2006).

[150] N. Huang, H. Deng, B. Liu, D. Wang, and Z. Zhao, "Features and futures of x-ray free-electron lasers", The Innovation **2**, 100097 (2021).

[151] Y. L. Wang, W. Ji, D. X. Shi, S. X. Du, C. Seidel, Y. G. Ma, H.-J. Gao, L. F. Chi, and H. Fuchs, "Structural evolution of pentacene on a Ag(110) surface", Physical Review B **69**, 075408 (2004).

[152] S. Söhnchen, S. Lukas, and G. Witte, "Epitaxial growth of pentacene films on Cu(110)", The Journal of Chemical Physics **121**, 525 (2004).

[153] M. Grimm, C. Metzger, M. Graus, M. Jugovac, G. Zamborlini, V. Feyer, A. Schöll, and F. Reinert, "Molecular orbital imaging beyond the first monolayer: insights into the pentacene/Ag(110) interface", Physical Review B **98**, 195412 (2018).

[154] F. Bussolotti, S. Kera, and N. Ueno, "Potassium doping of single crystalline pentacene thin film", Physical Review B **86**, 155120 (2012).

[155] T. Schwieger, X. Liu, D. Olligs, M. Knupfer, and T. Schmidt, "Orientation and electronic properties of pentacene molecules on SiO_2 and GeS(0001) studied using x-ray absorption spectroscopy", Journal of Applied Physics **96**, 5596–5600 (2004).

[156] D. B. Dougherty, W. Jin, W. G. Cullen, J. E. Reutt-Robey, and S. W. Robey, "Variable temperature scanning tunneling microscopy of pentacene monolayer and bilayer phases on Ag(111)", The Journal of Physical Chemistry C **112**, 20334–20339 (2008).

[157] S. Koslowski, D. Rosenblatt, A. Kabakchiev, K. Kuhnke, K. Kern, and U. Schlickum, "Adsorption and electronic properties of pentacene on thin dielectric decoupling layers", Beilstein Journal of Nanotechnology **8**, 1388–1395 (2017).

[158] S. H. Park and S. Kwon, "Dynamics of molecular orientation observed using angle resolved photoemission spectroscopy during deposition of pentacene on graphite", Analytical Chemistry **88**, 4565–4570 (2016).

[159] D. N. Congreve, J. Lee, N. J. Thompson, E. Hontz, S. R. Yost, P. D. Reusswig, M. E. Bahlke, S. Reineke, T. V. Voorhis, and M. A. Baldo, "External quantum efficiency above 100% in a singlet-exciton-fission–based organic photovoltaic cell", Science **340**, 334–337 (2013).

[160] D. M. N. M. Dissanayake, A. A. D. T. Adikaari, R. J. Curry, R. A. Hatton, and S. R. P. Silva, "Nanoimprinted large area heterojunction pentacene-C_{60} photovoltaic device", Applied Physics Letters **90**, 253502 (2007).

[161] Y. Yamashita, "Organic semiconductors for organic field-effect transistors", Science and Technology of Advanced Materials **10**, 024313 (2009).

[162] T. Hasegawa and J. Takeya, "Organic field-effect transistors using single crystals", Science and Technology of Advanced Materials **10**, 024314 (2009).

[163] E. Salvadori, J. D. Breeze, K.-J. Tan, J. Sathian, B. Richards, M. W. Fung, G. Wolfowicz, M. Oxborrow, N. M. Alford, and C. W. M. Kay, "Nanosecond time-resolved characterization of a pentacene-based room-temperature MASER", Scientific Reports **7**, 41836 (2017).

[164] Q. Yang, M. Muntwiler, and X.-Y. Zhu, "Charge transfer excitons and image potential states on organic semiconductor surfaces", Physical Review B **80**, 115214 (2009).

[165] Q. Wang, J. Yang, A. Franco-Cañellas, C. Bürker, J. Niederhausen, P. Dombrowski, F. Widdascheck, T. Breuer, G. Witte, A. Gerlach, S. Duhm, and F. Schreiber, "Pentacene/perfluoropentacene bilayers on Au(111) and Cu(111): impact of organic–metal coupling strength on molecular structure formation", Nanoscale Advances **3**, 2598–2606 (2021).

[166] G. Mercurio, O. Bauer, M. Willenbockel, N. Fairley, W. Reckien, C. H. Schmitz, B. Fiedler, S. Soubatch, T. Bredow, M. Sokolowski, and F. S. Tautz, "Adsorption height determination of nonequivalent C and O species of PTCDA on Ag(110) using x-ray standing waves", Physical Review B **87**, 045421 (2013).

[167] S. Duhm, C. Bürker, J. Niederhausen, I. Salzmann, T. Hosokai, J. Duvernay, S. Kera, F. Schreiber, N. Koch, N. Ueno, and A. Gerlach, "Pentacene on Ag(111): correlation of bonding distance with intermolecular interaction and order", ACS Applied Materials & Interfaces **5**, 9377–9381 (2013).

[168] F. Amy, C. K. Chan, W. Zhao, J. Hyung, M. Ono, T. Sueyoshi, S. Kera, G. Nesher, A. Salomon, L. Segev, O. Seitz, H. Shpaisman, A. Schöll, M. Haeming, T. Böcking, D. Cahen, L. Kronik, N. Ueno, E. Umbach, and A. Kahn, "Radiation damage to alkyl chain monolayers on semiconductor substrates investigated by electron spectroscopy", The Journal of Physical Chemistry B **110**, 21826–21832 (2006).

[169] A. Tebyani, F. B. Baalbergen, R. M. Tromp, and S. J. van der Molen, "Low-energy electron irradiation damage in few-monolayer pentacene films", The Journal of Physical Chemistry C **125**, 26150–26156 (2021).

[170] M. D. Angela, T. Anniyev, M. Beye, R. Coffee, A. Föhlisch, J. Gladh, S. Kaya, T. Katayama, O. Krupin, A. Nilsson, D. Nordlund, W. F. Schlotter, J. A. Sellberg, F. Sorgenfrei, J. J. Turner, H. Öström, H. Ogasawara, M. Wolf, and W. Wurth, "Vacuum space charge effects in sub-picosecond soft x-ray photoemission on a molecular adsorbate layer", Structural Dynamics **2**, 025101 (2015).

[171] M. Ono, H. Yamane, H. Fukagawa, S. Kera, D. Yoshimura, E. Morikawa, K. Seki, and N. Ueno, "Possibility of the Fermi level control by VUV-induced doping of an organic thin film: polytetrafluoroethylene", IPAP Conf. Series **6**, 27 (2008).

[172] E. Morikawa, J. Choi, H. M. Manohara, H. Ishii, K. Seki, K. K. Okudaira, and N. Ueno, "Photoemission study of direct photomicromachining in poly(vinylidene fluoride)", Journal of Applied Physics **87**, 4010–4016 (2000).

[173] W.-H. Soe, C. Manzano, A. D. Sarkar, N. Chandrasekhar, and C. Joachim, "Direct observation of molecular orbitals of pentacene physisorbed on Au(111) by scanning tunneling microscope", Physical Review Letters **102**, 176102 (2009).

[174] M. Bernardi, J. Mustafa, J. B. Neaton, and S. G. Louie, "Theory and computation of hot carriers generated by surface plasmon polaritons in noble metals", Nature Communications **6**, 7044 (2015).

[175] B. Xiang, Y. Li, C. H. Pham, F. Paesani, and W. Xiong, "Ultrafast direct electron transfer at organic semiconductor and metal interfaces", Science Advances **3**, 2375–2548 (2017).

[176] T. M. Halasinski, D. M. Hudgins, F. Salama, L. J. Allamandola, and T. Bally, "Electronic absorption spectra of neutral pentacene ($C_{22}H_{14}$) and its positive and negative ions in Ne, Ar, and Kr matrices", The Journal of Physical Chemistry A **104**, 7484–7491 (2000).

[177] J. Zirzlmeier, D. Lehnherr, P. B. Coto, E. T. Chernick, R. Casillas, B. S. Basel, M. Thoss, R. R. Tykwinski, and D. M. Guldi, "Singlet fission in pentacene dimers", Proceedings of the National Academy of Sciences **112**, 5325–5330 (2015).

[178] R. Costantini, R. Faber, A. Cossaro, L. Floreano, A. Verdini, C. Hättig, A. Morgante, S. Coriani, and M. Dell'Angela, "Picosecond timescale tracking of pentacene triplet excitons with chemical sensitivity", Communications Physics **2**, 56 (2019).

[179] J. R. Dwyer, R. E. Jordan, B. J. Siwick, C. T. Hebeisen, and R. D. Miller, "Femtosecond electron diffraction: towards making the "molecular movie"", in *Springer series in chemical physics* (Springer Berlin Heidelberg, 2005), pp. 144–148.

[180] J. Wilson and A. Yoffe, "The transition metal dichalcogenides discussion and interpretation of the observed optical, electrical and structural properties", Advances in Physics **18**, 193–335 (1969).

[181] K. Rossnagel, "On the origin of charge-density waves in select layered transition-metal dichalcogenides", Journal of Physics: Condensed Matter **23**, 213001 (2011).

[182] S. Manzeli, D. Ovchinnikov, D. Pasquier, O. V. Yazyev, and A. Kis, "2D transition metal dichalcogenides", Nature Reviews Materials **2**, 17033 (2017).

[183] S. Hellmann, T. Rohwer, M. Kalläne, K. Hanff, C. Sohrt, A. Stange, A. Carr, M. Murnane, H. Kapteyn, L. Kipp, M. Bauer, and K. Rossnagel, "Time-domain classification of charge-density-wave insulators", Nature Communications **3**, 1069 (2012).

[184] Z. Hu, Z. Wu, C. Han, J. He, Z. Ni, and W. Chen, "Two-dimensional transition metal dichalcogenides: interface and defect engineering", Chemical Society Reviews **47**, 3100–3128 (2018).

[185] S. J. McDonnell and R. M. Wallace, "Atomically-thin layered films for device applications based upon 2D TMDC materials", Thin Solid Films **616**, 482–501 (2016).

[186] M. D. Watson, O. J. Clark, F. Mazzola, I. Marković, V. Sunko, T. K. Kim, K. Rossnagel, and P. D. King, "Orbital- and k_z-selective hybridization of Se 4*p* and Ti 3*d* states in the charge density wave phase of $TiSe_2$", Physical Review Letters **122**, 076404 (2019).

[187] B. Stadtmüller, I. Kröger, F. Reinert, and C. Kumpf, "Submonolayer growth of CuPc on noble metal surfaces", Physical Review B **83**, 085416 (2011).

[188] C. Stadler, S. Hansen, F. Pollinger, C. Kumpf, E. Umbach, T.-L. Lee, and J. Zegenhagen, "Structural investigation of the adsorption of SnPc on Ag(111) using normal-incidence x-ray standing waves", Physical Review B **74**, 035404 (2006).

[189] L. A. Rochford, A. J. Ramadan, D. P. Woodruff, S. Heutz, and T. S. Jones, "Ordered growth of vanadyl phthalocyanine (VOPc) on an iron phthalocyanine (FePc) monolayer", Physical Chemistry Chemical Physics **17**, 29747–29752 (2015).

[190] K. Schönauer, S. Weiss, V. Feyer, D. Lüftner, B. Stadtmüller, D. Schwarz, T. Sueyoshi, C. Kumpf, P. Puschnig, M. G. Ramsey, F. S. Tautz, and S. Soubatch, "Charge transfer and symmetry reduction at the CuPc/Ag(110) interface studied by photoemission tomography", Physical Review B **94**, 205144 (2016).

[191] K. Greulich, A. Belser, T. Basova, T. Chassé, and H. Peisert, "Interfaces between different iron phthalocyanines and Au(111): influence of the fluorination on structure and interfacial interactions", The Journal of Physical Chemistry C **126**, 716–727 (2021).

[192] V. Feyer, M. Graus, P. Nigge, M. Wießner, R. Acres, C. Wiemann, C. Schneider, A. Schöll, and F. Reinert, "Adsorption geometry and electronic structure of iron phthalocyanine on Ag surfaces: a LEED and photoelectron momentum mapping study", Surface Science **621**, 64–68 (2014).

[193] F. Haidu, G. Salvan, D. R. T. Zahn, L. Smykalla, M. Hietschold, and M. Knupfer, "Transport band gap opening at metal–organic interfaces", Journal of Vacuum Science & Technology A: Vacuum, Surfaces, and Films **32**, 040602 (2014).

[194] B. Stadtmüller, S. Emmerich, D. Jungkenn, N. Haag, M. Rollinger, S. Eich, M. Maniraj, M. Aeschlimann, M. Cinchetti, and S. Mathias, "Strong modification of the transport level alignment in organic materials after optical excitation", Nature Communications **10**, 1470 (2019).

[195] T. Schwieger, H. Peisert, M. S. Golden, M. Knupfer, and J. Fink, "Electronic structure of the organic semiconductor copper phthalocyanine and K-CuPc studied using photoemission spectroscopy", Physical Review B **66**, 155207 (2002).

[196] D. G. de Oteyza, J. M. GarcÃa-Lastra, M. Corso, B. P. Doyle, L. Floreano, A. Morgante, Y. Wakayama, A. Rubio, and J. E. Ortega, "Customized electronic coupling in self-assembled donor-acceptor nanostructures", Advanced Functional Materials **19**, 3567–3573 (2009).

[197] F. Evangelista, V. Carravetta, G. Stefani, B. Jansik, M. Alagia, S. Stranges, and A. Ruocco, "Electronic structure of copper phthalocyanine: an experimental and theoretical study of occupied and unoccupied levels", The Journal of Chemical Physics **126**, 124709 (2007).

[198] F. Evangelista, A. Ruocco, R. Gotter, A. Cossaro, L. Floreano, A. Morgante, F. Crispoldi, M. G. Betti, and C. Mariani, "Electronic states of CuPc chains on the Au(110) surface", The Journal of Chemical Physics **131**, 174710 (2009).

[199] M. V. Nardi, F. Detto, L. Aversa, R. Verucchi, G. Salviati, S. Iannotta, and M. Casarin, "Electronic properties of CuPc and H_2Pc: an experimental and theoretical study", Physical Chemistry Chemical Physics **15**, 12864 (2013).

[200] M. L. Vidal, A. I. Krylov, and S. Coriani, "Dyson orbitals within the fc-CVS-EOM-CCSD framework: theory and application to x-ray photoelectron spectroscopy of ground and excited states", Physical Chemistry Chemical Physics **22**, 2693–2703 (2020).

[201] H. Hedayat, C. J. Sayers, D. Bugini, C. Dallera, D. Wolverson, T. Batten, S. Karbassi, S. Friedemann, G. Cerullo, J. van Wezel, S. R. Clark, E. Carpene, and E. D. Como, "Excitonic and lattice contributions to the charge density wave in 1T-$TiSe_2$ revealed by a phonon bottleneck", Physical Review Research **1**, 023029 (2019).

[202] S. Duan, Y. Cheng, W. Xia, Y. Yang, C. Xu, F. Qi, C. Huang, T. Tang, Y. Guo, W. Luo, D. Qian, D. Xiang, J. Zhang, and W. Zhang, "Optical manipulation of electronic dimensionality in a quantum material", Nature **595**, 239–244 (2021).

[203] Y. Cheng, A. Zong, J. Li, W. Xia, S. Duan, W. Zhao, Y. Li, F. Qi, J. Wu, L. Zhao, P. Zhu, X. Zou, T. Jiang, Y. Guo, L. Yang, D. Qian, W. Zhang, A. Kogar, M. W. Zuerch, D. Xiang, and J. Zhang, "Light-induced dimension crossover dictated by excitonic correlations", Nature Communications **13**, 963 (2022).

[204] C. Monney, M. Puppin, C. W. Nicholson, M. Hoesch, R. T. Chapman, E. Springate, H. Berger, A. Magrez, C. Cacho, R. Ernstorfer, and M. Wolf, "Revealing the role of electrons and phonons in the ultrafast recovery of charge density wave correlations in 1T-$TiSe_2$", Physical Review B **94**, 165165 (2016).

[205] G. Rohde, T. Rohwer, C. Sohrt, A. Stange, S. Hellmann, L. X. Yang, K. Hanff, A. Carr, M. M. Murnane, H. Kapteyn, L. Kipp, K. Rossnagel, and M. Bauer, "Tracking the relaxation pathway of photo-excited electrons in 1T-$TiSe_2$", The European Physical Journal Special Topics **222**, 997–1004 (2013).

[206] O. Gordan, M. Friedrich, and D. Zahn, "The anisotropic dielectric function for copper phthalocyanine thin films", Organic Electronics **5**, 291–297 (2004).

[207] M. Porer, U. Leierseder, J.-M. Ménard, H. Dachraoui, L. Mouchliadis, I. E. Perakis, U. Heinzmann, J. Demsar, K. Rossnagel, and R. Huber, "Non-thermal separation of electronic and structural orders in a persisting charge density wave", Nature Materials **13**, 857–861 (2014).

[208] M. Haniuda, M. Nozaki, and K. Niki, "A faster method of photoelectron intensity calculation based on multiple scattering theory", e-Journal of Surface Science and Nanotechnology **advpub**, 2022–037 (2022).

[209] K. E. Drexler, "Molecular engineering: an approach to the development of general capabilities for molecular manipulation", Proceedings of the National Academy of Sciences **78**, 5275–5278 (1981).

[210] B. L. Feringa, "In control of motion: from molecular switches to molecular motors", Accounts of Chemical Research **34**, 504–513 (2001).

[211] M. Peplow, "The tiniest lego: a tale of nanoscale motors, rotors, switches and pumps", Nature **525**, 18–21 (2015).

[212] R. Zhao, F. Qi, Y.-L. Zhao, K. E. Hermann, R.-Q. Zhang, and M. A. V. Hove, "Interlocking molecular gear chains built on surfaces", The Journal of Physical Chemistry Letters **9**, 2611–2619 (2018).

[213] Z. H. Cheng, L. Gao, Z. T. Deng, N. Jiang, Q. Liu, D. X. Shi, S. X. Du, H. M. Guo, and H.-J. Gao, "Adsorption behavior of iron phthalocyanine on Au(111) surface at submonolayer coverage", The Journal of Physical Chemistry C **111**, 9240–9244 (2007).

[214] R. Cuadrado, J. I. Cerdá, Y. Wang, G. Xin, R. Berndt, and H. Tang, "CoPc adsorption on Cu(111): origin of the C4 to C2 symmetry reduction", The Journal of Chemical Physics **133**, 154701 (2010).

[215] S. Fremy-Koch, A. Sadeghi, R. Pawlak, S. Kawai, A. Baratoff, S. Goedecker, E. Meyer, and T. Glatzel, "Controlled switching of a single CuPc molecule on Cu(111) at low temperature", Physical Review B **100**, 155427 (2019).

[216] I. Kröger, B. Stadtmüller, C. Wagner, C. Weiss, R. Temirov, F. S. Tautz, and C. Kumpf, "Modeling intermolecular interactions of physisorbed organic molecules using pair potential calculations", The Journal of Chemical Physics **135**, 234703 (2011).

[217] D. Civita, M. Kolmer, G. J. Simpson, A.-P. Li, S. Hecht, and L. Grill, "Control of long-distance motion of single molecules on a surface", Science **370**, 957–960 (2020).

[218] O. Snezhkova, J. Lüder, A. Wiengarten, S. R. Burema, F. Bischoff, Y. He, J. Rusz, J. Knudsen, M.-L. Bocquet, K. Seufert, J. V. Barth, W. Auwärter, B. Brena, and J. Schnadt, "Nature of the bias-dependent symmetry reduction of iron phthalocyanine on Cu(111)", Physical Review B **92**, 075428 (2015).

[219] Y. Zhang, J. P. Calupitan, T. Rojas, R. Tumbleson, G. Erbland, C. Kammerer, T. M. Ajayi, S. Wang, L. A. Curtiss, A. T. Ngo, S. E. Ulloa, G. Rapenne, and S. W. Hla, "A chiral molecular propeller designed for unidirectional rotations on a surface", Nature Communications **10**, 3742 (2019).

[220] A. Mugarza, N. Lorente, P. Ordejón, C. Krull, S. Stepanow, M.-L. Bocquet, J. Fraxedas, G. Ceballos, and P. Gambardella, "Orbital specific chirality and homochiral self-assembly of achiral molecules induced by charge transfer and spontaneous symmetry breaking", Physical Review Letters **105**, 115702 (2010).

[221] M. Parschau, S. Romer, and K.-H. Ernst, "Induction of homochirality in achiral enantiomorphous monolayers", Journal of the American Chemical Society **126**, 15398–15399 (2004).

[222] C. Bombis, S. Weigelt, M. M. Knudsen, M. Nørgaard, C. Busse, E. Lægsgaard, F. Besenbacher, K. V. Gothelf, and T. R. Linderoth, "Steering organizational and conformational surface chirality by controlling molecular chemical functionality", ACS Nano **4**, 297–311 (2009).

[223] T. Chen, D. Wang, and L.-J. Wan, "Two-dimensional chiral molecular assembly on solid surfaces: formation and regulation", National Science Review **2**, 205–216 (2015).

[224] C.-K. Ma, Y. Wang, M.-X. Shi, Y.-R. Wang, K. Sun, M.-L. Tao, D.-X. Yang, Z.-L. Wang, Z.-J. Wu, and J.-Z. Wang, "Coexistence of chiral and achiral adsorptions of metal-free phthalocyanine molecules on Cd(0001)", The Journal of Physical Chemistry C **125**, 335–340 (2021).

[225] G. Molnár, S. Rat, L. Salmon, W. Nicolazzi, and A. Bousseksou, "Spin crossover nanomaterials: from fundamental concepts to devices", Advanced Materials **30**, 1703862 (2017).

[226] K.-H. Ernst, "Amplification of chirality in two-dimensional molecular lattices", Current Opinion in Colloid & Interface Science **13**, 54–59 (2008).

[227] Q. Sallembien, L. Bouteiller, J. Crassous, and M. Raynal, "Possible chemical and physical scenarios towards biological homochirality", Chemical Society Reviews **51**, 3436–3476 (2022).

[228] M. M. Green, N. C. Peterson, T. Sato, A. Teramoto, R. Cook, and S. Lifson, "A helical polymer with a cooperative response to chiral information", Science **268**, 1860–1866 (1995).

[229] Y. Fang, E. Ghijsens, O. Ivasenko, H. Cao, A. Noguchi, K. S. Mali, K. Tahara, Y. Tobe, and S. D. Feyter, "Dynamic control over supramolecular handedness by selecting chiral induction pathways at the solution–solid interface", Nature Chemistry **8**, 711–717 (2016).

[230] R. Fasel, M. Parschau, and K.-H. Ernst, "Amplification of chirality in two-dimensional enantiomorphous lattices", Nature **439**, 449–452 (2006).

[231] S. Haq, N. Liu, V. Humblot, A. P. J. Jansen, and R. Raval, "Drastic symmetry breaking in supramolecular organization of enantiomerically unbalanced monolayers at surfaces", Nature Chemistry **1**, 409–414 (2009).

[232] C. J. Baddeley, "Giving surfaces a hand", Nature Chemistry **1**, 345–346 (2009).

[233] H. Cao and S. D. Feyter, "Amplification of chirality in surface-confined supramolecular bilayers", Nature Communications **9**, 3416 (2018).

[234] M. M. J. Smulders, P. J. M. Stals, T. Mes, T. F. E. Paffen, A. P. H. J. Schenning, A. R. A. Palmans, and E. W. Meijer, "Probing the limits of the majority-rules principle in a dynamic supramolecular polymer", Journal of the American Chemical Society **132**, 620–626 (2009).

[235] A. H. Zewail, "Femtochemistry: Atomic-Scale Dynamics of the Chemical Bond", The Journal of Physical Chemistry A **104**, 5660–5694 (2000).